Right-Handed currents and Electroweak penguins in B decays.

By

Abinash Kumar Nayak

PHYS10201205009

The Institute of Mathematical Sciences, Chennai

A thesis submitted to the

Board of Studies in Physical Sciences

In partial fulfillment of requirements

For the Degree of

DOCTOR OF PHILOSOPHY

of

HOMI BHABHA NATIONAL INSTITUTE

July, 2020

Homi Bhabha National Institute

Recommendations of the Viva Voice Board

As members of the Viva Voice Board, we certify that we have read the dissertation prepared by Abinash Kumar Nayak entitled “Right-Handed currents and Electroweak penguins in B decays” and recommend that it may be accepted as fulfilling the dissertation requirements for the Degree of Doctor of Philosophy.

Date: 19.1.2021
Chair - D. INDUMATHI

Date: 19.1.2021
Guide/Convener - RAHUL SINHA

Date: 19.1.2021
Member 1 - V. RAVINDRAN

Date: 19.1.2021
Member 2 - SHRIHARI GOPALAKRISHNA

Satyavani Vemparala
replaced by the Dean of Physical Sciences, IMSc Date: 19.1.2021
Member 3 - PARTHA MUKHOPADHYAYA

Date: 19.1.2021
External Examiner NAMIT MAHAJAN

Final approval and acceptance of this dissertation is contingent upon the candidate’s submission of the final copies of the dissertation to HBNI.

I hereby certify that I have read this dissertation prepared under my direction and recommend that it may be accepted as fulfilling the dissertation requirement.

Date: 19.1.2021

Place: Chennai

Guide

STATEMENT BY AUTHOR

This dissertation has been submitted in partial fulfillment of requirements for an advanced degree at Homi Bhabha National Institute (HBNI) and is deposited in the Library to be made available to borrowers under the rules of HBNI.

Brief quotations from this dissertation are allowable without special permission provided that accurate acknowledgment of the source is made. Requests for permission for extended quotation from or reproduction of this manuscript in whole or in part may be granted by the Competent Authority of HBNI when in his or her judgment the proposed use of the material is in the interests of scholarship. In all other instances, however, permission must be obtained from the author.

Abinash Kr. Nayak.
19/01/2021
Abinash Kumar Nayak

DECLARATION

I, hereby declare that the investigation presented in this thesis has been carried out by me. The work is original and has not been submitted earlier as a whole or in part for a degree/diploma at this or any other Institution/University.

Abinash Kr. Nayak.
19/01/2021
Abinash Kumar Nayak

List of Publications arising from this Thesis

- **Published**

  1. **Signal of right-handed currents using $B \to K^* \ell^+ \ell^-$ observables at the kinematic endpoint**,

     Anirban Karan, Rusa Mandal, Abinash Kumar Nayak, Rahul Sinha, and Thomas E. Browder,

     Physical Review D 95, 114006 (2017).

  2. **Constraining electroweak penguin graph contributions in measurements of the CKM phase alpha using $B \to \pi\pi$ and $B \to \rho\rho$ decays**,

     Abinash Kumar Nayak, Rahul Sinha, Anirban Karan, and Benjamin Grinstein,

     Physical Review D 101, 073001 (2020).

List of other Publications, Not included in this thesis

- **Published**

  1. **Using time-dependent indirect CP asymmetries to measure T and CPT violation in $B^0 - \bar{B}^0$ mixing**,

     Anirban Karan, Abinash Kumar Nayak, Rahul Sinha, and David London,

     Physics Letters B 781, 459-463 (2018).

  2. **Behavior of observables for neutral meson decaying to two vectors in the presence of T, CP, and CPT violation in mixing only** ,

     Anirban Karan, and Abinash Kumar Nayak,

     Physics Review D 101, 015027 (2020).

Abinash kr. Nayak.
19/01/2021
Abinash Kumar Nayak

Talks Presented at Schools/Conferences/Workshops

1. Talk on ***"Signal of right-handed current in*** $B \to K^* \ell^+ \ell^-$***"***,

   at 7th Belle Analysis Workshop, 30th November 2017, MNIT, Jaipur, India.

2. Talk on ***"Exploring*** T ***and*** CPT ***violation in time-dependent*** CP ***asymmetry of*** $B^0 - \bar{B}^0$ ***systems"***,

   at IFIC, 14th September 2018, Valencia, Spain.

3. Talk on ***"Exploring*** CPT ***violation in*** $B^0 - \bar{B}^0$ ***oscillation"***,

   at Particle Physics Challenges, 26th September 2018,

   DESY Hamburg, Germany.

4. Talk on ***"Exploring*** CPT ***violation in*** $B^0 - \bar{B}^0$ ***oscillation"***,

   at Nikhef, 2nd October 2018, Amsterdam, Netherlands.

5. Talk on ***"What can we learn from Charmless*** B ***decays"***,

   at WHEPP XVI, 4th December 2019, IIT Guwahati, India.

Abinash kr. Nayak.
19/01/2021
Abinash Kumar Nayak

Dedicated

to

my Teachers.

ACKNOWLEDGEMENTS

First of all, I would like to express my sincerest gratitude to my supervisor Prof. Rahul Sinha. I would like to thank him for his incredible guidance, patience, encouragement, and belief in me throughout this elevating journey. His immense knowledge of physics in general is truly amazing. I am grateful to him for always motivating and encouraging me to work hard and discover my real potential. His altruistic concern for the students is certainly noteworthy. I thank him for allowing me to work under him, it has been a real pleasure.

I would like to extend my gratitude to senior collaborators Prof. Benjamin Grinstein, Prof. David London, and Prof. Thomas E. Browder for some wonderful collaborations. I am grateful to my collaborators Dr. Rusa Mandal and Dr. Anirban Karan for sharing their knowledge and experience with me. I would like to thank them for being there always for me and making this journey easier. I have been extremely lucky to have them as collaborators.

I would like to thank all my teachers in IMSc for introducing me to the amazing world of physics. I thank my doctoral committee members Prof. D. Indumathi, Prof. V. Ravindran, Prof. Shrihari Gopalakrishna, and Prof. Partha Mukhopadhyaya for their continuous support and encouragement. A special thanks to Prof. D. Indumathi who has been an excellent teacher as well as an admirable mentor. I would like to thank the members of IMSc Pheno Group where I have learned many exciting aspects of particle phenomenology. I would also like to thank Prof. Antonio Pich, Prof. Christophe Grojean, and Prof. Robert Fleischer for visits to their respective institutes and granting me the opportunity to present my work.

I thank the dean academic Prof. Sibasish Ghosh for being very helpful with any HBNI related issues. It is my pleasure to thank the entire IMSc administration. They do their jobs in the best way possible and make life at IMSc really enjoyable. I acknowledge the efforts put by all canteen staff, cleaners, security personnel, librarians, plumbers, electricians, housekeeping, and caretakers of the sports complex in making life at IMSc a worry-free and healthy experience.

I would also like to thank all the people whom I have come across during my time at IMSc, there are so many and I must have learned something from each one of them. Special thanks to my dearest of friends: Anirban, Prasanna, Priyamvad, Vasan; none of this would have been possible without their support. I would like to mention some of my friends and seniors: Anand, Anantha, Ankita, Anupama, Anvy, Arindam, Arnab, Arun, Chandrasekhar, Chaoba, Dheeraj, Dibyakrupa, Dipanjan, Goutam, Issan, Jilmy, Madhu, Minati, Pianki, Prathik, Pratibha, Prosenjit, Pulak, Raghu, Ramanathan, Rathul, Ria, Sagnik, Sanjay, Shilpa, Sibasish, Sidharth, Sohan, Sreeraj, Sridhar, Sumit, Varuni. I would also like to thank some of my juniors whose company I shall miss: Amit, Anjali, Anupam, Chandrani, Mrigendra, Pavitra, Pritam, Ramit, Surabhi. I also thank the people I have met in the IMSc sports complex, thank you for the lessons, memories, and entertainment.

I would like to acknowledge the love and support of my Ravenshaw seniors and friends, without them this particular journey would not have begun.

Finally, I am grateful to my grandparents, parents, my little sister, friends, and relatives for their love and care over all these years. I hope, I would be able to stand up to their expectations.

Contents

List of Tables

List of Figures

Chapter 1

Synopsis

Introduction and Motivation

In today's world, the Standard Model (SM) is a well-established theory that comes the closest to explaining our universe. It is theoretically self-consistent and can accommodate three of four known fundamental forces. The SM is also very good at explaining experimental observations and predicting a wide variety of phenomena. However, its failure to include Gravity and to account for various observed phenomena: the observed baryon asymmetry, dark matter, neutrino oscillations, etc., makes it fall short of being a complete theory. As a result, we have to extend this theory or build new models that could fill the void left by SM. Such frameworks are referred to as Beyond Standard Model (BSM) physics or New Physics (NP). The existence of the BSM physics can be confirmed either directly through the production of new particles at collider experiments or indirectly through precision measurements. The direct searches, however, can only probe up to a certain energy scale whereas indirect searches are sensitive to much higher scales as they involve looking for effects of virtual high energy particles through loop induced processes. Without much success, yet, in direct detection at colliders and the availability of high-precision experiments, we have to turn to indirect searches for discovering NP. However, in order to make reliable claims on potential new physics discoveries, we require theoretical tools that could give precise and robust predictions.

In this thesis, we have focused on B-meson decays. We begin with the mode $B \to K^*\ell^+\ell^-$, a promising hotbed for indirect searches. Here, the angular distributions of the decay products lead to a very large number of observables which helps in reducing theoretical uncertainties. Consequently, a lot of effort has been put in this mode in search of NP, most of which are focused on the low di-lepton invariant mass squared region $q^2 = 1-6$ GeV^2. We, on the contrary, have funneled our efforts onto the $q^2_{\rm max}$ region, where we obtain a 5σ signal of right-handed currents using the latest LHCb measurements. In this kinematic limit, we work with heavy quark symmetries which are completely reliable making our conclusion free of hadronic uncertainties. We have also studied the impact of resonances and systematic effects on our claims.

One of many other means of indirect searches of NP is testing the unitarity of the CKM matrix. The unitarity of the CKM matrix imposes very strong constraints on the standard model, violation of which will firmly establish the presence of NP. An extensive amount of continuous and consistent effort has been put in testing the unitarity triangles as accurately as possible. There are collaborations that are dedicated to measuring the phases of some of these triangles e.g. α, β, and γ. Out of these three phases, the phase α is the one that concerns us here. Using an isospin framework, the phase α is measured directly using experimental observations for $B \to \pi\pi$ and $B \to \rho\rho$ modes. The contributions coming from the electroweak penguins are ignored in this method as they are expected to be tiny in SM. However, they are sensitive to NP and must be accounted for. Moreover, with experimental measurements becoming more and more precise, the effects such as the pollution in α measurement due to non-zero electroweak penguins will become more and more relevant. We have presented a clear way to approach the problem of ignoring them. The thesis is organized in the following chapters.

Right-Handed currents in $B \to K^*\ell^+\ell^-$

The decay $B \to K^*\ell^+\ell^-$ can be fully described in the massless lepton limit through six transversity amplitudes [1–4]:

$$\mathcal{A}_\lambda^{L,R} = C^\lambda_{L,R}\mathcal{F}_\lambda - \widetilde{\mathcal{G}}_\lambda = (\widetilde{C}_9^\lambda \mp C_{10})\mathcal{F}_\lambda - \widetilde{\mathcal{G}}_\lambda. \tag{1.1}$$

This parametric form is generic and incorporates all short-distance, long-distance, factorizable, non-factorizable and resonance contributions along with the full electromagnetic corrections to hadronic operators. The effective Wilson coefficient $\widetilde{C}_9^\lambda$ is defined as [1,5,6]

$$\widetilde{C}_9^\lambda = C_9 + \Delta C_9^{(\text{fac})}(q^2) + \Delta C_9^{\lambda,(\text{non-fac})}(q^2)\ . \tag{1.2}$$

However, C_{10} is unaffected by electromagnetic corrections [7]. $\mathcal{F}_\lambda$, $\widetilde{\mathcal{G}}_\lambda$ are q^2 dependent form factors, where q^2 is square of the difference in momentum between B and K^*, with units of GeV^2. In order to distinguish the imaginary contributions coming from $\widetilde{C}_9^\lambda$ and $\widetilde{\mathcal{G}}_\lambda$ we redefine the amplitudes as [1]

$$\begin{aligned} \mathcal{A}_\lambda^{L,R} &= (\mp C_{10} - r_\lambda)\mathcal{F}_\lambda + i\varepsilon_\lambda, \\ \text{where}\quad r_\lambda &= \frac{\text{Re}(\widetilde{\mathcal{G}}_\lambda)}{\mathcal{F}_\lambda} - \text{Re}(\widetilde{C}_9^\lambda), \qquad \varepsilon_\lambda = \text{Im}(\widetilde{C}_9^\lambda)\mathcal{F}_\lambda - \text{Im}(\widetilde{\mathcal{G}}_\lambda). \end{aligned} \tag{1.3}$$

The relevant observables for this analysis: $F_\perp$, $F_\parallel$, F_L, A_{FB} and A_5 are defined as,

$$\begin{aligned} \Gamma_f &\equiv \sum_\lambda (|\mathcal{A}_\lambda^L|^2 + |\mathcal{A}_\lambda^R|^2), \quad F_\lambda = \frac{|\mathcal{A}_\lambda^L|^2 + |\mathcal{A}_\lambda^R|^2}{\Gamma_f} \quad \lambda \in \{\perp, \parallel, 0\}, \\ A_{\text{FB}} &= \frac{3}{2}\frac{\text{Re}(\mathcal{A}_\parallel^L\mathcal{A}_\perp^{L^*} - \mathcal{A}_\parallel^R\mathcal{A}_\perp^{R^*})}{\Gamma_f}, \quad A_5 = \frac{3}{2\sqrt{2}}\frac{\text{Re}(\mathcal{A}_0^L\mathcal{A}_\perp^{L^*} - \mathcal{A}_0^R\mathcal{A}_\perp^{R^*})}{\Gamma_f}. \end{aligned} \tag{1.4}$$

The inclusion of right-handed currents introduces two new Wilson coefficients C_9' and C_{10}' [7] in the amplitudes:

$$\begin{aligned} \mathcal{A}_\perp^{L,R} &= ((\widetilde{C}_9^\perp + C_9') \mp (C_{10} + C_{10}'))\mathcal{F}_\perp - \widetilde{\mathcal{G}}_\perp \\ \mathcal{A}_\parallel^{L,R} &= ((\widetilde{C}_9^\parallel - C_9') \mp (C_{10} - C_{10}'))\mathcal{F}_\parallel - \widetilde{\mathcal{G}}_\parallel \end{aligned}$$

$$\mathcal{A}_0^{L,R} = ((\widetilde{C}_9^0 - C_9') \mp (C_{10} - C_{10}'))\mathcal{F}_0 - \widetilde{\mathcal{G}}_0. \tag{1.5}$$

Notice that the RH-currents affect the perpendicular helicity differently, this is a key observation for this analysis. The observables under the influence of RH-currents gets modified as:

$$F_\perp = 2\zeta\,(1+\xi)^2(1+R_\perp^2), \tag{1.6}$$

$$F_\parallel \mathsf{P}_1^2 = 2\zeta\,(1-\xi)^2(1+R_\parallel^2), \tag{1.7}$$

$$F_L \mathsf{P}_2^2 = 2\zeta\,(1-\xi)^2(1+R_0^2), \tag{1.8}$$

$$A_{\rm FB}\mathsf{P}_1 = 3\zeta\,(1-\xi^2)(R_\parallel + R_\perp), \tag{1.9}$$

$$\sqrt{2}A_5\mathsf{P}_2 = 3\zeta\,(1-\xi^2)(R_0 + R_\perp), \tag{1.10}$$

$$\text{where}\ \ \xi = \frac{C_{10}'}{C_{10}},\ \ \xi' = \frac{C_9'}{C_{10}},\ \ \mathsf{P}_1 = \frac{\mathcal{F}_\perp}{\mathcal{F}_\parallel},\ \ \mathsf{P}_2 = \frac{\mathcal{F}_\perp}{\mathcal{F}_0},\ \ \zeta = \frac{\mathcal{F}_\perp^2 C_{10}^2}{\Gamma_f},$$

$$R_\perp = \frac{\dfrac{r_\perp}{C_{10}} - \xi'}{1+\xi},\ R_\parallel = \frac{\dfrac{r_\parallel}{C_{10}} + \xi'}{1-\xi},\ R_0 = \frac{\dfrac{r_0}{C_{10}} + \xi'}{1-\xi}. \tag{1.11}$$

The theoretical parameters can be solved in terms of experimentally measured observables and P_1:

$$R_\perp = \pm\frac{3}{2}\frac{\left(\frac{1-\xi}{1+\xi}\right)F_\perp + \frac{1}{2}\mathsf{P}_1 Z_1}{\mathsf{P}_1 A_{\rm FB}}, \tag{1.12}$$

$$R_\parallel = \pm\frac{3}{2}\frac{\left(\frac{1+\xi}{1-\xi}\right)\mathsf{P}_1 F_\parallel + \frac{1}{2}Z_1}{A_{\rm FB}}, \tag{1.13}$$

$$R_0 = \pm\frac{3}{2\sqrt{2}}\frac{\left(\frac{1+\xi}{1-\xi}\right)\mathsf{P}_2 F_L + \frac{1}{2}Z_2}{A_5}, \tag{1.14}$$

$$\mathsf{P}_2 = \frac{\left(\frac{1-\xi}{1+\xi}\right)2\mathsf{P}_1 A_{\rm FB} F_\perp}{\sqrt{2}A_5\left(\left(\frac{1-\xi}{1+\xi}\right)2F_\perp + Z_1\mathsf{P}_1\right) - Z_2\mathsf{P}_1 A_{\rm FB}}, \tag{1.15}$$

with

$$Z_1 = \sqrt{4F_\parallel F_\perp - \frac{16}{9}A_{\rm FB}^2} \quad \text{and} \quad Z_2 = \sqrt{4F_L F_\perp - \frac{32}{9}A_5^2}. \tag{1.16}$$

In order to solve all desired parameters we need to eliminate one parameter. Incidentally, at $q^2_{\rm max}$ the heavy quark symmetries provide a relation among the ratios of form factors [8] which can be used to eliminate one parameter:

$$\frac{\widetilde{\mathcal{G}}_{\|}}{\mathcal{F}_{\|}} = \frac{\widetilde{\mathcal{G}}_{\perp}}{\mathcal{F}_{\perp}} = \frac{\widetilde{\mathcal{G}}_{0}}{\mathcal{F}_{0}} = -\kappa\frac{2m_b m_B C_7}{q^2}, \tag{1.17}$$

where $\kappa \approx 1$. From Eq. (1.3) and Eq. (1.17) we get $r_0 = r_{\|} = r_{\perp} \equiv r$ [9] at $q^2_{\rm max}$ in SM. Since Eq. (1.17) still holds in presence of RH-currents, the above relation translates to

$$R_0 = R_{\|} \neq R_{\perp} \quad \text{at} \quad q^2_{\rm max}. \tag{1.18}$$

We note that this relation is not affected by non-factorizable, and resonance contributions. Hence, it could provide conclusive evidence of RH-currents.

At $q^2_{\rm max}$ limit, the physical amplitudes are constrained from kinematics, and symmetries which lead to very unique values of the observables [1, 10] i.e.

$$\begin{aligned}
&F_L(q^2_{\rm max}) = \frac{1}{3}, F_{\|}(q^2_{\rm max}) = \frac{2}{3}, A_4(q^2_{\rm max}) = \frac{2}{3\pi},\\
&F_{\perp}(q^2_{\rm max}) = 0,\ A_{\rm FB}(q^2_{\rm max}) = 0,\ A_{5,7,8,9}(q^2_{\rm max}) = 0.
\end{aligned} \tag{1.19}$$

The RH-currents do not alter these values; instead, they can affect the observable's approach to these values. Our objective is to study R_λ in the limit $q^2 \to q^2_{\rm max}$. We begin with Taylor expanding the transversity amplitudes around $q^2_{\rm max}$ in terms of $\delta \equiv q^2_{\rm max} - q^2$. Considering the limiting values in Eq. (1.19) and the relative momentum dependence of $\mathcal{A}^{L,R}_\lambda$, the observables are expanded as

$$\begin{aligned}
F_L &= \frac{1}{3} + F_L^{(1)}\delta + F_L^{(2)}\delta^2 + F_L^{(3)}\delta^3\\
F_{\perp} &= F_{\perp}^{(1)}\delta + F_{\perp}^{(2)}\delta^2 + F_{\perp}^{(3)}\delta^3\\
A_{\rm FB} &= A_{\rm FB}^{(1)}\delta^{1/2} + A_{\rm FB}^{(2)}\delta^{3/2} + A_{\rm FB}^{(3)}\delta^{5/2}\\
A_5 &= A_5^{(1)}\delta^{1/2} + A_5^{(2)}\delta^{3/2} + A_5^{(3)}\delta^{5/2}.
\end{aligned} \tag{1.20}$$

Where, the $O^{(n)}$ is the coefficient of the $n^{\rm th}$ term in the expansion of the observable

$\mathcal{O}$. Note that, these simple polynomial expansions are limited in accounting for resonance contributions. With similar expansions for the amplitudes, Eq. (1.17) in the limit $q^2 \to q^2_{\rm max}$ turns out to be

$$q^2 \frac{\widetilde{\mathcal{G}}_\lambda}{\mathcal{F}_\lambda} = q^2_{\rm max} \frac{\widetilde{\mathcal{G}}^{(1)}_\lambda + \delta\,(\widetilde{\mathcal{G}}^{(2)}_\lambda - \dfrac{\widetilde{\mathcal{G}}^{(1)}_\lambda}{q^2_{\rm max}}) + \mathcal{O}(\delta^2)}{\mathcal{F}^{(1)}_\lambda + \delta\,\mathcal{F}^{(2)}_\lambda + \mathcal{O}(\delta^2)}. \tag{1.21}$$

In general, Eq. (1.21) must be satisfied at all orders in δ; but we only require it to be valid till δ order. For Eq. (1.21) to have a constant value in the neighborhood of $q^2_{\rm max}$ up to $\mathcal{O}(\delta)$, we require that $\mathcal{F}^{(2)}_\lambda = c\,\mathcal{F}^{(1)}_\lambda$ and $(q^2_{\rm max}\,\widetilde{\mathcal{G}}^{(2)}_\lambda - \widetilde{\mathcal{G}}^{(1)}_\lambda) = c\, q^2_{\rm max}\,\widetilde{\mathcal{G}}^{(1)}_\lambda$ where c is any constant. Since $\mathsf{P}_2 = \sqrt{2}\mathsf{P}_1$ at $q^2_{\rm max}$, we must have $\mathsf{P}^{(1)}_2 = \sqrt{2}\mathsf{P}^{(1)}_1$ where $\mathsf{P}^{(1)}_{1,2}$ are the coefficients of the leading $\mathcal{O}(\sqrt{\delta})$ term in the expansion. The above arguments also imply that at the next order, we must have $\mathsf{P}^{(2)}_2 = \sqrt{2}\mathsf{P}^{(2)}_1$, as $\mathcal{F}^{(2)}_\lambda = c\,\mathcal{F}^{(1)}_\lambda$. This extra input lets us eliminate P_1. Given this, R_λ at $q^2_{\rm max}$ can be expressed as follows:

$$\begin{aligned} R_\perp(q^2_{\rm max}) &= \frac{8A^{(1)}_{\rm FB}(-2A^{(2)}_5 + A^{(2)}_{\rm FB}) + 9(3F^{(1)}_L + F^{(1)}_\perp)F^{(1)}_\perp}{8\,(2A^{(2)}_5 - A^{(2)}_{\rm FB})\,\sqrt{\frac{3}{2}F^{(1)}_\perp - A^{(1)\,2}_{\rm FB}}} \\ &= \frac{\omega_2 - \omega_1}{\omega_2\,\sqrt{\omega_1 - 1}}, \end{aligned} \tag{1.22}$$

$$\begin{aligned} R_\|(q^2_{\rm max}) &= \frac{3(3F^{(1)}_L + F^{(1)}_\perp)\,\sqrt{\frac{3}{2}F^{(1)}_\perp - A^{(1)\,2}_{\rm FB}}}{-8A^{(2)}_5 + 4A^{(1)}_{\rm FB} + 3A^{(1)}_{\rm FB}(3F^{(1)}_L + F^{(1)}_\perp)} \\ &= \frac{\sqrt{\omega_1 - 1}}{\omega_2 - 1} = R_0(q^2_{\rm max}) \end{aligned} \tag{1.23}$$

$$\text{where} \quad \omega_1 = \frac{3}{2}\frac{F^{(1)}_\perp}{A^{(1)\,2}_{\rm FB}} \quad \text{and} \quad \omega_2 = \frac{4\,(2A^{(2)}_5 - A^{(2)}_{\rm FB})}{3\,A^{(1)}_{\rm FB}(3F^{(1)}_L + F^{(1)}_\perp)}. \tag{1.24}$$

As seen above $R_\lambda(q^2_{\rm max})$ depends only on the polynomial coefficients $F^{(1)}_L$, $F^{(1)}_\perp$, $A^{(2)}_{\rm FB}$ and $A^{(2)}_5$ which are not related by HQET. Hence, the claims made here are model independent.

We perform a χ^2 polynomial fit of the observables F_L, $F_\perp$, $A_{\rm FB}$ and A_5 (Eq.(1.20)) to the latest LHCb 14-bin data [11] as functions of q^2. The integrations involved are weighted with recently measured differential decay rates [12]. The fits show good convergence

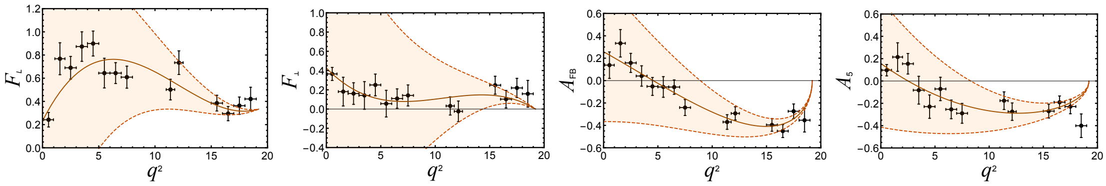

Figure 1.1: The polynomial fits for F_L, $F_\perp$, $A_{\rm FB}$ and A_5 are shown. The solid brown curve at the center correspond to the third order polynomial seen in Eq. (1.20). The dashed brown lines along with the light brown shaded region illustrates the $\pm 1\sigma$ error bands of the central polynomial fit. The black cross marks depict the LHCb measurements [11] and their errors. The q^2 is in units of GeV^2.

for 2nd-4th order polynomials and 10-14 bins. The various systematics of these fits are analyzed extensively. The best fit values for the Taylor coefficients of F_L, $F_\perp$, $A_{\rm FB}$ and A_5 in Eq. (1.20) are given in Table. 1.1. The errors are obtained through covariance matrix method. The best fit 3rd order polynomial for F_L, $F_\perp$, $A_{\rm FB}$ and A_5 along with their 1σ

	$\mathcal{O}^{(1)}(10^{-2})$	$\mathcal{O}^{(2)}(10^{-3})$	$\mathcal{O}^{(3)}(10^{-4})$
F_L	-2.85 ± 1.26	12.13 ± 1.90	-5.68 ± 0.67
$F_\perp$	6.89 ± 1.65	-9.79 ± 2.47	3.83 ± 0.86
$A_{\rm FB}$	-30.58 ± 1.95	26.96 ± 3.58	-4.15 ± 1.47
A_5	-15.85 ± 1.87	5.38 ± 3.33	2.46 ± 1.29

Table 1.1: The best fit values along with their $\pm 1\sigma$ errors for coefficients of the observables in Eq. (1.20) are shown. These values are obtained by fitting the bin-averaged values of the observables to the LHCb 's 14-bin measurements [11].

error bands are given in Fig. 1.1.

The $R_\perp$ and $R_{\parallel,0}$ values are estimated in two different ways. In first method, we use Eq. (1.24) and the coefficient values from Table. 1.1 to get ω_1 and ω_2. Then using Eq. (1.22)-(1.23) we fit R_λ. The results are shown in Fig. 1.2. The contours should be aligned along the 45$^{\rm o}$ straight line in SM as the resonances contribute equally across the helicities. Hence, this deviation indicates a strong presence of RH currents.

In second approach, we have taken $F_L^{(1)}$, $F_P^{(1)}$, $A_{\rm FB}^{(1)}$, $A_5^{(1)}$, $A_{\rm FB}^{(2)}$ and $A_5^{(2)}$ as Gaussian distributions around their central values(see Table. 1.1). Then R_λ are estimated using Eq. (1.22)-(1.24). These values should lie along a straight line with a 45$^{\rm o}$ slope in the $R_\perp - R_{\parallel,0}$ plane in SM. However, we find a slope that is nearly 0$^{\rm o}$, indicating that $R_\perp \gg R_{\parallel,0}$. This deviation is a strong indirect evidence of RH currents.

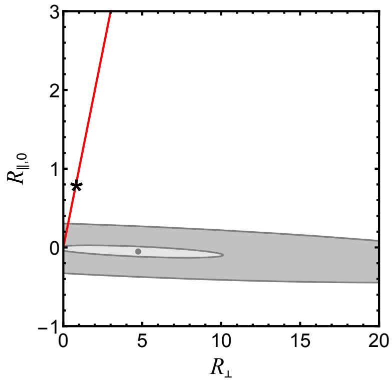

Figure 1.2: The estimated contours of R_λ in $R_\perp - R_{\|,0}$ plane are shown. The predicted 1σ and 5σ confidence levels are shown in light and dark gray contours, respectively. The gray point at the center of 1σ contour indicates the best fit value. The black star corresponds to the SM estimate. The solid red straight line represents the $R_\perp = R_{\|,0}$.

We use Eq. (1.11) to estimate C_9' and C_{10}' from ξ and ξ'. However this extraction depends on the value of r/C_{10} at $q^2_{\rm max}$, see Eq. (1.11). Though we have an SM estimate for this quantity, it can change due to contributions within SM e.g. errors in Wilson coefficients or contributions from other kinds of new physics or from the effects of resonances. Some of possible scenarios are considered in Fig. 1.3. Using SM estimate i.e. $r/C_{10} = 0.84$ [8] the best fit values of ξ and ξ', with $\pm1\sigma$ errors are -0.63 ± 0.43 and -0.92 ± 0.10, respectively. The value $r/C_{10} = 0.6$ corresponds to a scenario in which NP contribution to C_9 is $C_9^{\rm NP} \approx -1$, see [13]. In this case, best fit values of ξ and ξ' with $\pm1\sigma$ errors are -0.73 ± 0.32 and -0.69 ± 0.10. In another analysis,we have considered r/C_{10} as a nuisance parameter and the results are given in right panel of Fig. 1.3. As seen in Fig. 1.3, though uncertainties have increased there is still a 3σ evidence for RH currents.

The complex contributions to the transversity amplitudes i.e ε_λ (in Eq. (1.3)) are incorporated according to Ref. [1]. The $\hat{\varepsilon}_\lambda \equiv 2|\varepsilon_\lambda|^2/\Gamma_f$ have been Taylor expanded around $q^2_{\rm max}$ and LHCb data has been used to estimate their coefficients. The resulting $\omega_{1,2}$ values are $\omega_1 = 1.03 \pm 0.31(0.98 \pm 0.29)$ and $\omega_2 = -4.52 \pm 17.40(-3.94 \pm 9.86)$. These have insignificant difference to the values obtained for the real case.

The finite width of the K^* has been taken into account by varying $q^2_{\rm max}$ between $18.34 - 20.10$ GeV^2. The $\omega_{1,2}$ values turn out to be $\omega_1 = 1.11 \pm 0.30$ (1.03 ± 0.35) and $\omega_2 = -3.56 \pm 28.34$ (-3.50 ± 27.44). Again these have insignificant effect on Fig. 1.1-1.3.

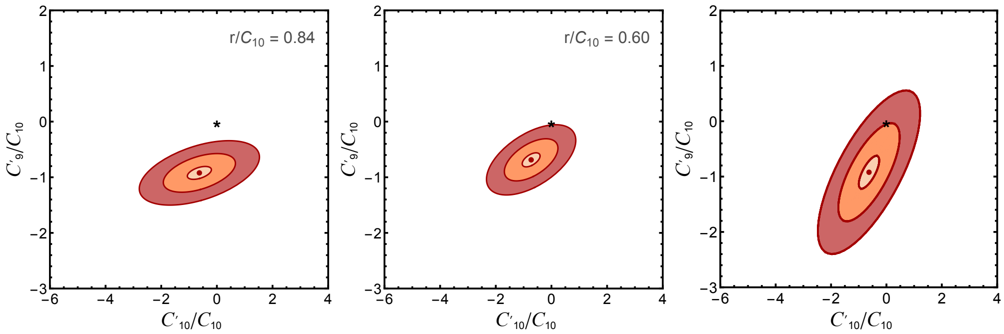

Figure 1.3: The predicted regions in ξ - ξ' plane are shown. The yellow, orange and red contours correspond to 1σ, 3σ and 5σ confidence levels, respectively. The red dot at center indicates the best fit value. The black star correspond to the SM estimate of C'_{10}/C_{10} and C'_9/C_{10}. These plots illustrate the sensitivity of ξ, and ξ' to r/C_{10}. The figure in the first panel corresponds to ξ - ξ' contours generated using the SM estimate of $r/C_{10} = 0.84$ [8] and the SM value of ξ, and ξ' lied beyond 5σ confidence level. The estimates in the second panel correspond to $r/C_{10} = 0.60$ which coincides with an additional NP contribution $C_9^{\rm NP} \approx -1$ [13]. The estimates on the last panel result from treating r/C_{10} as a nuisance parameter where the SM value is lying on the edge of 3σ confidence level.

We test the convergence of our polynomial fits by varying the order of polynomials along with the number of bins used from 4-14. The results are summarized in Fig. 1.4. We have chosen 3rd order polynomial fitted to 14-bins as our benchmark fit and have justified this choice through a third order polynomial fit to the SM simulated 14-bin data of the observables, see Fig. 1.5.

We have also done a comprehensive study about the impact of resonance contributions on our claims. We find that the data does not have significant resonance contributions and if the resonance contributions could somehow be isolated from the signal data then the significance of RH currents would actually increase.

Electroweak penguins in $B \to \pi\pi$ and $B \to \rho\rho$

The $B \to \pi\pi$ and $B \to \rho\rho$ modes are used for direct α measurements. An isospin framework is used to describe the decay amplitudes. The $B^0 \to \pi^+\pi^-$, $B^0 \to \pi^0\pi^0$ and $B^+ \to \pi^+\pi^0$ decay amplitudes (denoted as A^{+-}, A^{00} and A^{+0}, respectively) in terms of the isospin

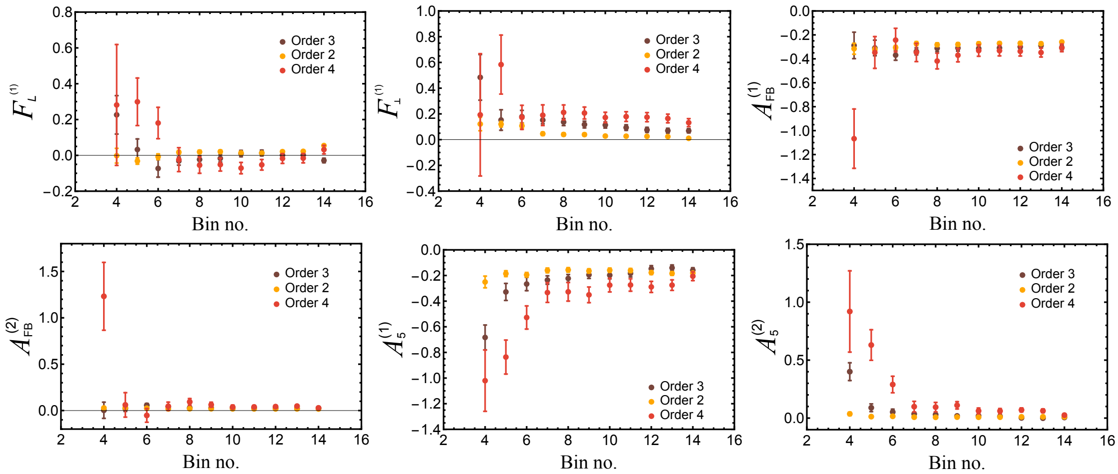

Figure 1.4: A summary of the fit coefficient values and their $\pm 1\sigma$ errors are shown here. The coefficients are obtained by varying the order of the polynomials as well as the number of bin averaged values considered in the data set. The color code for different orders of the polynomial are shown in each panel. The $x-$axis denotes the number of bin averaged values used in the fit. The $y-$ axis denotes the value taken by these coefficients. The best fit values of the coefficients are given by circular dots while the vertical bars through them denote $\pm 1\sigma$ errors. The thin gray line indicates the value zero.

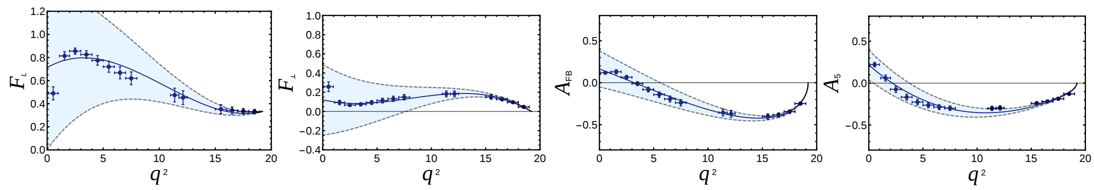

Figure 1.5: The third order polynomial fits to 14-bin SM simulated data are shown here. The q^2 is in units of GeV^2. The blue central curve is the best fit while the dashed blue curves along with the light blue shaded region illustrate $\pm 1\sigma$ region surrounding the best fit. The blue crosses depict the corresponding observable data points which are generated using LCSR form factors for $q^2 \leq 15\,\mathrm{GeV}^2$ and Lattice QCD form factors for $q^2 \geq 15\,\mathrm{GeV}^2$.

amplitudes corresponding to $I = 0$ and $I = 2$ final states (A_0 and A_2, respectively) [14]:

$$\begin{aligned}\frac{1}{\sqrt{2}}A^{+-} &= A_2 - A_0,\\ A^{00} &= 2A_2 + A_0,\\ A^{+0} &= 3A_2.\end{aligned} \tag{1.25}$$

It is clear that the decay amplitudes satisfy the relations:

$$\frac{1}{\sqrt{2}}A^{+-} + A^{00} = A^{+0}, \tag{1.26}$$

$$\frac{1}{\sqrt{2}}\bar{A}^{+-} + \bar{A}^{00} = \bar{A}^{+0}. \tag{1.27}$$

The amplitudes $\bar{A}^{+-}$, $\bar{A}^{00}$ and $\bar{A}^{+0}$ correspond to the charge-conjugated processes $\bar{B}^0 \to \pi^+\pi^-$, $\bar{B}^0 \to \pi^0\pi^0$ and $B^- \to \pi^-\pi^0$, respectively. In terms of graph contributions they are given by [15, 16]

$$\begin{aligned}
\frac{1}{\sqrt{2}}A^{+-} &= (T+E)e^{i\gamma} + (P + \frac{2}{3}P^C_{EW})e^{-i\beta}, \\
A^{00} &= (C-E)e^{i\gamma} + (P_{EW} + \frac{1}{3}P^C_{EW} - P)e^{-i\beta}, \\
A^{+0} &= (T+C)e^{i\gamma} + (P_{EW} + P^C_{EW})e^{-i\beta}.
\end{aligned} \tag{1.28}$$

The complex topologies T, C, P, P_{EW} and P^C_{EW} are referred as “tree", “color-suppressed-tree", “penguin", “electroweak-penguin" and “color-suppressed electroweak-penguin" amplitudes correspondingly, include strong phases. With some manipulations and redefinitions, the decay amplitudes become

$$\begin{aligned}
\frac{1}{\sqrt{2}}\tilde{A}^{+-} &= (T+E) + Xe^{i\alpha}, \\
\tilde{A}^{00} &= (C-E) + Ye^{i\alpha}, \\
\tilde{A}^{+0} &= (T+C) + (X+Y)e^{i\alpha},
\end{aligned} \tag{1.29}$$

where, $X = (-P - \frac{2}{3}P^C_{EW})$ and $Y = (P - P_{EW} - \frac{1}{3}P^C_{EW})$. The corresponding conjugate amplitudes are given by switching the sign of the weak phase α. An important observation at this point is that the quantity $X+Y(=-P_{EW} - P^C_{EW})$ depends on the electroweak and color suppressed electroweak penguins alone [15]. In other words, $X+Y$ serves as a measure of pure electroweak contributions in $B \to \pi\pi$ modes. The two triangles corresponding to the isospin relations could be solved using the branching fractions B_{ij}, direct CP asymmetries C_{ij}, and the associated time-dependent CP asymmetry S_{ij}, up to some ambiguity. However, in the absence of any measurements for S_{00} we need one extra piece of information. We have chosen the indirect measured value of α to be this extra input.

Our primary objective is to estimate the size of electroweak contributions or $X+Y$. For a better grasp on the numbers, we normalize our hadronic parameters by the dominant tree contributions $|T+C|$ and define the desired quantities as $\mathcal{R}_P = \{\tilde{X}, \tilde{Y}, \tilde{X}+\tilde{Y}\}$:

$$\tilde{X} = \frac{X}{|T+C|}, \quad \tilde{Y} = \frac{Y}{|T+C|},$$
$$\tilde{X}+\tilde{Y} = \frac{X+Y}{|T+C|} \equiv z e^{i\delta_{TC}},$$

where z is defined in Eq. (1.32) and δ_{TC} is the strong phase of $T+C$. The $B^{\pm} \to \pi^{\pm}\pi^{0}$ decay only gets contribution from $\Delta I = \frac{3}{2}$ part of the Hamiltonian. In presence of electroweak penguins, $\Delta I = \frac{3}{2}$ operators has both tree and electroweak penguin contributions; and they can be related by assuming that only C_7 and C_8 are neglected [17]:

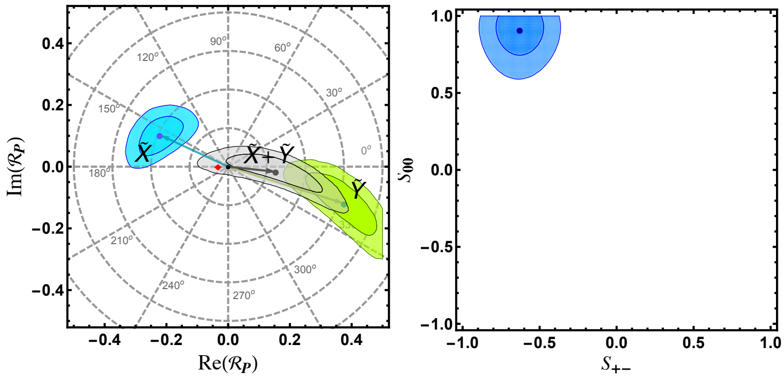

Figure 1.6: The estimated 68.27% and 95.45% confidence levels for the topological ratios (left panel) and S_{00} versus S_{+-} (right panel) for $B \to \pi\pi$ modes are depicted. The light gray, light blue and light green contours correspond to the topological ratios $\tilde{X}+\tilde{Y}$, $\tilde{X}$ and $\tilde{Y}$, respectively. The gray, blue and green points show the mean value of the PDFs corresponding to $\tilde{X}+\tilde{Y}$, $\tilde{X}$ and $\tilde{Y}$, respectively and similarly the vectors connecting them to the origin. The'•' at the center indicates origin while the '♦' symbol at −0.0327 indicates the SM estimate for z.

$$\mathcal{H}^{EW}_{\Delta I=\frac{3}{2}} = -\frac{3}{2}\frac{V_{tb}V_{td}}{V_{ub}V_{ud}}\frac{C_9+C_{10}}{C_1+C_2}\mathcal{H}^{\text{tree}}_{\Delta I=\frac{3}{2}} \tag{1.30}$$

The amplitudes $\tilde{\bar{A}}^{+0}$, $\tilde{A}^{+0}$ can be expressed here as

$$\tilde{A}^{+0} = (T+C) + z e^{i\alpha}(T+C),$$
$$\tilde{\bar{A}}^{+0} = (T+C) + z e^{-i\alpha}(T+C), \tag{1.31}$$

where,

$$z = -\frac{3}{2}\left|\frac{V_{tb}V_{td}}{V_{ub}V_{ud}}\right|\frac{C_9+C_{10}}{C_1+C_2} \approx -0.013\left|\frac{V_{tb}V_{td}}{V_{ub}V_{ud}}\right|. \tag{1.32}$$

Eq. (1.32) serves as a theoretical estimate for z in this analysis. The value of ratio of CKM elements $(V_{tb}V_{td})/(V_{ub}V_{ud})$ are taken from Ref. [18].

Once the triangles are fully solved in terms of the observables, we can easily estimate $\mathcal{R}_P$. We generate the 68.27% and 95.45% confidence levels of $\mathcal{R}_P$ and S_{00} for $B \to \pi\pi$ decays. The solution, one of the possible eight, illustrated in Fig. 1.6 shows that the estimate for $\tilde{X}+\tilde{Y}$ agrees with the SM within one standard deviation. As seen in the right panel figure of Fig. 1.6, S_{00} has been estimated to have positive values; however if S_{00} is measured to be negative while rest of the experimental data remain the unchanged then it is clear that we have to discard this solution. In other words, measurement of the time-dependent asymmetry S_{00} can help reduce or even eliminate the ambiguity.

Similar estimates of the topological ratios (left panel) and S_{00} versus S_{+-} (right panel) for $B \to \rho\rho$ are depicted in Fig. 1.7. The details of the figures are same as that of Fig. 1.6. Four of the eight possible solutions are presented here. The estimates for $\tilde{X}+\tilde{Y}$ are in good agreement with SM for all of these four solutions. The remaining four solutions are ignored as they indicate very large penguin contributions and are, in turn, very far from the SM expectations. The gray band in S_{00} versus S_{+-} (right panel) figures correspond to the 1σ region of measured S_{00} for $B^0 \to \rho^0\rho^0$. It is clear that more accurate measurements of S_{00} can help in identifying the correct ambiguity.

We have also analyzed the ratios of redefined isospin amplitudes which are denoted by

$$\mathcal{R}_I = \{\tilde{A}_0/\tilde{A}_2, \tilde{\bar{A}}_0/\tilde{\bar{A}}_2, \tilde{A}_0/\tilde{\bar{A}}_0, \tilde{A}_2/\tilde{\bar{A}}_2\}.$$

The estimates of $\mathcal{R}_I$ for $B \to \pi\pi$ and $B \to \rho\rho$ are shown in Fig. 1.8 and Fig. 1.9, respectively. The light gray, light blue, light green and light orange contours correspond to 68.27% and 95.45% confidence levels of A_0/A_2, $\bar{A}_0/\bar{A}_2$, $A_0/\bar{A}_0$ and $A_2/\bar{A}_2$, respectively. The solutions presented in Fig. 1.8 and Fig. 1.9 correspond to the solutions in Fig. 1.6 and Fig. 1.7, respectively.

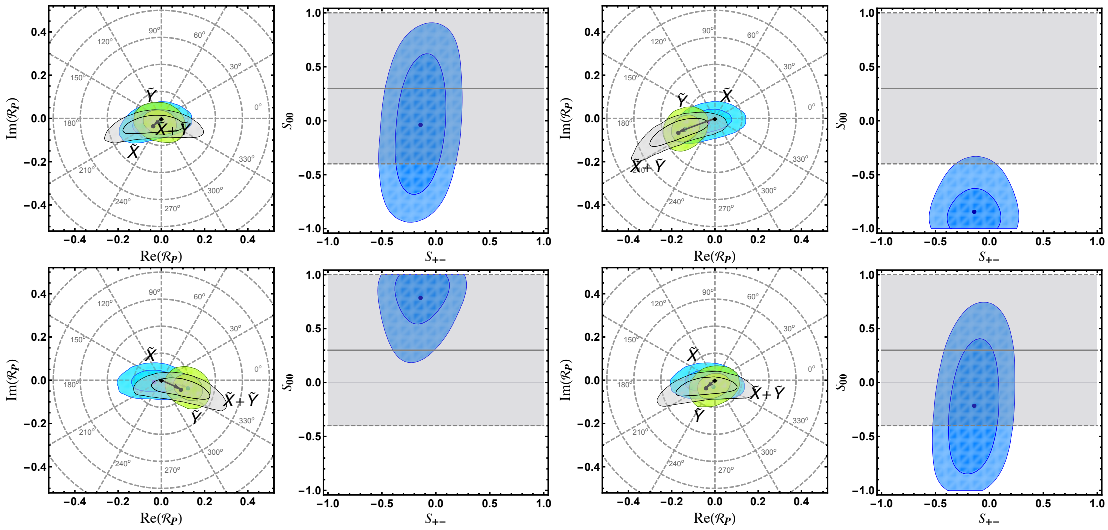

Figure 1.7: The topological amplitudes (left panel) and S_{00} versus S_{+-} (right panel) are depicted for $B \to \rho\rho$ modes. The color codes and other details are the same as in Fig. 1.6. The estimates for $\tilde{X}+\tilde{Y}$ are in good agreement with SM for all of these solutions. The gray band in S_{00} versus S_{+-} (right panel) figures correspond to the 1σ region of measured S_{00} for $B^0 \to \rho^0\rho^0$. It is clear that more accurate measurements of S_{00} can help identifying the correct ambiguity.

We find two sets of hierarchies among $\mathcal{R}_I$ from Fig. 1.8 and 1.9. For $B \to \pi\pi$ we find $|A_2| \approx |\bar{A}_2| \lesssim |A_0| < |\bar{A}_0|$ whereas for $B \to \rho\rho$ we find $|A_2| \approx |\bar{A}_2| < |A_0| \approx |\bar{A}_0|$. It is interesting to observe that in first and the last figure of Fig. 1.9 A_0/A_2 and $\bar{A}_0/\bar{A}_2$ are almost overlapping which leads to a relation among topological amplitudes. The isospin ratios can be written as

$$\begin{aligned}\frac{A_0}{A_2} &= xe^{i\delta_x} + iye^{i\delta_y},\\ \frac{\bar{A}_0}{\bar{A}_2} &= xe^{i\delta_x} - iye^{i\delta_y},\end{aligned} \tag{1.33}$$

where x, y, δ_x and δ_y are complicated function of topological amplitudes and α. Then the overlap of these two implies $y = 0$:

$$\frac{A_0}{A_2} \approx \frac{\bar{A}_0}{\bar{A}_2} \implies y = 0 \implies \frac{C-E}{T+E} \approx \frac{Y}{X}. \tag{1.34}$$

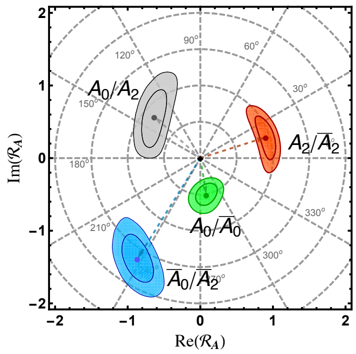

Figure 1.8: The estimated 68.27% and 95.45% confidence levels of $\mathcal{R}_I$ for $B \to \pi\pi$ modes are shown. The gray, blue, green and orange contours correspond to A_0/A_2, $\bar{A}_0/\bar{A}_2$, $A_0/\bar{A}_0$ and $A_2/\bar{A}_2$, respectively. The figures shown corresponds to the solutions presented in Fig. 1.6.

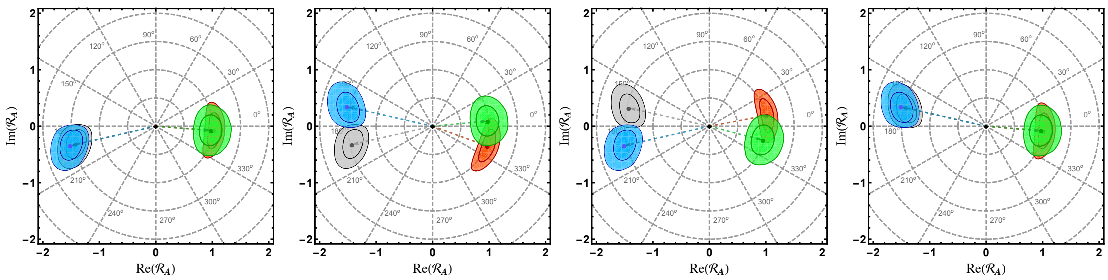

Figure 1.9: The estimated $\mathcal{R}_I$ for $B \to \rho\rho$ are depicted here. The color code and other details are same as of Fig. 1.8.

Conclusions

In this thesis, we have presented a framework which uniquely probes for RH-currents in $B \to K^* \ell^+ \ell^-$ at $q^2_{\rm max}$. The heavy quark symmetries involved in this limit lets us get rid of any dependence on form factor estimates. The observables are kinetically constrained in this limit. Though NP do not alter the values of observables at endpoint, they can alter their approach to these values. In other words the NP affects the first and second derivatives of observables in this limit. It is in these derivatives that we find a deviation from SM with the latest LHCb measurements. These effects quantify to a 5σ evidence of NP at $q^2_{\rm max}$. While the signal for RH currents is evident, other kind of NP contributions could reduce the value of ξ and ξ'. Various systematic studies on our claims are also done. Adopting the theoretical input r/C_{10} as a nuisance parameter still gives us a 3σ signal of NP. We also find that the imaginary contributions of the transversity amplitudes and the finite K^* width have insignificant effect on our results. We also learn that the resonance contributions can not weaken our claims.

In the second part of the thesis, we present a clear approach to address the pollution in α measurements caused by the presence of non-zero electroweak penguins. With the current precision of measurements, we find that the electroweak penguins are consistent with the SM expectation. We find that the precise measurement of S_{00} is very important as it can help in reduce, even eliminate ambiguities. We observe that the estimates for $B \to \rho\rho$ are consistent with SM expectations which implies that the approximations made in studying $B \to \rho\rho$ are reliable. We have generated the isospin amplitudes and a hierarchy among them is noted. Finally, we emphasize that with this approach, future improvements in measurements will definitely make the role of electroweak penguins clear.

Chapter 2

Introduction

2.1 The Standard Model

Throughout the history of mankind, curiosity has guided our scientific evolution. The desire to know the unknown has often led to discoveries that are comprehended in the form of principles, laws, and theories. The saga which had started with concepts promoted by Aristotle (384BC-322BC): "observation of physical phenomena could ultimately lead to the discovery of natural laws governing them" continues to drive physicists even today. It’s inspiring to realize that the moment first of such principles was conceived, we were able to decipher one of the secrets of our physical universe. It also led to the understanding that the universe, as overwhelming as it may appear, was still bound to a simple rule which mankind had just discovered. Thus had started the obsession to study the universe up to its fundamental scales which has led us to where we stand today. In today’s world, we understand that elementary particles are the building blocks of our observable universe which is governed by four fundamental forces: Electromagnetic, Weak, Strong, and Gravitational. In addition, we have also established a theory that could unite three of these forces(i.e Electroweak and Strong) within a single theoretical framework, namely the Standard Model (SM) of particle physics. However, a unified theory governing all four forces is still eluded.

Before we go on to discuss more on SM, we emphasize the role symmetries play in building physical theories. In fact, all of our physical theories are based on symmetry principles. From spacetime symmetry of the special theory of relativity to the gauge symmetries of quantum field theories, they have laid the foundation of modern physical theories. This feature is made explicit in relativistic quantum field theories via Noether's theorem which states that if the action has some symmetry or, in other words, if the action is invariant under some group of transformations, there exist one or more conserved quantities associated to these transformations. In short, symmetries imply conservation laws. Then it's natural to wonder if symmetries could also dictate dynamics, in other words, if we impose certain symmetries on theory then does it affect the dynamics of that theory? Indeed, it does and Quantum Electrodynamics(QED), regarded as the most successful quantum field theory ever written, is an apt example. In particular, the existence and some of the properties of the underlying gauge field, the photon, follows directly from the principle of invariance of local gauge transformation of the $U(1)$ group in this theory. Moreover, these principles could be generalized for other interactions. In fact, in the standard model, this has been accomplished to describe the weak and strong interactions through gauge principles.

The SM Lagrangian consists of three key ingredients:

- the gauge symmetry,
- the representation of its particle content under the gauge symmetry and
- spontaneous symmetry breaking.

The SM gauge group is

$$G_{\mathrm{SM}} = SU(3)_C \times SU(2)_L \times U(1)_Y. \tag{2.1}$$

There are three generations of fermions and their representations under this gauge group are

$$Q_{L\alpha}(3,2)_{+1/6},\ u_{R\alpha}(3,1)_{+2/3},\ d_{R\alpha}(3,1)_{-1/3},\ L_{L\alpha}(1,2)_{-1/2} \text{ and } l_{R\alpha}(1,1)_{-1}. \tag{2.2}$$

The above notation can be comprehended as follows, for example, $Q_{L\alpha}(3,2)_{1/6}$ would mean left-handed quarks are triplets of group $SU(3)_C$, doublets of $SU(2)_L$ and carry hypercharge(Y) $1/6$ while α stands for the flavor. The lone scalar field, ϕ, is represented by

$$\phi(1,2)_{+1/2}. \tag{2.3}$$

In SM, the scalar field assumes a non-zero vacuum expectation value which indicate that the gauge group is spontaneously broken to

$$G_{\mathrm{SM}} \to SU(3)_C \times U(1)_Q. \tag{2.4}$$

The standard model Lagrangian, $\mathcal{L}_{\mathrm{SM}}$, is renormalizable and can in general be divided into three parts such that

$$\mathcal{L}_{\mathrm{SM}} = \mathcal{L}_{\mathrm{kinetic}} + \mathcal{L}_{\mathrm{Higgs}} + \mathcal{L}_{\mathrm{Yukawa}}. \tag{2.5}$$

$\mathcal{L}_{\mathrm{kinetic}}$ describes the self-interactions of the gauge fields along with their interactions with the fermions i.e.

$$\mathcal{L}_{\mathrm{kinetic}} = -\frac{1}{4}\sum F^a_{\mu\nu}F^{\mu\nu}_a + \sum \bar{\psi} i \not{D} \psi. \tag{2.6}$$

The covariant derivative is defined to ensure the theory is gauge invariant and takes the following form in general,

$$D_\mu = \partial_\mu + i g_s G^a_\mu L_a + i g W^b_\mu T_b + i g' B_\mu Y. \tag{2.7}$$

Here G^a_μ represents the gluon fields while W^b_μ and B_μ represent the weak bosons and the hypercharge boson, respectively. The L_a and T_b are $SU(3)_C$ and $SU(2)_L$ generators, respectively, while Y's are the $U(1)_Y$ charges. The g_s, g and g' are theory parameters.

The Higgs part of the Lagrangian includes the mass term as well as the self interactions of the Higgs field,

$$\mathcal{L}_{\text{Higgs}} = |D_\nu \phi|^2 + \mu^2 \phi^\dagger \phi - \lambda (\phi^\dagger \phi)^2. \tag{2.8}$$

The Higgs potential, $\mu^2 \phi^\dagger \phi - \lambda(\phi^\dagger \phi)^2$, describes EW symmetry breaking. The vacuum stability implies $\lambda > 0$ while the pattern of spontaneous symmetry breaking requires $\mu^2 < 0$.

The Yukawa part of the Lagrangian consists of

$$\mathcal{L}_{\text{Yukawa}} = -Y_{ij}^d \bar{Q}_{Li}^I \phi d_{Rj}^I - Y_{ij}^u \bar{Q}_{Li}^I \tilde{\phi} u_{Rj}^I - Y_{ij}^l \bar{L}_{Li}^I \phi l_{Rj}^I + \text{h.c.} \tag{2.9}$$

where $\tilde{\phi}$ is the conjugate Higgs field. In the absence of Yukawa interactions, i.e. $Y_{ij}^{d,u,l} = 0$, the SM Lagrangian is essentially a sum of covariant kinetic terms $\sum \bar{\psi} i \not{D} \psi$, where the sum runs over all fields in irreducible representations of SM gauge group. Consequently, the Lagrangian stays invariant under linear unitary transformations among the fields in a given representation. Considering that there are 3 copies of SM-representation(or 3 generations of fermions) and 5 distinct SM-representations the full symmetry group becomes $U(3)^5$ and the the arising symmetry is referred to as *flavor symmetry*. The Yukawa interactions are the only source of flavor changing quark interactions in SM. The gauge interactions are divided in to the charged current (CC) and neutral current (NC) interactions:

$$\mathcal{L}_{CC} = \frac{g}{\sqrt{2}} \left(\bar{u}_{L\alpha} \gamma^\mu d_{L\alpha} W_\mu^+ + \bar{e}_{L\alpha} \gamma^\mu \nu_{L\alpha} W_\mu^- \right) + \text{h.c.} \tag{2.10}$$

$$\mathcal{L}_{NC} = e q_f \bar{f} \gamma^\mu f A_\mu + \frac{g}{c_W} \bar{f} \gamma^\mu \left(g_V^f - g_A^f \gamma_5 \right) f Z_\mu \tag{2.11}$$

where g_V^f and g_A^f are the vector and axial vector couplings of Z to fermions, respectively. As evident from the above equation the flavor changing neutral currents (FCNC) are absent in SM.

2.2 Hadronic weak decays and B Physics

The phenomenology of weak decays is very useful in understanding the nature of fundamental interactions. For instance, weak decays can be used to test the standard model and measure its parameters. In particular, the hadronic weak decays are used in direct measurements of the weak mixing angles, analyzing *CP* violation, testing unitarity of the *CKM* matrix, etc. Moreover, some of the hadronic decays are used in indirect searches for NP and depending upon the final decay products, they are categorized into three classes: leptonic decays (having all-lepton final states), semi-leptonic decays (where both leptons and hadrons are present in the final states), and non-leptonic decays (having all-hadron final states). Physically, the quarks are confined inside hadrons which means that the simplicity provided by the weak transitions is often subdued by the complexity of strong interactions that increase with the number of quarks present in the final states. Nonetheless, there are a few established mechanisms to deal with these theoretical challenges. For instance, the bound-state effects in the leptonic decays can be parametrized in terms of single decay constants. While those in semi-leptonic decays are described by invariant form factors that are dependent on the momentum transfer q^2 between the initial and final hadrons. Approximate symmetries of underlying strong interactions help us constrain the properties of some of these form factors. Non-leptonic decays are the most difficult to deal with. However, significant progress has been made in developing theoretical tools to analyze the decays of heavy hadrons. Particularly, the discovery of heavy-quark symmetry, the development of heavy-quark effective theory, and the establishment of various kinds of heavy-quark expansions help in formulating modern theoretical frameworks for the description of the properties and decays of hadrons containing a heavy quark.

As $m_b \gg \Lambda_{\text{QCD}}$, b-quark is considered as heavy. The effective coupling constant for b-quark, $\alpha_s(m_b)$, is small which implies that on length scales comparable to the corresponding Compton wavelength $\lambda_b \sim 1/m_b$, the strong interactions can be treated perturbatively. Moreover, as $\lambda_b \ll R_{\text{had}}$, the heavy quarks inside the hadrons can be treated non-relativistically. For instance, the bottomonium systems ($\bar{b}b$) are well approximated by non-relativistic models like non-relativistic QCD or non-relativistic models of the hydrogen atom. In the hadrons, consisting of a heavy quark and other light quarks, the soft gluon exchanges between the heavy and light quarks are sensitive to scales much larger than λ_b which means the light degrees of freedom are blind to the flavor and spin orientation of the heavy quark. Hence, in the limit $m_b \to \infty$, this observation helps us relate properties of different heavy mesons (e.g. B, D, B^*, D^*) or heavy baryons (e.g. Λ_b, Λ_c) for that matter. The corrections to these heavy quark symmetries arise as the quark masses are not infinite. Similarly, heavy quark effective theories (HQET) and heavy-quark expansions (HQE) are implemented in studying the properties and decays of B-hadrons.

There has been significant progress on the experimental front as well, particularly over the past few decades. A lot of data have been and are being analyzed on the decays of heavy-quark hadrons. B-factories at SLAC, KEK, Cornell, DESY, LHCb, and Belle are focused on studying CP violation and rare B-meson decays. With continuous upgrades, LHCb, and Belle-II are expected to provide data with improved accuracies. We are already witnessing some disagreements between the theory and the experiment: difference in exclusive and inclusive measurements of the CKM elements V_{ub} and V_{cb} [19], the P_5' anomaly in $B \to K^* \ell^+ \ell^-$ [11], lepton universality tests through measurements of R_D, R_D^*, R_K, and R_K^* [20–25], etc. In view of new measurements coming in with improved statistics, systematics, along with consistent improvements from the theoretical side, these are exciting times in B-physics.

2.3 The effective weak Hamiltonian

The effective theories provide a very convenient description of physics at a specific scale and have very diverse applications across physics. In particular physics, this formalism involves a particular scale in the relevant parameter space, e.g. energy, with the idea that the physical phenomena occurring at scales beyond the region turn irrelevant and perhaps, it is rather useful to work with a low-energy effective theory where the higher degrees of freedom no longer appear. With the expectation that this theory would be easier to handle than the full theory and yet will have the essence of the correct physics of the scale of interest.

Following this ideology in hadronic weak decays, the weak interactions can be well approximated by point like four-fermion couplings as the effects of the intermediate bosons can only be resolved at energies much larger than the hadron masses. In theory, we start off with integrating out the heavy-particle fields. With the heavy particles gone missing, we end up with a non-local effective action. The non-local effective action is then rewritten as a sum of local terms though operator product expansion (OPE). For weak decay of hadrons, the OPE formalism corresponds to an expansion in powers of $1/m_W$. After OPE, the long-distance and short-distance physics get disentangled. Long-distance physics is the same in the full and effective theory. However, the short-distance physics are not correctly described in this effective theory. These are added using renormalization-group techniques and amount to the renormalization of the coefficients of the local operators in the effective Lagrangian. A general effective Hamiltonian is given by

$$\mathcal{H}_{\text{eff}} = \frac{G_F}{\sqrt{2}} \sum_i \lambda_i^{\text{CKM}} C_i(\mu) \mathcal{O}_i(\mu)$$

where G_F is the Fermi constant, λ_i^{CKM} contains the corresponding Cabibbo-Kobayashi-Masakawa (CKM) factors. The $C_i(\mu)$ are Wilson coefficients and $\mathcal{O}_i$ are the local operators. The $B \to F$ decay amplitude would then be written as

$$A(B \to F) = \langle F|\mathcal{H}_{\text{eff}}|B\rangle = \frac{G_F}{\sqrt{2}} \sum_i \lambda_i^{\text{CKM}} C_i(\mu) \langle F|\mathcal{O}_i(\mu)|B\rangle,$$

where F is any final state. The OPE divides the $B \to F$ transition into two parts: short-distance and long-distance contributions separated by an energy scale μ referred to as the factorization scale. The Wilson coefficients contain all the short-distance information and can be calculated perturbatively. Naturally, the $C_i(\mu)$ includes contributions obtained by integrating heavy degrees of freedom such as top quarks, gauge bosons W and Z, and any new heavy NP contributions. All of the QCD effects above the factorization scale are contained in $C_i(\mu)$ and are independent of external states. Thus the Wilson coefficients do not depend on the hadrons involved; they only depend on the quarks involved in the process under consideration. On the other hand, the matrix elements $\langle F|\mathcal{O}_i(\mu)|B\rangle$ contains long-distance information i.e. contributions below the OPE factorization scale and hence need non-perturbative techniques. Some of the well established and popular non-perturbative techniques are LCSR, Lattice QCD, HQET, etc. The LCSR calculations are used for calculations in large recoil energy limit of the final state meson whereas the Lattice QCD and HQET are used in the low recoil limit.

The Wilson coefficients could also be determined from experimental data through global fits. For instance, the Wilson coefficients corresponding to the dominating operators in $b \to s$ transition (i.e. $C_{7,9,10}$) can be determined by performing global fits to the available data on $b \to s$ decays. In addition, numerical fits to data can be used to estimate or constrain the Wilson coefficients corresponding to various NP operators.

2.4 Prologue

Rare decays with $b \to s$ flavor-changing neutral currents(FCNCs) are sensitive to physics beyond the standard model. No wonder these modes have drawn plenty of attention from theoreticians and experimentalists alike. A large number of observables (i.e. branching fractions, angular coefficients, CP asymmetries, angular asymmetries, etc.) can be constructed for both inclusive, and exclusive B decay modes which can be measured at the B factories(Belle, BaBar), and the LHC experiments(LHCb). However, few disagreements with SM have been reported in these decay modes over the last few years. In 2013, LHCb had observed a tension in $B \to K^* \ell^+ \ell^-$ angular observables [26] which has persisted with the later updates in data [27]. In 2014, LHCb had observed that the ratio R_K of $B \to K \mu^+ \mu^-$ and $B \to K e^+ e^-$ branching fractions is suppressed compared to SM in the low q^2 region [24]. Similar tensions have also been observed for R_{K^*} in $B \to K^* \ell^+ \ell^-$ [25]. Tensions have also been observed for $R(D^{(*)})$ in the charged current decays $B \to D^{(*)} \ell^+ \ell^-$ by BaBar [20], Belle [21,22], and LHCb collaborations [23]. These observables have clean estimates from SM as the leading uncertainties coming from form-factors tend to cancel out in these ratios, adding huge significance to these observations. While the observed R_K or R_{K^*} lies below the SM expectations, observations for $R(D)$ or $R(D^*)$ lie above the SM predictions. The combined average, including correlations, for the charged-current decays puts the tension between the data and SM at the level of 3.9σ [19]. Another instance of such tensions is that the branching ratio measurements for $B \to K^* \mu^+ \mu^-$ [28] and $B_s \to \phi \mu^+ \mu^-$ [29] turn out to be too low compared to SM predictions [30–33].

As mentioned above the theoretical estimates for $R_{K^{(*)}}$, and $R(D^{(*)})$ are very clean, however, the estimates for other observables are affected by uncertainties which could come from poorly known form-factors, from contributions of the hadronic weak Hamiltonian that breaks quark-hadron duality, from breaking of QCD factorization, from resonance contributions, etc. Hence, it's important that we carefully consider these factors before making any significant claim about NP. There are several ways to go about this. One could try to estimate the uncertainties from the theory using clever and innovative techniques, or one can design observables that are less and less dependent on these uncertainties, or one can choose to investigate certain observables in certain kinematic regions such that the hadronic effects are minimal, etc [6, 8, 32, 34–45].

A huge amount of literature is available on $b \to s\gamma$ and $b \to s\ell^+\ell^-$ mediated rare decays. Among the phenomenological studies, the global analyses mostly vary in degree of sophistication, or by statistical approaches, or through means in which the theoretical uncertainties are estimated. A few of them are discussed in the following. In [13], the authors have tried to calculate the global significance of the relevant experimental data. A detailed discussion of possible theoretical uncertainties with correlations and their effects on the results is given. However, the analysis relies on form factor estimates and they have used integrated observables over the higher q^2 region to wash off the effects of broader charm resonances. Their earlier works [46, 47] also depend upon form factor estimates. In another work [48], the authors perform a global analysis of the then measured LHCb data with a set of optimal observables (i.e. $P_{1,2}$, $P'_{4,5,6,8}$, and $A_{\rm FB}$) over five q^2 bins along with branching ratio for some of the radiative and dileptonic B decays. It is found that the discrepancy patterns in the data is well explained by a solution with $C_7^{\rm NP}, C_9^{\rm NP} < 0$. The $C_7^{\rm NP} < 0$ is driven by the radiative decays. Though the analysis uses two low-recoil bins, emphasis is given to the first three bins in the high-recoil (or low q^2) region where the observables have low hadronic and high NP sensitivities. The analysis also does not include correlations among observables as they were not available at the time. The authors also point out that the case for the chiarally-flipped Wilson coefficient

C_9' is favored by the data in high-recoil region but upset by the data in low-recoil region. In [49] which uses a different statistical approach, a global analysis is done using Baysian inference and the theory uncertainties are modeled through use of nuisance parameters. It uses lattice calculations of form factors and other QCD calculations for theory estimates. NP scenario with additional chirally flipped operators $\mathcal{O}_{7',9',10'}$ is discussed. The study finds that the disagreements with the angular, and optimal observables can be diffused by allowing $10\% - 20\%$ shifts in the transversity amplitudes at low q^2 that can be attributed to subleading contributions. However, when chirally-flipped operators are present, shifts up to a few percent is adequate. The study finds if lattice-QCD form factors are used for high q^2 bins, the scenario with chirally-flipped operators can explain the data as efficiently or even better than the standard model. In another work [50], possible sources of theoretical uncertainties and their implications on the LHCb P_5' is discussed. An ansatz is proposed to parametrize the corrections to QCD factorisation beyond leading order of $\Lambda_{\rm QCD}/m_b$. The impact of power corrections at low-recoil is also discussed. They are suppressed by $(\Lambda_{\rm QCD}/m_b)^2$ or by $\alpha_s\Lambda_{\rm QCD}/m_b$ [36]. Form factor estimates from LCSR and LQCD calculations are used for obtaining the SM estimate. The authors also use a toy Monte-Carlo model to calculate correlation among observables which is used in the numerical analysis. Finally, the authors show that the discrepancies are consistent with the MFV(minimal flavor violation) hypothesis, and no new flavor structures are needed. In another work [44], the authors investigate the low recoil region in $\bar{B} \to \bar{K}^*(\to \bar{K}\pi)\ell^+\ell^-$ and $\bar{B} \to \bar{K}\ell^+\ell^-$ with a complete set of semi-leptonic dimension-six operators. Observables that are free from hadronic uncertainties under OPE(operator product expansion) in this limit are illustrated. The effects of power corrections or duality violation are assessed. The sensitivity of observables to SM and NP models are discussed.

However, as seen above most of the studies rely on the form factor estimates coming from LCSR or LQCD calculations. Even the optimal observables, that are less dependent on these form factors, are prone to power corrections as well as corrections coming from beyond the standard QCDF or OPE frameworks, even though they are only at few percent level in some instances. Hence, in order to obtain a robust NP signal, a completely model independent approach is required. Moreover, the global analyses indicate the presence of NP in C_9. Some of the studies also find good explanation in the presence of chiral-flipped operators.

Chapter 3

Right Handed currents in $B \to K^*\ell^+\ell^-$

The contents of this chapter are based on the work done with Rahul Sinha, Rusa Mandal, Anirban Karan and Thomas E. Browder in [3].

3.1 Introduction

The rare semileptonic decay $B \to K^*\ell^+\ell^-$ involves $b \to s$ flavor changing quark transition at the quark level. In the absence of FCNC in SM, these processes are loop induced with penguin and box diagrams giving dominant contributions. Hence, these modes serve as indirect yet sensitive probes for physics beyond the SM. With the subsequent decay of $K^* \to K\pi$, the angular analysis of the decay products enables us to measure a large number of observables [51] which can then be used to reduce hadronic uncertainties. Moreover, B mesons are produced in copious amounts at Belle, BABAR, and LHCb , with higher statistics expected from Belle and LHCb in coming years. In view of these, $B \to K^*\ell^+\ell^-$ is considered to be a relevant probe for new physics (NP). A considerable amount of work has been devoted to study these modes. However, most of these efforts have been put on the low dilepton invariant mass squared region $q^2 = 1-6$ GeV^2 [13]. Though the low q^2 region is immune to any significant resonance contributions, the theory involved in this region relies on the form factor estimates and hence are prone to hadronic uncertainties. Alternatively, efforts have also been put in studying the large q^2 region [44, 52] and some have been already successful in obtaining possible signals of NP in this limit [2]. In this chapter, we show that there is a unique way to probe for a particular class of NP at the very end of the kinetic spectrum. We discover that the latest LHCb measurements imply a 5σ evidence for the presence of NP in $B \to K^*\ell^+\ell^-$. While the evidence of RH currents is evident, other NP contributions are also feasible. Our conclusions are drawn around $q^2 \to q^2_{\rm max}$. Naturally, instead of depending on theoretical estimates for hadronic parameters, we have used heavy quark symmetries which are reliable in this limit [10, 52]. We have also used the limiting values of the observables that are kinetically constrained at $q^2_{\rm max}$ and does not change in the presence of NP. However, their approach to these values is affected by the nature of NP present in the decay channels.

In this chapter, we have presented a formalism that uniquely probes for RH currents in $B \to K^*\ell^+\ell^-$. The chapter is arranged as follows: The model-independent theoretical framework is presented in Sec. 3.2. The numerical procedures used for extracting RH currents and, the impact of resonance and systematic contributions on it are discussed in Sec. 3.3. Finally, we summarize in Sec. 3.4.

3.2 Theoretical Framework

3.2.1 The $B \to K^*\ell^+\ell^-$ rare decay

In SM, $B \to K^*\ell^+\ell^-$ decay is described in an effective theory, where, a effective Hamiltonian separates the short-distance and long-distance physics. However, exclusive decays such as this are always a theoretical challenge. Not only do we have to assess the hadronic form factors accurately, we also have to carefully accommodate effects such as the "non-factorizable" contributions which do not correspond to the conventional form factors. The nonfactorizable contributions originate from electromagnetic corrections to the hadronic operators in the effective Hamiltonian. Nonetheless, it is possible to write the decay amplitudes in the most general parametric form which accommodates both the factorizable and nonfactorizable contributions as shown in Ref. [1, 9].

The short-distance effective Hamiltonian, $\mathcal{H}_{\rm eff}$, for the underlying quark level $b \to s\ell^+\ell^-$ transition is given by

$$\mathcal{H}_{\rm eff} = -4\frac{G_F}{\sqrt{2}}\Big[V_{tb}V_{ts}^*\Big(C_1\mathcal{O}_1^c + C_2\mathcal{O}_2^c + \sum_{i=3}^{10} C_i\mathcal{O}_i\Big) + V_{ub}V_{us}^*\Big(C_1(\mathcal{O}_1^c - \mathcal{O}_1^u) + C_2(\mathcal{O}_2^c - \mathcal{O}_2^u)\Big)\Big], \tag{3.1}$$

where, G_F is the Fermi constant, V_{ij} are the CKM matrix elements corresponding to the respective quark currents. The local operators $\mathcal{O}_i$ are given in Ref. [7], out of which the dominant operators are given by

$$\begin{aligned}
\mathcal{O}_7 &= \frac{e}{g^2}\Big[\bar{s}\sigma_{\mu\nu}(m_b P_R + m_s P_L)b\Big]F^{\mu\nu},\\
\mathcal{O}_9 &= \frac{e^2}{g^2}(\bar{s}\gamma_\mu P_L b)\bar{\ell}\gamma^\mu\ell,\\
\mathcal{O}_{10} &= \frac{e^2}{g^2}(\bar{s}\gamma_\mu P_L b)\bar{\ell}\gamma^\mu\gamma_5\ell,
\end{aligned} \tag{3.2}$$

where, $e(g)$ is the electromagnetic(strong) coupling constant, $P_{L,R} = (1 \mp \gamma_5)/2$ are the chiral projection operators, and $m_b(m_s)$ are the running $b(s)$ quark mass in $\overline{\rm MS}$ scheme. The Wilson coefficients, C_i, contain the short-distance information and are evaluated perturbatively up to next-to-next-to-leading-logarithmic (NNLL) order [53, 54]. The NP contributes exclusively to these Wilson coefficients. The Wilson coefficients calculated for $b \to s\ell^+\ell^-$ process are same for every decay mode with the same underlying quark level transition. The decay amplitudes for different modes differ only in the long-distance contributions. The long-distance contributions are encoded in the hadronic matrix element of the local bilinear operators $\mathcal{O}_i$, i.e. $\langle f|\mathcal{O}_i|B\rangle$, that are calculated using non-perturbative techniques such as HQET. Most of the theoretical error in the decay amplitudes come from the absence of reliable calculations of these matrix elements.

The decay amplitude in terms of the hadronic matrix elements for $B \to K^*\ell^+\ell^-$is given by [6, 52]

$$A(B(p) \to K^*(k)\ell^+\ell^-) = \frac{G_F\alpha}{\sqrt{2}\pi}V_{tb}V_{ts}^*\Big[\Big\{\widehat{C}_9\langle K^*|\bar{s}\gamma^\mu P_L b|\bar{B}\rangle$$

$$- \frac{2\widehat{C}_7}{q^2}\langle K^*|\bar{s}i\sigma^{\mu\nu}q_\nu(m_bP_R+m_sP_L)b|\bar{B}\rangle - \frac{16\pi^2}{q^2}\sum_{i=\{1-6,8\}}\widehat{C}_i\mathcal{H}_i^\mu\Big\}\bar{\ell}\gamma_\mu\ell$$

$$+\widehat{C}_{10}\langle K^*|\bar{s}\gamma^\mu P_L b|\bar{B}\rangle\bar{\ell}\gamma_\mu\gamma_5\ell\Big], \tag{3.3}$$

where, $p = k + q$ with q being the dilepton invariant momentum. The $\widehat{C}_7$, $\widehat{C}_9$, and $\widehat{C}_{10}$ indicate the true values of the corresponding Wilson coefficients. The non-local hadronic matrix element, $\mathcal{H}_i^\mu$, is given by

$$\mathcal{H}_i^\mu = \langle K^*(k)|i\int d^4x e^{iq.x}T\{j^\mu_{\rm em}(x),\mathcal{O}_i(0)\}|\bar{B}(p)\rangle. \tag{3.4}$$

The form of the amplitude presented in Eq. (3.3) is notionally complete and free from any approximation. The hadronic matrix elements can be expressed in the most general form using Lorentz invariance [1]:

$$\langle K^*(\epsilon^*,k)|\bar{s}\gamma^\mu P_L b|B(p)\rangle = \epsilon^*_\nu\Big(\mathcal{X}_0q^\mu q^\nu + \mathcal{X}_1\Big(g^{\mu\nu}-\frac{q^\nu q^\nu}{q^2}\Big)$$

$$+\mathcal{X}_2\Big(k^\mu-\frac{k.q}{q^2}q^\mu\Big)q^\nu + i\mathcal{X}_3\epsilon^{\mu\nu\rho\sigma}k_\rho q_\sigma\Big), \tag{3.5}$$

$$\langle K^*(\epsilon^*,k)|i\bar{s}\sigma^{\mu\nu}q_\nu P_{R,L}b|B(p)\rangle = \epsilon^*_\nu\Big(\pm\mathcal{Y}_1\Big(g^{\mu\nu}-\frac{q^\nu q^\nu}{q^2}\Big)$$

$$\pm\mathcal{Y}_2\Big(k^\mu-\frac{k.q}{q^2}q^\mu\Big)q^\nu + i\mathcal{Y}_3\epsilon^{\mu\nu\rho\sigma}k_\rho q_\sigma\Big). \tag{3.6}$$

Where, $\mathcal{X}_{0,1,2,3}$, and $\mathcal{Y}_{1,2,3}$ are form factors that are functions of q^2, and k^2. The explicit momentum dependencies have been ignored for notational simplicity. For $B \to (K^* \to K\pi)\ell^+\ell^-$, the subsequent decay of $K^*(k) \to K(k_1)\pi(k_2)$ can be easily taken into account [7, 51]. The corresponding hadronic matrix elements are given by

$$\langle[K(k_1)\pi(k_2)]_{K^*}|\bar{s}\gamma^\mu P_L b|B(p)\rangle = D_{K^*}(k^2)W_\nu\Big(\mathcal{X}_0q^\mu q^\nu + \mathcal{X}_1\Big(g^{\mu\nu}-\frac{q^\nu q^\nu}{q^2}\Big)$$

$$+\mathcal{X}_2\Big(k^\mu-\frac{k.q}{q^2}q^\mu\Big)q^\nu + i\mathcal{X}_3\epsilon^{\mu\nu\rho\sigma}k_\rho q_\sigma\Big), \tag{3.7}$$

$$\langle[K(k_1)\pi(k_2)]_{K^*}|i\bar{s}\sigma^{\mu\nu}q_\nu P_{R,L}b|B(p)\rangle = D_{K^*}(k^2)W_\nu\Big(\pm\mathcal{Y}_1\Big(g^{\mu\nu}-\frac{q^\nu q^\nu}{q^2}\Big)$$

$$\pm\mathcal{Y}_2\Big(k^\mu-\frac{k.q}{q^2}q^\mu\Big)q^\nu + i\mathcal{Y}_3\epsilon^{\mu\nu\rho\sigma}k_\rho q_\sigma\Big). \tag{3.8}$$

The subscript K^* in $[K(k_1)\pi(k_2)]_{K^*}$ indicates that the final state has been produced by a decaying K^*. $D_{K^*}(k^2)$ is the K^* propagator:

$$|D_{K^*}(k^2)|^2 = \frac{g^2_{K^*K\pi}}{(k^2 - m^2_{K^*})^2 + (m_{K^*}\Gamma_{K^*})^2}, \tag{3.9}$$

where, $g_{K^*K\pi}$ is the $K^*K\pi$ coupling,

$$W_\nu = K_\nu - \xi k_\nu, \quad K = k_1 - k_2, \quad k = k_1 + k_2, \text{ and } \xi = \frac{k_1^2 - k_2^2}{k^2}. \tag{3.10}$$

The matrix elements arising from the nonlocal operators in Eq. (3.3) can also be expressed in a generic form using Lorentz invariance:

$$\begin{aligned} \mathcal{H}_i^\mu &= \langle K^*(\epsilon^*, k)| i \int d^4x e^{iq.x} T\{j^\mu_{em}(x), \mathcal{O}_i(0)\}|\bar{B}(p)\rangle \\ &= \epsilon^*_\nu \Big(\mathcal{Z}_1^i (g^{\mu\nu} - \frac{q^\nu q^\nu}{q^2}) + \mathcal{Z}_2^i (k^\mu - \frac{k.q}{q^2} q^\mu) q^\nu + i \mathcal{Z}_3^i \epsilon^{\mu\nu\rho\sigma} k_\rho q_\sigma \Big). \end{aligned} \tag{3.11}$$

As these matrix elements arise from non-local contributions, three new form factors $\mathcal{Z}^i_{1,2,3}$ have been introduced corresponding to nonfactorizable contributions from each $\mathcal{H}_i^\mu$.

From Eq. (3.3),(3.7),(3.8),(3.11) it's easy to see that the non-local contributions can be taken into account by redefining $\widehat{C}_9$ and modifying the contribution from the electromagnetic dipole operator $\mathcal{O}_7$ [1]. $\widehat{C}_7$ is the dominant contributor for $B \to K^*\gamma$ at $q^2 = 0$. However, the electromagnetic corrections to $\mathcal{O}_{1-6,8}$ also contribute to $B \to K^*\gamma$ at $q^2 = 0$. In addition, the charm loops at $q^2 = 0$ must contribute to $\widehat{C}_7$ in order for $\widehat{C}_7$ to be mode independent. The effect of this is to modify the $\widehat{C}_7 \langle K\pi|\bar{s} i\sigma^{\mu\nu} q_\nu (m_b P_R + m_S P_L) b|B\rangle$ terms such that the form factors and Wilson coefficients mix in an essentially inseparable fashion. This holds true even for the leading logarithmic contributions [5, 55]. Both factorizable and nonfactorizable contributions arising from electromagnetic corrections to hadronic operators up to all orders can in principle be included in this approach. The remaining contributions can easily be absorbed into a redefined effective $\widehat{C}_9$ defined such that

$$\widehat{C}_9 \to \widetilde{C}_9^{(j)} = \widehat{C}_9 + \Delta C_9^{\text{fac}}(q^2) + \Delta C_9^{(j),(\text{non-fac})}(q^2) \tag{3.12}$$

where, $j = 1,2,3$ and $\Delta C_9^{\text{fac}}(q^2)$, $\Delta C_9^{(j),(\text{non-fac})}(q^2)$ correspond to the factorizable and soft gluon nonfactorizable contributions, respectively and their dependencies on the form factors are as follows,

$$\Delta C_9^{\text{fac}} + \Delta C_9^{(j),\text{non-fac}} = -\frac{16\pi^2}{q^2} \sum_{i=\{1-6,8\}} \widehat{C}_i \frac{\mathcal{Z}_j^i}{\mathcal{X}_j}. \tag{3.13}$$

It should ne noted that there is no nonfactorizable correction term in Eq. (3.11) analogous to $\mathcal{X}_0$ due to EM current conservation.

The corresponding corrections to $\widehat{C}_7$ are taken into account by the replacement

$$\frac{2(m_b+m_s)}{q^2}\widehat{C}_7\mathcal{Y}_j \to \widetilde{\mathcal{Y}}_j = \frac{2(m_b+m_s)}{q^2}\widehat{C}_7\mathcal{Y}_j + \ldots, \tag{3.14}$$

where the dots indicate other factorizable and nonfactorizable contributions. The $\widetilde{\mathcal{Y}}_j$'s in Eq. (3.14) are complex in general due to nonfactorizable contributions to $\widehat{C}_7$. However, on-shell quarks and resonances do not contribute to them. The $\widetilde{C}_9^{(j)}$'s are also complex as they contain both factorizable and nonfactorizable effects as defined in Eq. (3.13). However, strong interaction effects originating from electromagnetic corrections to the hadronic operators do not contribute to $\widehat{C}_{10}$. In SM, $\widehat{C}_{10}$ is real whereas $\widetilde{C}_9^{(j)}$ and $\widetilde{\mathcal{Y}}_j$ are complex in general. The decay amplitude can therefore be written as

$$\begin{aligned}
A(B(p) \to [K(k_1)\pi(k_2)]_{K^*}\ell^+\ell^-) &= \frac{G_F\alpha}{\sqrt{2}\pi} V_{tb}V_{ts}^* D_{K^*}(k^2)\Bigg[\bigg\{C_L W.q\mathcal{X}_0 q^\mu \\
&+ C_L^{(1)}\mathcal{X}_1\left(K^\mu - \frac{W.q}{q^2}q^\mu - \xi k^\mu\right) + C_L^{(2)} W.q\mathcal{X}_2\left(k^\mu - \frac{k.q}{q^2}q^\mu\right) + iC_L^{(3)}\mathcal{X}_3\epsilon^{\mu\nu\rho\sigma}K_\nu k_\rho q_\sigma \\
&- \left(\zeta\widetilde{\mathcal{Y}}_1\left(K^\mu - \frac{W.q}{q^2}q^\mu - \xi k^\mu\right) + \zeta W.q\widetilde{\mathcal{Y}}_2\left(k^\mu - \frac{k.q}{q^2}q^\mu\right) + i\widetilde{\mathcal{Y}}_3\epsilon^{\mu\nu\rho\sigma}K_\nu k_\rho q_\sigma\right)\bigg\}\bar{\ell}\gamma_\mu P_L \ell \\
&+ L \to R\Bigg],
\end{aligned} \tag{3.15}$$

where, $C_{L,R} = \widehat{C}_9 \mp \widehat{C}_{10}$, $C_{L,R}^{(j)} = \widetilde{C}_9^{(j)} \mp \widehat{C}_{10}$, and $\zeta = (m_b - m_s)/(m_b + m_s)$. It's important to note that, no particular assumption has been made in obtaining Eq. (3.15) from Eq. (3.3). The introduced form factors are completely general and not altered by power corrections in HQET [56]. Consequently, Eq. (3.15) appears to be notionally exact.

3.2.2 The angular distribution

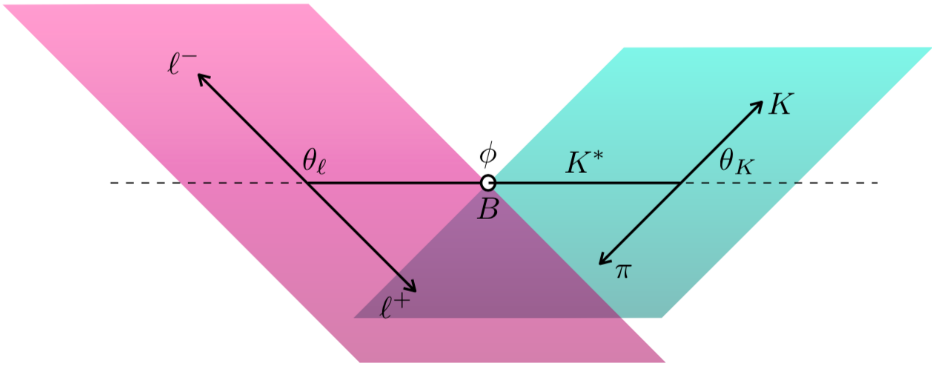

Figure 3.1: A depiction of the B rest frame and related kinematic variables.

The decay $\bar{B}(p) \to (K^*(k) \to K(k_1)\pi(k_2))\ell^+(q_1)\ell^-(q_2)$, can be completely described in terms of four independent kinematic variables: ϕ, θ_ℓ, θ_K, and the di-lepton invariant mass squared $q^2 = (q_1+q_2)^2$. The angles are defined in the B rest frame as shown in Fig. 3.1, where, the horizontal line towards the right is the +ve z-axis. The differential decay distribution of $B \to K^*\ell^+\ell^-$ is given by

$$\frac{d^4\Gamma(B\to K^*\ell^+\ell^-)}{dq^2 d\cos\theta_l d\cos\theta_K d\phi} = I(q^2,\theta_l,\theta_K,\phi) = \frac{9}{32\pi}\Big[I_1^s\sin^2\theta_K + I_1^c\cos^2\theta_K + (I_2^s\sin^2\theta_K + I_2^c\cos^2\theta_K)\cos 2\theta_\ell + I_3\sin^2\theta_K\sin^2\theta_\ell\cos 2\phi + I_4\sin 2\theta_K\sin 2\theta_\ell\cos\phi + I_5\sin 2\theta_K\sin\theta_\ell\cos\phi + I_6^s\sin^2\theta_K\cos\theta_\ell + I_7\sin 2\theta_K\sin\theta_\ell\sin\phi + I_8\sin 2\theta_K\sin 2\theta_\ell\sin\phi + I_9\sin^2\theta_K\sin^2\theta_\ell\sin 2\phi\Big]. \tag{3.16}$$

Here, the angular coefficients I's are measured from the study of the angular distribution and, are q^2 dependent. However, for notational simplification their explicit q^2 dependence has been suppressed.

In the massless lepton limit there are six real transversity amplitudes that correspond to six distinct configurations of the final state: three states of polarizations of K^* and left or right chirality of ℓ^-. The angular coefficients are expressed in terms of these six amplitudes: $\mathcal{A}^{L,R}_{\perp,||,0}$, where $\perp$, $||$, and 0 represent the polarizations of the on-shell K^* and L,R denote the chirality of the lepton current. The explicit expression of I's are given by

$$I_1^s = \frac{3}{4}\Big[|\mathcal{A}_\perp^L|^2 + |\mathcal{A}_{||}^L|^2 + (L \to R)\Big], \tag{3.17}$$

$$I_1^c = \Big[|\mathcal{A}_0^L|^2 + |\mathcal{A}_0^R|^2\Big], \tag{3.18}$$

$$I_2^s = \frac{1}{4}\Big[|\mathcal{A}_\perp^L|^2 + |\mathcal{A}_{||}^L|^2 + (L \to R)\Big], \tag{3.19}$$

$$I_2^c = -\Big[|\mathcal{A}_0^L|^2 + (L \to R)\Big], \tag{3.20}$$

$$I_3 = \frac{1}{2}\Big[|\mathcal{A}_\perp^L|^2 - |\mathcal{A}_{||}^L|^2 + (L \to R)\Big], \tag{3.21}$$

$$I_4 = \frac{1}{\sqrt{2}}\Big[\mathrm{Re}(\mathcal{A}_0^L \mathcal{A}_{||}^{L*}) + (L \to R)\Big], \tag{3.22}$$

$$I_5 = \sqrt{2}\Big[\mathrm{Re}(\mathcal{A}_0^L \mathcal{A}_\perp^{L*}) - (L \to R)\Big], \tag{3.23}$$

$$I_6^s = 2\Big[\mathrm{Re}(\mathcal{A}_{||}^L \mathcal{A}_\perp^{L*}) - (L \to R)\Big], \tag{3.24}$$

$$I_7 = \sqrt{2}\Big[\mathrm{Im}(\mathcal{A}_0^L \mathcal{A}_{||}^{L*}) - (L \to R)\Big], \tag{3.25}$$

$$I_8 = \frac{1}{\sqrt{2}}\Big[\mathrm{Im}(\mathcal{A}_0^L \mathcal{A}_\perp^{L*}) + (L \to R)\Big], \tag{3.26}$$

$$I_9 = \Big[\mathrm{Im}(\mathcal{A}_{||}^{L*} \mathcal{A}_\perp^{L}) + (L \to R)\Big]. \tag{3.27}$$

Again, the explicit q^2 dependence of the amplitudes have been ignored for notational simplicity.

The transversity amplitudes are expressed in terms of the form factors $\mathcal{X}_{0,1,2,3}$, and $\mathcal{Y}_{1,2,3}$ as follows:

$$\mathcal{A}_\perp^{L,R} = N\sqrt{2}\lambda^{1/2}(m_B^2, m_{K^*}^2, q^2)\,[(\widetilde{C}_9^{(3)} \mp \widehat{C}_{10})\mathcal{X}_3 - \widehat{\mathcal{Y}}_3], \tag{3.28}$$

$$\mathcal{A}_{||}^{L,R} = 2\sqrt{2}N\,[(\widetilde{C}_9^{(1)} \mp \widehat{C}_{10})\mathcal{X}_1 - \zeta\widehat{\mathcal{Y}}_1], \tag{3.29}$$

$$\begin{aligned}\mathcal{A}_0^{L,R} = \frac{N}{2m_{K^*}\sqrt{q^2}}\,[(\widetilde{C}_9^{(2)}\kappa \mp \widehat{C}_{10})\{4k.q\mathcal{X}_1 + \lambda(m_B^2, m_{K^*}^2, q^2)\mathcal{X}_2\} \\ - \zeta\{4k.q\widetilde{\mathcal{Y}}_1 + \lambda(m_B^2, m_{K^*}^2, q^2)\widetilde{\mathcal{Y}}_2], \end{aligned}\tag{3.30}$$

where,

$$\kappa = 1 + \frac{\widetilde{C}_9^{(1)} - \widetilde{C}_9^{(2)}}{\widetilde{C}_9^{(2)}}\frac{4k.q\mathcal{X}_1}{4k.q\mathcal{X}_1 + \lambda(m_B^2, m_{K^*}^2, q^2)\mathcal{X}_2}, \tag{3.31}$$

$\lambda(a,b,c) \equiv a^2+b^2+c^2-2(ab+bc+ac)$ and N is the normalization constant. In the narrow width approximation of K^*, $|D_{K^*}(k^2)|^2$ simplifies to

$$|D_{K^*}(k^2)|^2 = \frac{48\pi^2 m_{K^*}^4}{\lambda^{3/2}(m_{K^*}^2, m_K^2, m_\pi^2)}\delta(k^2-m_{K^*}^2). \tag{3.32}$$

This results in simplifying N to

$$N = V_{tb}V_{ts}^*\left[\frac{G_F^2\alpha^2}{3\times 2^{10}\pi^5 m_B^3}q^2\sqrt{\lambda(m_B^2, m_{K^*}^2, q^2)}\,\beta\right]^{1/2}. \tag{3.33}$$

The transversity amplitudes described in Eq. (3.28) can be rewritten in a short-form notation by introducing new form factors $\mathcal{F}_\lambda$ and $\widetilde{\mathcal{G}}_\lambda$ as follows:

$$\mathcal{A}_\lambda^{L,R} = C_{L,R}^\lambda\mathcal{F}_\lambda - \widetilde{\mathcal{G}}_\lambda = (\widetilde{C}_9^\lambda \mp C_{10})\mathcal{F}_\lambda - \widetilde{\mathcal{G}}_\lambda. \tag{3.34}$$

3.2.3 The SM amplitude:

As discussed in the previous section, in the massless lepton limit, the $B \to K^*\ell^+\ell^-$ decay process can be completely described through six transversity amplitudes which are expressed as [1]

$$\mathcal{A}_\lambda^{L,R} = C_{L,R}^\lambda\mathcal{F}_\lambda - \widetilde{\mathcal{G}}_\lambda = (\widetilde{C}_9^\lambda \mp C_{10})\mathcal{F}_\lambda - \widetilde{\mathcal{G}}_\lambda, \tag{3.35}$$

where λ runs over the polarizations of K^* i.e., perpendicular ($\perp$), parallel ($\|$), and longitudinal (0) and L,R denote the chirality of the lepton current. C_9 and C_{10} are the Wilson coefficients and $\widetilde{C}_9^\lambda$ is the redefined "effective" Wilson coefficient [1, 5, 6]:

$$\widetilde{C}_9^\lambda = C_9 + \Delta C_9^{(\text{fac})}(q^2) + \Delta C_9^{\lambda,(\text{non-fac})}(q^2). \tag{3.36}$$

$\Delta C_9^{(\text{fac})}$, $\Delta C_9^{\lambda,(\text{non-fac})}(q^2)$ indicate the factorizable and the soft gluon non-factorizable contributions, respectively. C_{10} is unaltered by strong interaction effects coming from the electromagnetic correction to hadronic operators [7]. $\mathcal{F}_\lambda$ and $\widetilde{\mathcal{G}}_\lambda$ are form factors that can be related to the conventional form factors when power corrections are neglected [1] and our analysis does not rely on estimates of these form factors. The amplitudes in Eq. (3.35) have been written in the massless lepton limit of the SM [4]. This parametric form is general enough to incorporate all short-distance, long-distance, factorizable, non-factorizable, resonance as well as electromagnetic corrections of hadronic operators up to all orders.

The transversity amplitudes, the Wilson coefficients, and the form factors are complex in general. However, in the SM, C_{10} and $\mathcal{F}_\lambda$ are real which means that the complex contributions to the amplitudes come from $\widetilde{C}_9^\lambda$ and $\widetilde{\mathcal{G}}_\lambda$. We can write the amplitudes such that the complex contributions are clearly visible:

$$\mathcal{A}_\lambda^{L,R} = (\mp C_{10} - r_\lambda)\mathcal{F}_\lambda + i\varepsilon_\lambda, \tag{3.37}$$

where r_λ and ε_λ are two real parameters i.e.,

$$r_\lambda = \frac{\mathrm{Re}(\widetilde{\mathcal{G}}_\lambda)}{\mathcal{F}_\lambda} - \mathrm{Re}(\widetilde{C}_9^\lambda), \tag{3.38}$$

$$\varepsilon_\lambda = \mathrm{Im}(\widetilde{C}_9^\lambda)\mathcal{F}_\lambda - \mathrm{Im}(\widetilde{\mathcal{G}}_\lambda). \tag{3.39}$$

The ε_λ contributions are ignorable in the SM. However, estimating their effects are essential for making any conclusive claims of physics beyond the SM; we elaborate on this later in the chapter.

The subsequent on-shell decay of $K^* \to K\pi$ means the full 4-body angular analysis of the final states in $B \to K^*\ell^+\ell^-$ lead to several observables. While there is a plethora of angular observables to choose from, we only define those carrying relevance for this chapter:

$$F_\lambda = \frac{|\mathcal{A}_\lambda^L|^2 + |\mathcal{A}_\lambda^R|^2}{\Gamma_f} \quad \lambda \in \{\perp, \|, 0\}, \quad \Gamma_f \equiv \sum_\lambda (|\mathcal{A}_\lambda^L|^2 + |\mathcal{A}_\lambda^R|^2) \tag{3.40}$$

$$A_{\mathrm{FB}} = \frac{3}{2}\frac{\mathrm{Re}(\mathcal{A}_\|^L \mathcal{A}_\perp^{L^*} - \mathcal{A}_\|^R \mathcal{A}_\perp^{R^*})}{\Gamma_f}, \tag{3.41}$$

$$A_5 = \frac{3}{2\sqrt{2}}\frac{\mathrm{Re}(\mathcal{A}_0^L \mathcal{A}_\perp^{L^*} - \mathcal{A}_0^R \mathcal{A}_\perp^{R^*})}{\Gamma_f}. \tag{3.42}$$

The relation between experimentally measured observables, LHCb [11] in particular, and the ones defined in Eq. (3.40-3.42) are given by

$$
\begin{aligned}
F_\perp &= \frac{1-F_L+2S_3}{2}, \quad A_4 = -\frac{2}{\pi}S_4, \\
A_5 &= \frac{3}{4}S_5, \quad A_{\rm FB} = -A_{\rm FB}^{\rm LHCb}.
\end{aligned} \tag{3.43}
$$

Where S_3, S_4, S_5, and $A_{\rm FB}^{\rm LHCb}$ are some of the angular observables reported by LHCb .

3.2.4 Introducing Right-Handed currents:

If we imagine a beyond the SM scenario where only RH currents have been added as an extension to the SM theory then the transversity amplitudes would be given by [7]

$$\mathcal{A}_\perp^{L,R} = ((\widetilde{C}_9^\perp + C_9') \mp (C_{10}+C_{10}'))\mathcal{F}_\perp - \widetilde{\mathcal{G}}_\perp \tag{3.44}$$

$$\mathcal{A}_\parallel^{L,R} = ((\widetilde{C}_9^\parallel - C_9') \mp (C_{10}-C_{10}'))\mathcal{F}_\parallel - \widetilde{\mathcal{G}}_\parallel \tag{3.45}$$

$$\mathcal{A}_0^{L,R} = ((\widetilde{C}_9^0 - C_9') \mp (C_{10}-C_{10}'))\mathcal{F}_0 - \widetilde{\mathcal{G}}_0. \tag{3.46}$$

At this point, we emphasize that ε_λ has been ignored from now onwards unless they are mentioned explicitly. For notational simplicity, we have introduced two parameters ξ, and ξ':

$$\xi = \frac{C_{10}'}{C_{10}} \text{ and } \xi' = \frac{C_9'}{C_{10}}. \tag{3.47}$$

The observables $F_\perp$, $F_\parallel$, F_L, $A_{\rm FB}$ and A_5 (Eqs. (3.40) – (3.42)) can be expressed by

$$F_\perp = 2\zeta(1+\xi)^2(1+R_\perp^2), \tag{3.48}$$

$$F_\parallel \mathsf{P}_1^2 = 2\zeta(1-\xi)^2(1+R_\parallel^2), \tag{3.49}$$

$$F_L \mathsf{P}_2^2 = 2\zeta(1-\xi)^2(1+R_0^2), \tag{3.50}$$

$$A_{\rm FB}\mathsf{P}_1 = 3\zeta(1-\xi^2)(R_\parallel + R_\perp), \tag{3.51}$$

$$\sqrt{2}A_5\mathsf{P}_2 = 3\zeta(1-\xi^2)(R_0+R_\perp), \tag{3.52}$$

where
$$\mathsf{P}_1 = \frac{\mathcal{F}_\perp}{\mathcal{F}_\parallel}, \quad \mathsf{P}_2 = \frac{\mathcal{F}_\perp}{\mathcal{F}_0}, \quad \zeta = \frac{\mathcal{F}_\perp^2 C_{10}^2}{\Gamma_f} \tag{3.53}$$
$$R_\perp = \frac{\frac{r_\perp}{C_{10}} - \xi'}{1+\xi}, \quad R_\parallel = \frac{\frac{r_\parallel}{C_{10}} + \xi'}{1-\xi}, \quad R_0 = \frac{\frac{r_0}{C_{10}} + \xi'}{1-\xi}. \tag{3.54}$$

Note that R_0, $R_\parallel$, $R_\perp$, P_2, and P_1 are dependent on form factors by definition. The objective in hand is to determine these hadronic quantities entirely from the observables. However, the helicity fractions or F_λs are not all independent as they are constrained by

$$F_L + F_\parallel + F_\perp = 1. \tag{3.55}$$

This implies that we have four independent equations instead of five. Hence, we can solve for four of our desired quantities in terms of the observables and one remaining unknown parameter (P_1 in this case) using Eq. (3.48)-(3.52):

$$R_\perp = \pm\frac{3}{2}\frac{\left(\frac{1-\xi}{1+\xi}\right)F_\perp + \frac{1}{2}\mathsf{P}_1 Z_1}{\mathsf{P}_1 A_{\rm FB}}, \tag{3.56}$$
$$R_\parallel = \pm\frac{3}{2}\frac{\left(\frac{1+\xi}{1-\xi}\right)\mathsf{P}_1 F_\parallel + \frac{1}{2}Z_1}{A_{\rm FB}}, \tag{3.57}$$
$$R_0 = \pm\frac{3}{2\sqrt{2}}\frac{\left(\frac{1+\xi}{1-\xi}\right)\mathsf{P}_2 F_L + \frac{1}{2}Z_2}{A_5}, \tag{3.58}$$
$$\mathsf{P}_2 = \frac{\left(\frac{1-\xi}{1+\xi}\right)2\mathsf{P}_1 A_{\rm FB} F_\perp}{\sqrt{2}A_5\left(\left(\frac{1-\xi}{1+\xi}\right)2F_\perp + Z_1\mathsf{P}_1\right) - Z_2\mathsf{P}_1 A_{\rm FB}}, \tag{3.59}$$

where
$$Z_1 = (4F_\parallel F_\perp - \frac{16}{9}A_{\rm FB}^2)^{\frac{1}{2}} \quad \text{and} \quad Z_2 = (4F_L F_\perp - \frac{32}{9}A_5^2)^{\frac{1}{2}}. \tag{3.60}$$

Our next task is to try and eliminate P_1 and as we will see, a relation among the form factors in the kinematic endpoint limit provides such an opportunity.

3.2.5 The kinematic endpoint

We choose the B rest frame to work with. In this frame, the kinematic endpoint limit is defined by $q^2 = q^2_{\rm max} = (m_B - m_{K^*})^2$. At this limit, the K^* is at rest and the leptons travel back to back; as a result, there is no preferred direction left in the decay kinematics. Some of the kinematic angles become irrelevant and can be integrated out, which in turn puts constraints on the amplitudes and consequently on the observables. Since the full decay can be described on a single plane, the perpendicular helicity must vanish which implies that $F_\perp = 0$. The K^* decaying at rest means that the $K\pi$ distribution is isotropic and independent of θ_K which implies $F_\parallel = 2F_L$ [10]. Since all of the transversity amplitudes vanish at $q^2 = q^2_{\rm max}$, $\Gamma_f(q^2_{\rm max}) = 0$. Overall, the nature of the decay kinematics at $q^2 = q^2_{\rm max}$ result in very unique values for the observables [1, 10]:

$$\begin{aligned}
&F_L(q^2_{\rm max}) = \frac{1}{3}, \quad F_\parallel(q^2_{\rm max}) = \frac{2}{3}, \quad A_4(q^2_{\rm max}) = \frac{2}{3\pi}, \\
&F_\perp(q^2_{\rm max}) = 0, \quad A_{\rm FB}(q^2_{\rm max}) = 0, \quad A_{5,7,8,9}(q^2_{\rm max}) = 0.
\end{aligned} \tag{3.61}$$

3.2.6 The low-recoil limit

The values taken by the observables at $q^2_{\rm max}$ are originated from kinematic constraints. The presence of NP in the decays does not affect these fixed values. In particular, the presence of RH currents does not affect these values; however, they could in principle alter the way these observables approach these values. We are interested in studying this behavior of observables around this region of the kinematic spectrum. The low-recoil limit or $q^2 \to q^2_{\rm max}$ is a region where K^* has low-recoil energy. The $B \to K^*\ell^+\ell^-$ mode has been studied in this limit with a modified heavy effective theory framework [8, 52]. We note that in $q^2 \to q^2_{\rm max}$ limit, the hadronic form factors satisfy the relation

$$\frac{\widetilde{\mathcal{G}}_\parallel}{\mathcal{F}_\parallel} = \frac{\widetilde{\mathcal{G}}_\perp}{\mathcal{F}_\perp} = \frac{\widetilde{\mathcal{G}}_0}{\mathcal{F}_0} = -\kappa\frac{2m_b m_B C_7}{q^2}, \tag{3.62}$$

where $\kappa \approx 1$ [8]. This relation has particular relevance for our analysis and is easily motivated. Moreover, it has been shown in Ref. [10] that the non-factorizable are also helicity independent in this limit. As a result, Eq. (3.36),(3.38) and (3.62) imply [9]

$$r_0 = r_\parallel = r_\perp \equiv r. \tag{3.63}$$

An immediate consequence of Eq. (3.63) comes from Eq. (3.54). It is easy to see that in the presence of RH currents, R_λ must obey

$$R_0(q^2_{\rm max}) = R_{||}(q^2_{\rm max}) \neq R_\perp(q^2_{\rm max}). \tag{3.64}$$

As mentioned already, this relation is unaltered by non-factorizable contributions. Moreover, the resonance contributions are helicity independent and hence do not affect Eq. (3.64). Hence, this relation is theoretically clean and could serve as a clean probe for the presence of RH currents in $B \to K^* \ell^+ \ell^-$.

3.2.7 The polynomial expansion

As mentioned in the previous subsection, we are interested in looking at how our observables and form-factor ratios (R_λ, P_1, P_2, ζ) approach the kinematic endpoint. We note that in the limit $q^2 \to q^2_{\rm max}$, $F_\perp(q^2_{\rm max}) = 0$ which implies

$$\zeta = 0. \tag{3.65}$$

Similarly, Eq. (3.49),(3.50),(3.54) and (3.64) together imply that

$$\mathsf{P}_2 = \sqrt{2}\,\mathsf{P}_1 \;\; \text{in the limit } q^2 \to q^2_{\rm max}. \tag{3.66}$$

On the other hand, Eq. (3.65),(3.49) and (3.50) imply that

$$\mathsf{P}_{1,2} \to 0 \;\; \text{in the limit } q^2 \to q^2_{\rm max}. \tag{3.67}$$

Hence, the functional dependency of $\mathsf{P}_{1,2}$ in terms of q^2 is crucial around $q^2_{\rm max}$. We Taylor expand all our observables around the kinematic endpoint in terms of the variable $\delta \equiv q^2_{\rm max} - q^2$. The relative momentum dependence of the $\mathcal{A}^{L,R}_\lambda$ are taken in to account by the leading order terms in δ of the Taylor expansions. It is clear from Eq. (3.40)-(3.42) and (3.61) that $\mathcal{A}^{L,R}_\perp$ must have at least a $\mathcal{O}(\sqrt{\delta})$ higher dependency compared to $\mathcal{A}^{L,R}_{||,0}$. This form of dependencies can also be seen in Ref. [10]. Given the $\mathcal{O}(\delta)$ behavior of $\mathcal{A}^{L,R}_\lambda$, it is easy to infer the $\mathcal{O}(\delta)$ dependencies of the observables: the leading term in F_L and $F_\parallel$ would be $\mathcal{O}(\delta^0)$, the leading term for $F_\perp$ would be $\mathcal{O}(\delta)$, whereas the leading terms for the asymmetries, A_5 and $A_{\rm FB}$, would be $\mathcal{O}(\sqrt{\delta})$. As a result, the observables are expressed as

$$F_L = \frac{1}{3} + F_L^{(1)}\delta + F_L^{(2)}\delta^2 + F_L^{(3)}\delta^3 \tag{3.68}$$

$$F_\perp = F_\perp^{(1)}\delta + F_\perp^{(2)}\delta^2 + F_\perp^{(3)}\delta^3 \tag{3.69}$$

$$A_{\rm FB} = A_{\rm FB}^{(1)}\delta^{1/2} + A_{\rm FB}^{(2)}\delta^{3/2} + A_{\rm FB}^{(3)}\delta^{5/2} \tag{3.70}$$

$$A_5 = A_5^{(1)}\delta^{1/2} + A_5^{(2)}\delta^{3/2} + A_5^{(3)}\delta^{5/2}, \tag{3.71}$$

where $X^{(n)}$ is the coefficient of the $n^{\rm th}$ term in the expansion of observable X. The above parametric form is purely motivated by the observable behavior at the kinematic endpoint and hence independent of any non-perturbative frameworks (HQET, for instance). Moreover, the validity of it away from the endpoint is based on the analytic continuation of the observables, hence it is insufficient to account for resonance effects. We will discuss how to deal with resonance systematics of the parametric fit later in the chapter.

3.2.8 The final input

The form factor relation of Eq. (3.62) is expected to hold in the large q^2 limit. The relation is clearly satisfied if it is valid at each order in the Taylor expansion:

$$q^2\frac{\widetilde{\mathcal{G}}_\lambda}{\mathcal{F}_\lambda} = q^2_{\rm max}\frac{\widetilde{\mathcal{G}}_\lambda^{(1)} + \delta\,(\widetilde{\mathcal{G}}_\lambda^{(2)} - \dfrac{\widetilde{\mathcal{G}}_\lambda^{(1)}}{q^2_{\rm max}}) + \mathcal{O}(\delta^2)}{\mathcal{F}_\lambda^{(1)} + \delta\,\mathcal{F}_\lambda^{(2)} + \mathcal{O}(\delta^2)}. \tag{3.72}$$

However, we only need that the relation is valid up to order δ. As seen in Eq. (3.72), this can be achieved if $\mathcal{F}_\lambda^{(2)} = c\,\mathcal{F}_\lambda^{(1)}$ and $(q^2_{\rm max}\,\widetilde{\mathcal{G}}_\lambda^{(2)} - \widetilde{\mathcal{G}}_\lambda^{(1)}) = c\,q^2_{\rm max}\,\widetilde{\mathcal{G}}_\lambda^{(1)}$ where c is any constant. On the other hand, $\mathsf{P}_2 = \sqrt{2}\mathsf{P}_1$ at $q^2_{\rm max}$ which means the leading order coefficients of $\mathsf{P}_{1,2}$ must obey the relation $\mathsf{P}_2^{(1)} = \sqrt{2}\mathsf{P}_1^{(1)}$. However, as $\mathcal{F}_\lambda^{(2)} = c\,\mathcal{F}_\lambda^{(1)}$, the second order coefficients also should obey

$$\mathsf{P}_2^{(2)} = \sqrt{2}\mathsf{P}_1^{(2)}. \tag{3.73}$$

This is the required input for us to be able to solve R_λ completely in terms of the observable coefficients in the limit $q^2 \to q^2_{\rm max}$:

$$
\begin{aligned}
R_\perp(q^2_{\rm max}) &= \frac{8A^{(1)}_{\rm FB}(-2A^{(2)}_5 + A^{(2)}_{\rm FB}) + 9(3F^{(1)}_L + F^{(1)}_\perp)F^{(1)}_\perp}{8\,(2A^{(2)}_5 - A^{(2)}_{\rm FB})\,\sqrt{\frac{3}{2}F^{(1)}_\perp - A^{(1)\,2}_{\rm FB}}} \\
&= \frac{\omega_2 - \omega_1}{\omega_2\,\sqrt{\omega_1 - 1}}, \qquad (3.74)\\
R_\parallel(q^2_{\rm max}) &= \frac{3(3F^{(1)}_L + F^{(1)}_\perp)\,\sqrt{\frac{3}{2}F^{(1)}_\perp - A^{(1)\,2}_{\rm FB}}}{-8A^{(2)}_5 + 4A^{(1)}_{\rm FB} + 3A^{(1)}_{\rm FB}(3F^{(1)}_L + F^{(1)}_\perp)} \\
&= \frac{\sqrt{\omega_1 - 1}}{\omega_2 - 1} = R_0(q^2_{\rm max}) \qquad (3.75)
\end{aligned}
$$

$$
\text{where,}\quad \omega_1 = \frac{3}{2}\frac{F^{(1)}_\perp}{A^{(1)\,2}_{\rm FB}} \quad \text{and} \quad \omega_2 = \frac{4\,(2A^{(2)}_5 - A^{(2)}_{\rm FB})}{3\,A^{(1)}_{\rm FB}(3F^{(1)}_L + F^{(1)}_\perp)}. \qquad (3.76)
$$

As the above equation suggests, $R_\lambda(q^2_{\rm max})$ are only dependent on $F^{(1)}_L$, $F^{(1)}_\perp$, $A^{(2)}_{\rm FB}$, and $A^{(2)}_5$; where, the coefficients are obtained through a polynomial fit to the experimental data.

If RH currents or any other NP that affect the perpendicular helicity differently around $q^2_{\rm max}$ are not present then we must have $R_\perp(q^2_{\rm max}) = R_\parallel(q^2_{\rm max}) = R_0(q^2_{\rm max})$. Then it's clear from Eq. (3.51) that $R_\lambda(q^2_{\rm max}) > 0$ as $A_{\rm FB}\mathsf{P}_1 > 0$ and $\zeta > 0$ in this limit. On the other hand, even if RH currents are present their contributions are expected to be small as otherwise they would have been seen elsewhere. In such scenarios, ξ and ξ' are restricted to reasonably small values and $R_\lambda(q^2_{\rm max}) > 0$ still holds true. This is made explicit in Eq. (3.74)-(3.75), where only the positive solutions are kept as compared to Eq. (3.56)-(3.58).

3.3 Numerical Analysis

The numerical analysis based on the theoretical framework developed in Section 3.2 is presented here.

	$O^{(1)}(10^{-2})$	$O^{(2)}(10^{-3})$	$O^{(3)}(10^{-4})$
F_L	-2.85 ± 1.26	12.13 ± 1.90	-5.68 ± 0.67
$F_\perp$	6.89 ± 1.65	-9.79 ± 2.47	3.83 ± 0.86
$A_{\rm FB}$	-30.58 ± 1.95	26.96 ± 3.58	-4.15 ± 1.47
A_5	-15.85 ± 1.87	5.38 ± 3.33	2.46 ± 1.29

Table 3.1: The best fit values along with their $\pm1\sigma$ errors for coefficients of the observables in Eqs. ((3.68))-((3.71)) are shown. These values are obtained by fitting the bin-averaged values of the observables to the LHCb 's 14-bin measurements [11].

3.3.1 Polynomial fits

As made apparent in Eq. (3.64), the presence of RH currents can be inferred by measuring the R_λ at $q^2_{\rm max}$. To that effect, we have deduced a way to compute R_λ using experimentally measurements at this limit, see Eq. (3.74),(3.75) and (3.68)-(3.71). In order to achieve this, we have to extract the expansion coefficients of the observables or $X^{(n)}$ from experimental data. The data we use are based on the latest LHCb measurements [11] of F_L, $F_\perp$, $A_{\rm FB}$ and A_5. The corresponding correlations among the observables, as reported by LHCb , are also taken into account. These measurements provide observables evaluated in particular bins of q^2 and the corresponding values in theory are easily calculable from Eq. (3.68)-(3.71) in terms of $X^{(n)}$. We fit these theoretical bin averaged entities to their bin averaged values measured in experiments through a χ^2 minimization. We have used the 14-bin data set based on the method of moments [57] as compared to the 8-bin data set as the earlier one provides more data sets close to the kinematic endpoint and hence helps to constraint the parameters better.

First, we fit a polynomial (in terms of δ) to the differential decay rate or $d\Gamma/dq^2$ data [12] for the entire q^2 region. We use this fit for $d\Gamma/dq^2$ (say $\Gamma(q^2)$) in weighted average of all observables. The theoretical bin averaged observables are then obtained by integrating their polynomial or parametric forms weighted with that of the differential decay rate. For instance, the bin averaged value of an observable $\mathcal{O}$ in q^2 bin $[b_i, b_f]$ would be given by

$$\frac{\int_{b_i}^{b_f}\mathcal{O}(q^2)\Gamma(q^2)\,dq^2}{\int_{b_i}^{b_f}\Gamma(q^2)\,dq^2}. \tag{3.77}$$

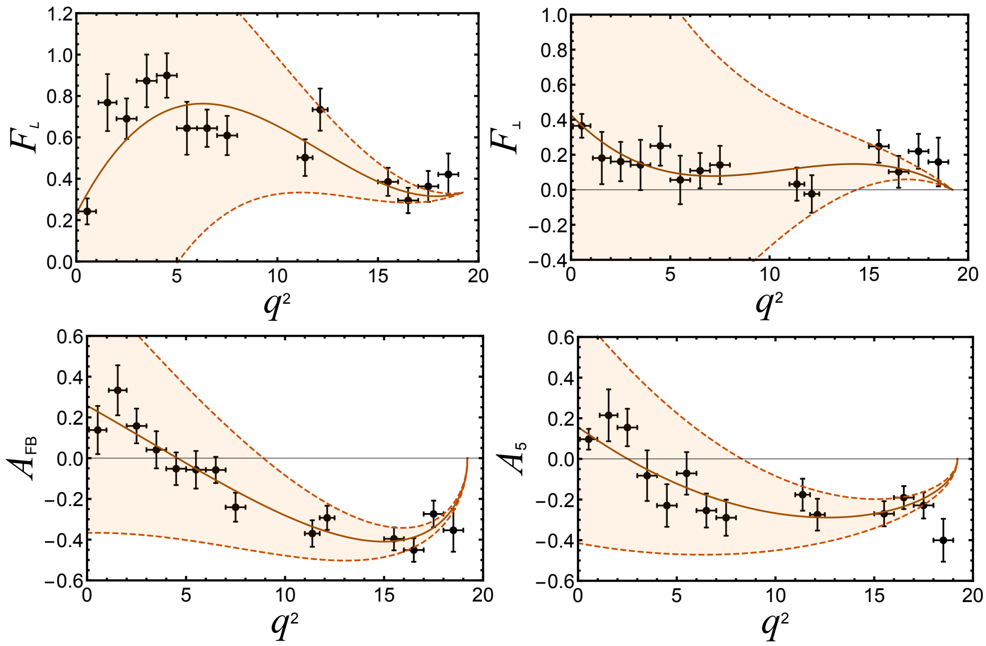

Figure 3.2: The polynomial fits for F_L, $F_\perp$, $A_{\rm FB}$ and A_5 are shown. The q^2 is in units of GeV^2. The solid brown curve at the center correspond to the third-order polynomial seen in Eq. (3.68)-(3.71). The dashed brown lines along with the light brown shaded region illustrate the $\pm 1\sigma$ error bands of the central polynomial fit. The black cross marks depict the LHCb measurements [11] and their errors.

The best fit values obtained for each of the observable coefficients or $X^{(n)}$ are shown in Table 3.1. We have used a covariance matrix technique to estimate the errors on each of the coefficients. Note that the factorization assumption $A_{\rm FB}^{(1)} = 2A_5^{(1)}$ still holds true within $\pm 1\sigma$. However, we treat $A_{\rm FB}^{(1)}$ and $2A_5^{(1)}$ as two independent measurements of any given quantity. The resulting polynomial fits for F_L, $F_\perp$, $A_{\rm FB}$ and A_5 are shown in Fig. 3.2, from left to right respectively. The solid brown curve at the center correspond to the third order polynomial seen in Eq. (3.68)-(3.71). The dashed brown lines along with the light brown shaded region illustrate the $\pm 1\sigma$ error bands of the central polynomial fit. The black cross marks depict the LHCb measurements [11] with the center indicating the central value in the specific bin, the horizontal line indicating the span of the q^2 bin and the vertical line indicating the $\pm 1\sigma$ errors on the measurements.

3.3.2 Hint of Right-Handed Currents

Given the knowledge of the observable coefficients, $\omega_{1,2}$ are easily calculated using

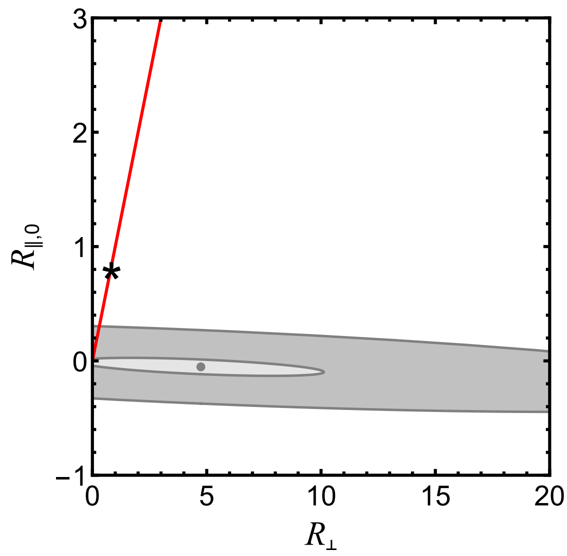

Figure 3.3: The estimated contours of R_λ in $R_\perp - R_{\|,0}$ plane are shown. The predicted 1σ and 5σ confidence levels are shown in light and dark gray contours, respectively. The gray point at the center of 1σ contour indicates the best fit value. The black star corresponds to the SM estimate. The solid red straight line represents the $R_\perp = R_{\|,0}$.

Eq. (3.76):

$$\omega_1 = 1.10 \pm 0.30 \; (1.03 \pm 0.34),$$
$$\omega_2 = -4.19 \pm 10.48 \; (-4.04 \pm 10.12), \tag{3.78}$$

where the values in round brackets are evaluated in terms of $A_5^{(1)}$, using $A_{\rm FB}^{(1)} = 2A_5^{(1)}$ in Eq. (3.76). Considering the large errors in extraction of $\omega_{1,2}$, R_λ are obtained numerically using Eq. (3.74)-(3.75) and we consider two different approaches in doing so. In one approach, the $F_L^{(1)}$, $F_P^{(1)}$, $A_{\rm FB}^{(1)}$, $A_5^{(1)}$, $A_{\rm FB}^{(2)}$, and $A_5^{(2)}$ are taken as Gaussian distributions around the central values as mean and errors from Tabel. 3.1. For each set of randomly chosen values from these distributions, we generate R_λ. The R_λ, thus simulated, must lie on a $45^{\rm o}$ inclined straight line in $R_\perp - R_{\|,0}$ plane if RH currents are absent. However, we observe the slope of $R_{\|,0}$ vs $R_\perp$ to be nearly horizontal, implying $R_\perp \gg R_{\|,0}$. This can be perceived as evidence for presence of RH currents in $B \to K^*\ell^+\ell^-$.

In another approach, we fit R_λ as functions of $\omega_{1,2}$ to their estimated values and errors in Eq. (3.78) by minimizing the corresponding χ^2 function. The results are depicted in Fig. 3.3. The predicted 1σ and 5σ confidence levels are shown in light and dark gray

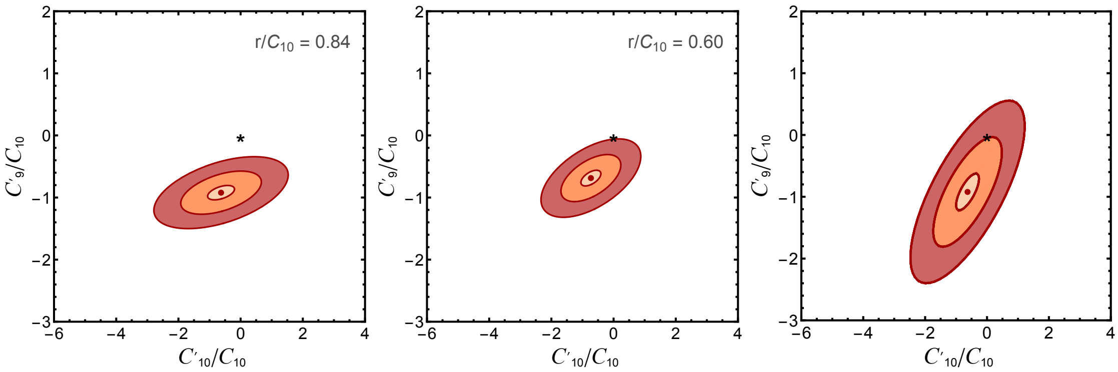

Figure 3.4: The predicted regions in ξ - ξ' plane are shown. The yellow, orange and red contours correspond to 1σ, 3σ and 5σ confidence levels, respectively. The red dot at center indicates the best fit value. The black star correspond to the SM estimate of C'_{10}/C_{10} and C'_9/C_{10}. These plots illustrate the sensitivity of ξ, and ξ' to r/C_{10}. The figure in the first panel corresponds to ξ - ξ' contours generated using the SM estimate of $r/C_{10} = 0.84$ [8] and the SM value of ξ, and ξ' lied beyond 5σ confidence level. The estimates in the second panel correspond to $r/C_{10} = 0.60$ which coincides with an additional NP contribution $C_9^{\rm NP} \approx -1$ [13]. The estimates on the last panel result from treating r/C_{10} as a nuisance parameter where the SM value is lying on the edge of 3σ confidence level.

contours, respectively. The gray point at the center of 1σ contour indicates the best fit value. The black star corresponds to the SM estimate. The solid red straight line represents the $R_\perp = R_{\|,0}$. The deviation of the contours from the SM estimates is a signal of the presence of RH currents.

3.3.3 ξ and ξ' estimates

As the presence of RH currents established, we move to get an estimate of corresponding Wilson coefficients (WC), i.e. C'_9 and C'_{10}. We use Eqs. (3.54), (3.74) and (3.75) to perform a χ^2 fit to our NP parameters ξ and ξ'. The SM estimate for $r/C_{10}(q^2_{\rm max})$ is required as an input here which can be easily obtained from Eq. (3.62). The predicted regions in ξ - ξ' plane are shown in Fig. 3.4. The yellow, orange and red contours correspond to 1σ, 3σ and 5σ confidence levels, respectively. The red dot at center indicates the best fit value. The black star correspond to the SM estimate of C'_{10}/C_{10} and C'_9/C_{10}. The first figure corresponds to the SM estimate of $r/C_{10} = 0.84$ [8]. The best fit values with $\pm 1\sigma$ error of ξ and ξ' are -0.63 ± 0.43 and -0.92 ± 0.10, respectively. The SM estimate lies beyond 5σ confidence level in this case which is as per expectation with Fig. 3.3.

The r/C_{10} estimates are sensitive to errors in Wilson coefficients, other kinds of NP contributions, resonance contributions, etc. In order to make our claims more robust, we have to consider these effects. We scan r/C_{10} over a range of values and find that the evidence for RH currents is clear. However, the discrepancy can be somewhat reduced if r/C_{10} is smaller. This scenario is depicted in the second (middle) figure in Fig. 3.4 where the SM estimate lies on the edge of 5σ confidence level. The corresponding value of r/C_{10} is 0.6, which results from $C_9^{\rm NP} \approx -1$ as suggested by a global fit analysis for $b \to s$ transition [13]. The best fit values ξ and ξ' with $\pm 1\sigma$ errors are obtained to be -0.73 ± 0.32 and -0.69 ± 0.10, in this case.

The third or last figure in Fig. 3.4 depicts a scenario where r/C_{10} has been considered as a nuisance parameter. The best fit values with $\pm 1\sigma$ error of ξ, ξ' and r/C_{10} are given by -0.63 ± 0.43, -0.92 ± 0.14 and 0.84 ± 0.10, respectively. The errors in the NP Wilson coefficients have increased due to variation in r/C_{10}. However, the SM estimate still lies on the edge on 3σ confidence level establishing the presence of RH currents.

3.3.4 Resonance effects

In this section, we assess the effect of resonance states on the parametric fits to the observables presented in Eq. (3.68)-(3.71). The dominant resonance contributions in $B \to K^* \ell^+ \ell^-$ come from the charm resonances. In the absence of an exact theory, it is impossible to separate the real signal from resonance effects as is done for other background modes. Not surprisingly, bins containing narrow width resonances such as J/ψ and $\psi(2S)$ are usually ignored in the extraction of observable data. However, the interference of these resonances with the signal mode can have a significant impact on the observables even beyond the aforementioned bins. Moreover, the effect of broad resonances in the higher q^2 region is always present in the bin-averaged observables. Considering these, it is safe to assume that the resonance contributions are implicitly present in the bin-averaged values of the observables. Two obvious questions emerge: How significant are they?, and How do they affect our conclusions?

In our approach, we have used polynomial functions to fit the observable data but we could have equally chosen any other function. However, a poor choice of functions will lead to a poor fit with large errors. Our fits reflect the errors resulted from ignoring resonance contributions. It should be noted that even if a better function or a better estimate of resonance systematics were to be implemented, the fits itself would not be invalidated rather the errors estimated in Table. 3.1 would decrease. In other words, our errors are an overestimate. We also emphasize that the real part of resonance contributions are notionally included in the amplitudes and the imaginary parts are also accounted for as discussed in Sec. 3.3.6. Since, both our theory and experimental data include resonance contributions, the observed discrepancy cannot arise due to resonances. Below we discuss the differences between q^2 distributions with and without resonances as systematic uncertainties.

In the following numerical analysis, the observable values are evaluated from the SM estimated form factors and Wilson coefficients. For $q^2 \leq 15\,\text{GeV}^2$ the form factors are evaluated using LCSR [32] while for $q^2 \geq 15\,\text{GeV}^2$ Lattice QCD [33] is used. The resonances are introduced as prescribed in [58] where the corresponding one-loop functions in C_9^{eff} are defined by

$$
\begin{aligned}
g(m_c, q^2) = &-\frac{8}{9}\ln\frac{m_c}{m_b} - \frac{4}{9} \\
&+ \frac{q^2}{3}\mathcal{P}\int_{4\hat{m}_D^2}^{\infty} \frac{R_{\text{had}}^{c\bar{c}}(x)}{x(x-q^2)}dx + i\frac{\pi}{3}R_{\text{had}}^{c\bar{c}}(q^2),
\end{aligned}
\tag{3.79}
$$

where $\mathcal{P}$ denotes the principal value. m_c and m_b are masses of c and b quark, respectively. Also, $\hat{m}_D = m_D/m_b$ where m_D is the mass of $D-$meson. The hadronic cross section ratio $R_{\text{had}}^{c\bar{c}}(q^2)$ is defined by

$$
R_{\text{had}}^{c\bar{c}}(q^2) \equiv \frac{\sigma_{\text{tot}}(e^+e^- \to \text{hadrons})}{\sigma_{\text{tot}}(e^+e^- \to \mu^+\mu^-)}
\tag{3.80}
$$

which can be written as

$$
R_{\text{had}}^{c\bar{c}}(q^2) = R_{\text{cont}}^{c\bar{c}}(q^2) + R_{\text{res}}^{c\bar{c}}(q^2),
\tag{3.81}
$$

where $R_{\text{cont}}^{c\bar{c}}$ and $R_{\text{res}}^{c\bar{c}}$ indicate contributions from the continuum and the narrow resonances, respectively. The narrow widths are well approximated by a Breit-Wigner ansatz:

$$R^{c\bar{c}}_{\rm res}(q^2) = N_r \sum_{V=J/\psi,\psi',..} \frac{9\,q^2}{\alpha} \frac{{\rm Br}(V\to\ell^+\ell^-)\Gamma^V_{\rm tot}\Gamma^V_{\rm had}}{(q^2-m_V^2)^2+m_V^2\Gamma^{V2}_{\rm tot}} e^{i\delta_V} \tag{3.82}$$

where N_r is a normalization factor which determines the size of resonance contributions. m_V, $\Gamma^V_{\rm tot}$, and $\Gamma^V_{\rm had}$ are the mass, the total width and the hadronic width of vector meson "V". δ_V is a strong phase associated with each of the vector mesons. In this analysis, we have taken the $J/\psi\,(1S)$, $\psi(2S)$, $\psi(3770)$, $\psi(4040)$, $\psi(4160)$ and $\psi(4415)$ resonances into account. We have used the values for the masses and widths of these mesons as provided in [59]. The continuum part, $R^{c\bar{c}}_{\rm cont}(q^2)$ can be determined using experimental data. We have considered two different parametrization of $R^{c\bar{c}}_{\rm cont}(q^2)$, as given in Refs. [58] and [45]. We observe that both of these parametrization give virtually indistinguishable results for this analysis. Before moving on to the next step, we introduce another overall normalization factor N_b such that $d\Gamma/dq^2$ is consistent with its experimentally observed value. As seen from Eq. (3.79)-(3.82), $C_9^{\rm eff}$ and in turn the transversity amplitudes depend on N_b, N_r and δ_V. In other words, given δ_V all the observables depend only on N_b and N_r. However, δ_V are not known quantities hence we simulate their values in particular intervals for their entire range.

Using the framework described above, we numerically calculate the branching fractions for eight q^2 bins given in Ref. [12]. Summing them all up we end up with a quantity which is denoted by $d\Gamma^{\rm tot}_{\rm th}/dq^2$. Similarly, we also calculate the branching fractions for the q^2 region $[3.05^2, 3.15^2]$ to match with the cuts implemented by Belle in measuring the $B^0 \to J/\psi K^{*0}$ branching fraction [61] and denote it by $d\Gamma^{J/\psi}_{\rm th}/dq^2$. Given δ_V, the $d\Gamma^{\rm tot}_{\rm th}/dq^2$ and $d\Gamma^{J/\psi}_{\rm th}/dq^2$ are completely dependent on the normalization factors which means by comparing them with their experimentally measured values we can obtain N_b and N_r. In other words, N_b and N_r can be obtained by solving the following quadratic equations:

$$\begin{aligned} \frac{d\Gamma^{\rm tot}_{\rm th}(N_b,N_r)}{dq^2} &= 4.379\times10^{-7} \\ \frac{d\Gamma^{J/\psi}_{\rm th}(N_b,N_r)}{dq^2} &= 1.29\times10^{-3}. \end{aligned} \tag{3.83}$$

The above equation also implies that for each set of choices of δ_V, we obtain two sets of values of N_b and N_r. The strong phases are varied through $\pi/12$ intervals starting from 0 to 2π. Keeping a limited amount of data, we present only some sample plots which are obtained by varying δ_V for $J/\psi\,(1S)$, $\psi(4040)$, and $\psi(4160)$ resonances. More than 22000 of such plots have been put together in the form of movies that are available on [62]. Two particular examples corresponding to $\delta_{J/\psi\,(1S)} = 0$, $\delta_{\psi(4040)} = 0$, $\delta_{\psi(4160)} = 0$, and $\delta_{J/\psi\,(1S)} = 3\pi/2$, $\delta_{\psi(4040)} = 4\pi/3$, $\delta_{\psi(4160)} = 5\pi/2$ are presented in Fig. 3.5. Where, the red curves correspond to SM predicted behavior of the corresponding observables in the absence of resonance contributions. The observables have been evaluated using LCSR form factors for $4m_\ell^2 < q^2 < 15\,\text{GeV}^2$ and Lattice-QCD form factors for $15\,\text{GeV}^2 < q^2 < q^2_{\text{max}}$. The solid gray curves result after the inclusion of resonance contributions. The light gray bands lie around the threshold of narrow resonances $J/\psi\,(1S)$, $\psi(2S)$, and $\psi(3770)$. The resonance effects are expected to be significant in this region and hence ignored in the experimental data.

From Fig. 3.5 and [62], we observe that the inclusion of resonances does not have any noticeable effect on the helicity fractions. Only the asymmetries A_{FB}, and A_5 show significant change. Furthermore, we note that the asymmetries show a drop in their magnitudes for $15\,\text{GeV}^2 \leq q^2 \leq 19\,\text{GeV}^2$ region. In other words, the magnitudes of A_{FB}, and A_5 will increase in this q^2 region if it were possible to somehow subtract the resonance contributions from the data. Similarly, the slope or the angle of approach of the corresponding polynomial fits ($A^{(1)}_{\text{FB}}$, $A^{(1)}_5$), as they approach zero at q^2_{max}, will also increase if the resonances could be subtracted. Following Eq. (3.76) it is clear that the ω_1 will decrease if resonance effects could be taken out or in other words, the ω_1 will increase in its value in $15\,\text{GeV}^2 \leq q^2 \leq 19\,\text{GeV}^2$ region if resonance effects are included. Note that ω_1 central values from our fits (see Eq. 3.78) are already close to unity. Since $\omega_1 < 1$ is unphysical, we infer that the data can not have significant resonance contributions.

We can also see analytically that significant resonance contributions would in fact strengthen our claims. For that we consider the observable Z_1 [1,9] which can be cast as

$$Z_1 = \sqrt{4F_\parallel F_\perp - \frac{16}{9}A^2_{\text{FB}}}$$

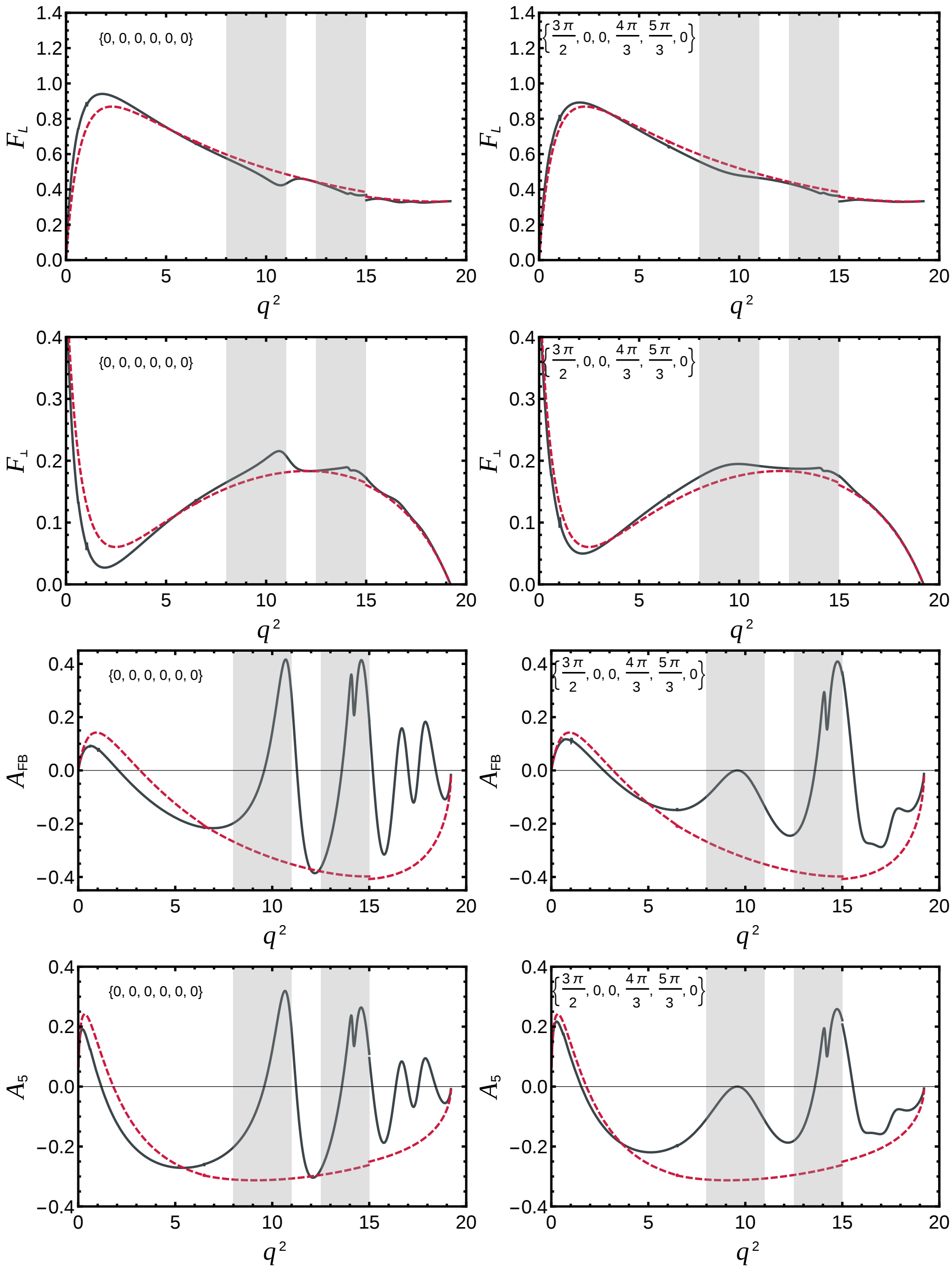

Figure 3.5: The observables F_L, $F_\perp$, $A_{\rm FB}$, and A_5 after the inclusion of charm resonances are shown here. The q^2 is in units of GeV^2. The red dashed curves correspond to the SM estimate of the corresponding observables evaluated using LCSR and Lattice-QCD form factors. The gray curves correspond to the observables with resonances added. The figures on the left column have all the strong phases set to zero, while the ones on the right correspond to the choice of $\delta_{J/\psi\,(1S)} = 3\pi/2$, $\delta_{\psi(4040)} = 4\pi/3$, and $\delta_{\psi(4160)} = 5\pi/2$. The light gray shaded regions correspond to $8.0\,\mathrm{GeV}^2 < q^2 < 11.0\,\mathrm{GeV}^2$, and $12.5\,\mathrm{GeV}^2 < q^2 < 15.0\,\mathrm{GeV}^2$. Since these regions are dominated by resonance contributions, they are excluded from the experimental data [11].

$$= \frac{4}{3}|A_{\rm FB}|\sqrt{\frac{9F_{\|}F_{\perp}}{4A_{\rm FB}^2}-1} = \frac{4}{3}|A_{\rm FB}|\sqrt{\Omega_1 - 1} \tag{3.84}$$

$$\text{where} \quad \Omega_1 = \frac{9F_{\|}F_{\perp}}{4A_{\rm FB}^2}. \tag{3.85}$$

The observable is real implying $\Omega_1 > 1$. Experimental measurements of $F_{\|}$, $F_{\perp}$ and $A_{\rm FB}$ for $q^2 > 15\,{\rm GeV}^2$ indicate that Ω_1 is close to unity. If resonance contributions are explicitly included Z_1 becomes,

$$\begin{aligned} Z_1 &= \frac{4}{3}|A_{\rm FB}|\sqrt{\frac{9(F_{\|}-\frac{2\varepsilon_{\|}^2}{\Gamma_f})(F_{\perp}-\frac{2\varepsilon_{\perp}^2}{\Gamma_f})}{4A_{\rm FB}^2}-1} \\ &= \frac{4}{3}|A_{\rm FB}|\sqrt{\Omega_1 - \mathcal{O}\Big(\frac{2\varepsilon_{\|,\perp}^2\Omega_1}{F_{\|,\perp}\Gamma_f}\Big)-1} \end{aligned} \tag{3.86}$$

where ε_λ is defined in Eq. (3.39) and $\mathcal{O}\Big(\frac{2\varepsilon_{\|,\perp}^2\Omega_1}{F_{\|,\perp}\Gamma_f}\Big) > 0$.

Hence, we conclude that the resonance contributions cannot be significant in data or else the value of Ω_1 would become unphysical. It should be noted that $\omega_1 \equiv \Omega_1(q^2_{\rm max})$, implying that the value of ω_1 which we find very close to unity is consistent and would only decrease and become unphysical if resonances were included. The same arguments hold for the observables Z_2 and Ω_2 or ω_2. It may be noted that in a previous study of resonance effects in $B \to K\ell^+\ell^-$ [45], the difficulty in accommodating the LHCb-result in the standard treatment of the SM or QCD was noted and possible right-handed current contributions were suggested.

3.3.5 Convergence of polynomial fit

In Sec. 3.2 the observables F_L, $F_\perp$, $A_{\rm FB}$, and A_5 were Taylor expanded in terms of third order polynomials around $q^2_{\rm max}$, see Eqs. (3.68)– (3.71). The values of the fit coefficients were given in Table. 3.1. In this section we study the systematic effects on the fit coefficients $F_L^{(1)}$, $F_P^{(1)}$, $A_{\rm FB}^{(1)}$, $A_{\rm FB}^{(2)}$, $A_5^{(1)}$, and $A_5^{(2)}$ as they determine $\omega_{1,2}$ defined in Eq. (3.76). We have varied order of the polynomials from two to four. We have also varied the number of

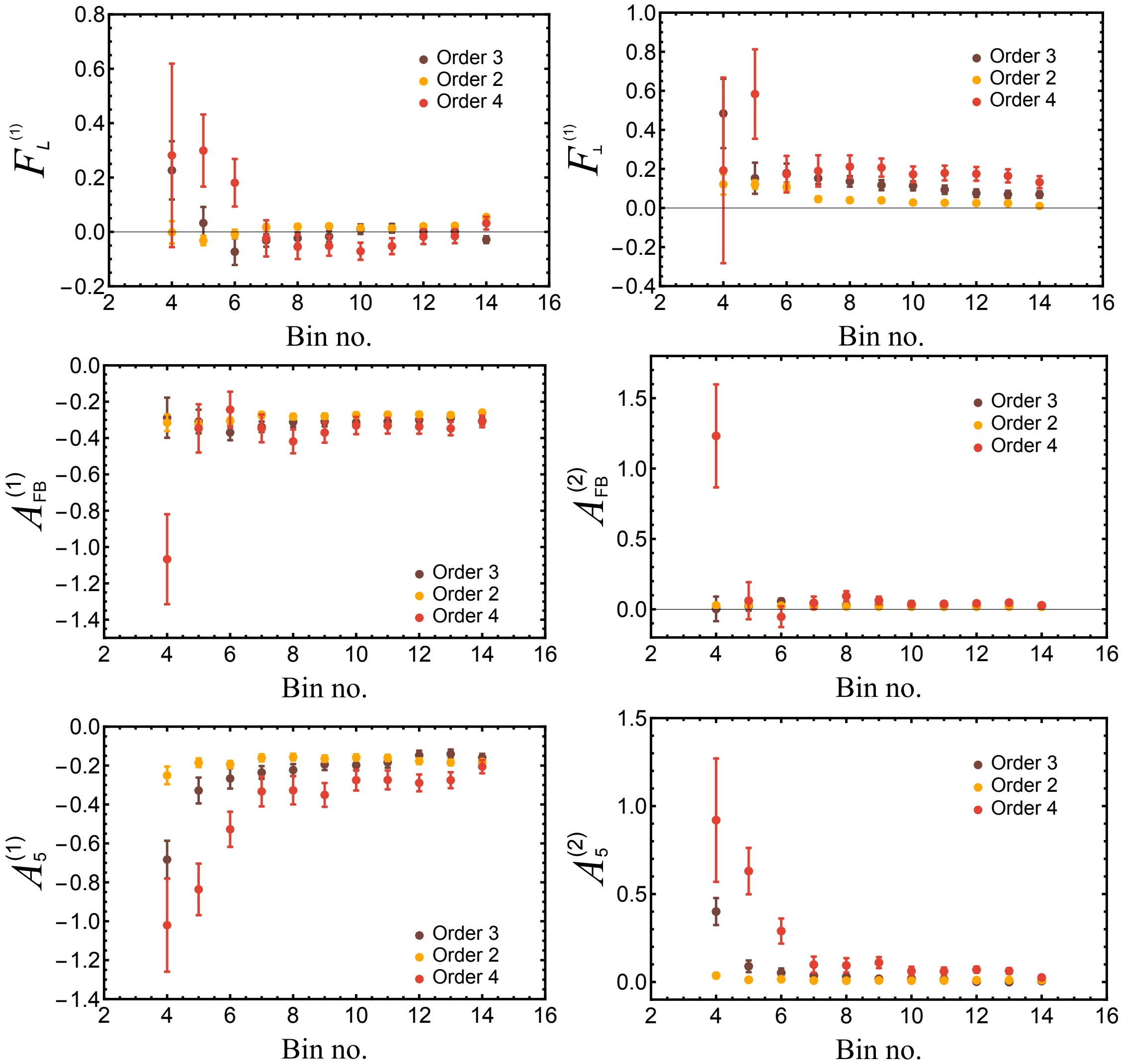

Figure 3.6: A summary of the fit coefficient values and their $\pm 1\sigma$ errors are shown here. The coefficients are obtained by varying the order of the polynomials as well as the number of bin averaged values considered in the data set. The color code for different orders of the polynomial are shown in each panel. The $x-$axis denotes the number of bin averaged values used in the fit. The $y-$ axis denotes the value taken by these coefficients. The best fit values of the coefficients are given by circular dots while the vertical bars through them denote $\pm 1\sigma$ errors. The thin gray line indicates the value zero.

experimental bin averaged values, used in the fit, from last four to fourteen. The resulting fits with $\pm 1\sigma$ error bands for F_L, $F_\perp$, $A_{\rm FB}$, and A_5 are depicted in Fig. 3.9, Fig. 3.10, Fig. 3.11, and Fig. 3.12, respectively. The color codes and other details are as that of Fig. 3.2. The corresponding fit coefficients $F_L^{(1)}$, $F_P^{(1)}$, $A_{\rm FB}^{(1)}$, $A_{\rm FB}^{(2)}$, $A_5^{(1)}$, and $A_5^{(2)}$ and their errors are illustrated in Fig. 3.6. The color codes for varying order of the polynomials are given in each panel of Fig. 3.6. The $x-$axis denotes the number of bin averaged values

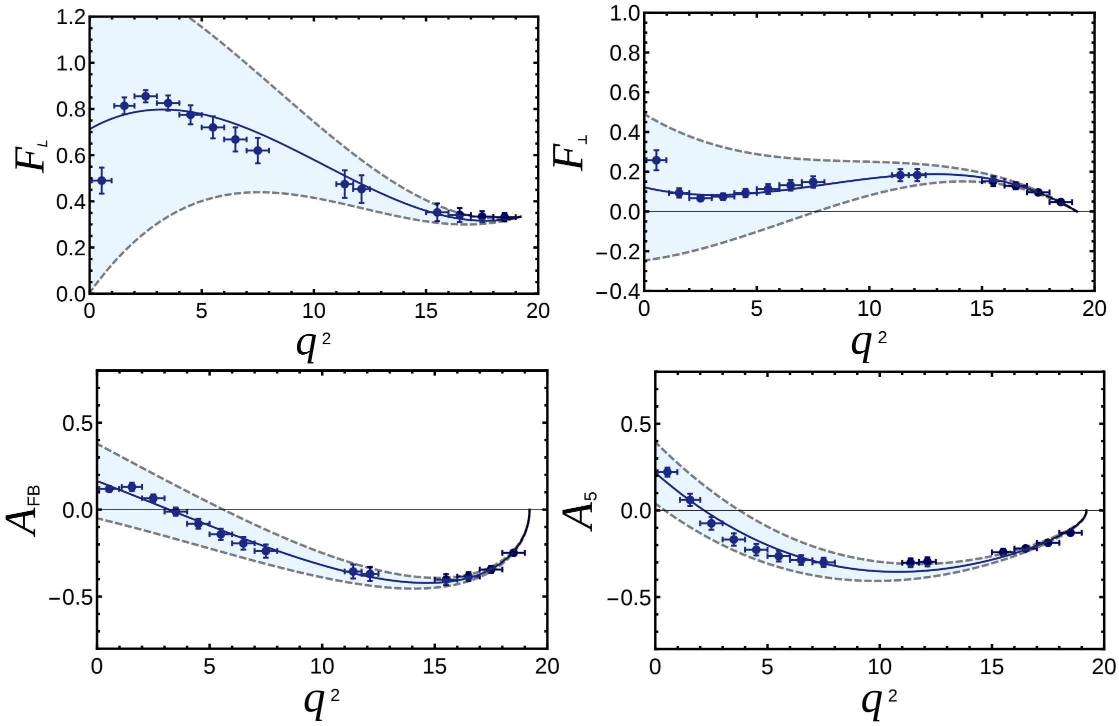

Figure 3.7: The third order polynomial fits to 14-bin SM simulated data are shown here. The q^2 is in units of GeV^2. The blue central curve is the best fit while the dashed blue curves along with the light blue shaded region illustrate $\pm 1\sigma$ region surrounding the best fit. The blue crosses depict the corresponding observable data points which are generated using LCSR form factors for $q^2 \leq 15\,\mathrm{GeV}^2$ and Lattice QCD form factors for $q^2 \geq 15\,\mathrm{GeV}^2$.

used in the fit. The $y-$ axis denotes the value taken by these coefficients. The best fit values of the coefficients are given by circular dots while the vertical bars through them denote $\pm 1\sigma$ errors. The thin gray line indicates the value zero. We observe from Fig. 3.6 that the fit coefficients show a good degree of convergence in terms of the order of the polynomials when more number of bin averaged values are used in the fit, particularly when seven or higher number of bins are used. A small mismatch is observed in $F_P^{(1)}$, and $A_5^{(1)}$ even with large number of bins. As evident, the third order polynomials with all of the fourteen bins are used as the best suited fit.

To illustrate the sanctity of our choice, we use the same third order polynomials to fit the observables to 14-bin SM data. The SM data for the observables are obtained using form factor values from LCSR [32] for the $q^2 \leq 15\,\mathrm{GeV}^2$ and from Lattice QCD [33] for $q^2 \geq 15\,\mathrm{GeV}^2$ region. The results are shown in Fig. 3.7. The central blue line correspond to the best fit polynomial while the dashed blue curves along with the light blue shaded region denote $\pm 1\sigma$ errors on them. It is clear that the fits are satisfactory in the entire q^2 region while being impeccably accurate for $q^2 \geq 15\,\mathrm{GeV}^2$.

3.3.6 Imaginary contributions to amplitude, ε_λ

The complex contributions to the transversity amplitudes or ε_λ (see Eq. (3.37)) are usually expected to be sub-dominant and were neglected in Sec. 3.2. Nonetheless, ε_λ are not necessarily small and their effects have to be assessed in order to validate our claims.

The amplitude definitions in Eq. (3.37) leads to $2|\varepsilon_\lambda|^2/\Gamma_f$ contributing to F_λ [1]. We define this quantity as $\widehat{\varepsilon}_\lambda \equiv 2|\varepsilon_\lambda|^2/\Gamma_f$. We can Taylor expand $\widehat{\varepsilon}_\lambda$ in terms of δ around q^2_{max}:

$$\widehat{\varepsilon}_\perp = \widehat{\varepsilon}_\perp^{(1)}\delta + \widehat{\varepsilon}_\perp^{(2)}\delta^2 + \widehat{\varepsilon}_\perp^{(3)}\delta^3, \tag{3.87}$$

$$\widehat{\varepsilon}_0 = \widehat{\varepsilon}_0^{(0)} + \widehat{\varepsilon}_0^{(1)}\delta + \widehat{\varepsilon}_0^{(2)}\delta^2, \tag{3.88}$$

$$\widehat{\varepsilon}_\parallel = \widehat{\varepsilon}_\parallel^{(0)} + \widehat{\varepsilon}_\parallel^{(1)}\delta + \widehat{\varepsilon}_\parallel^{(2)}\delta^2. \tag{3.89}$$

The limiting values (as $\delta \to 0$) of F_λ in Eq. (3.61) implies

$$\widehat{\varepsilon}_\parallel^{(0)} = 2\,\widehat{\varepsilon}_0^{(0)}. \tag{3.90}$$

As seen in Ref. [1], the helicity fractions gets modified by $\widehat{\varepsilon}_\lambda$:

$$\begin{aligned} F_\lambda &= F_\lambda^0 + \widehat{\varepsilon}_\lambda \\ \text{where}\quad F_\lambda^0 &= F_\lambda\big|_{\varepsilon_\lambda\to 0}\,. \end{aligned} \tag{3.91}$$

A_{FB} and A_5 are unaltered by ε_λ. On the other hand, asymmetries such as A_7, A_8, and A_9 are linearly proportional to ε_λ [1]. Following Eq. (3.91) and the fact that A_{FB}, and A_5 are unaltered, the $\omega_{1,2}$ defined in Eq. (3.76) get modified as

$$\omega_1 = \frac{9}{4}\frac{\left(\frac{2}{3} - 2\,\widehat{\varepsilon}_0^{(0)}\right)\left(F_\perp^{(1)} - \widehat{\varepsilon}_\perp^{(1)}\right)}{A_{\mathrm{FB}}^{(1)\,2}}, \tag{3.92}$$

$$\omega_2 = \frac{4\left(2A_5^{(2)} - A_{\mathrm{FB}}^{(2)}\right)\left(1 - 3\,\widehat{\varepsilon}_0^{(0)}\right)}{3\,A_{\mathrm{FB}}^{(1)}\left(3F_L^{(1)} + F_\perp^{(1)} + \widehat{\varepsilon}_\parallel^{(1)} - 2\,\widehat{\varepsilon}_0^{(1)}\right)}. \tag{3.93}$$

As the above equation suggests we need to obtain the coefficients $\widehat{\varepsilon}_0^{(0)}$, $\widehat{\varepsilon}_0^{(1)}$, $\widehat{\varepsilon}_\parallel^{(1)}$, and $\widehat{\varepsilon}_\perp^{(1)}$ in order to estimate $\omega_{1,2}$. We have used the 3 fb^{-1} of LHCb data [11] to simulate these coefficients which are then used in estimating

$$\begin{aligned}\omega_1 &= 1.03 \pm 0.31\ (0.98 \pm 0.29),\\ \omega_2 &= -4.52 \pm 17.40\ (-3.94 \pm 9.86).\end{aligned} \tag{3.94}$$

The first values are obtained using $A_{\rm FB}^{(1)}$, and $A_9^{(1)}$ while the ones in round brackets are obtained using $2A_5^{(1)}$ and $-\frac{2}{3}A_8^{(1)}$. We only require that the factorization assumption holds true in leading order of the observable expansions i.e., $A_{\rm FB}^{(1)} = 2A_5^{(1)}$ and $A_9^{(1)} = -\frac{2}{3}A_8^{(1)}$. Comparing with Eq. (3.78) we observe that the inclusion of complex contributions has insignificant effect on $\omega_{1,2}$. Hence, we infer that our claims are not affected by the complex contributions present in the amplitudes.

3.3.7 Effect of finite K^* width

The K^* has a finite width of 47.3 ± 0.5 MeV [65]. This implies that the position of the kinematic endpoint $q^2_{\rm max}$ could vary within a small range which would in turn affect the polynomial fits. We have studied the modification in coefficients of the polynomial fits by varying $q^2_{\rm max}$ in the range $18.34 - 20.10\,\text{GeV}^2$ in Eq. (3.68)–(3.71). The $\omega_{1,2}$ can be evaluated for any choice of $q^2_{\rm max}$ in this range e.g. we present 5 instances in Table 3.2 for which $\omega_{1,2}$ have been evaluated. With the corresponding polynomial fits shown in Fig. 3.8:

$q^2_{\rm max}$(in GeV^2)	ω_1	ω_2
18.34	$0.84 \pm 0.24(0.77 \pm 0.25)$	$25.16 \pm 433.67(24.01 \pm 413.86)$
18.81	$0.99 \pm 0.27(0.91 \pm 0.3)$	$-9.31 \pm 54.83(-8.91 \pm 52.50)$
19.21	$1.10 \pm 0.3(1.03 \pm 0.34)$	$-4.19 \pm 10.48(-4.04 \pm 10.12)$
19.69	$1.24 \pm 0.34(1.17 \pm 0.41)$	$-2.61 \pm 3.87(-2.54 \pm 3.78)$
20.10	$1.34 \pm 0.37(1.31 \pm 0.48)$	$-2 \pm 2.23(-1.98 \pm 2.22)$

Table 3.2: The best fit values and their $\pm 1\sigma$ errors for $\omega_{1,2}$ with varying $q^2_{\rm max}$ are shown in this table. The values in the round brackets are evaluated using $A_5^{(1)}$, as opposed to $A_{\rm FB}^{(1)}$.

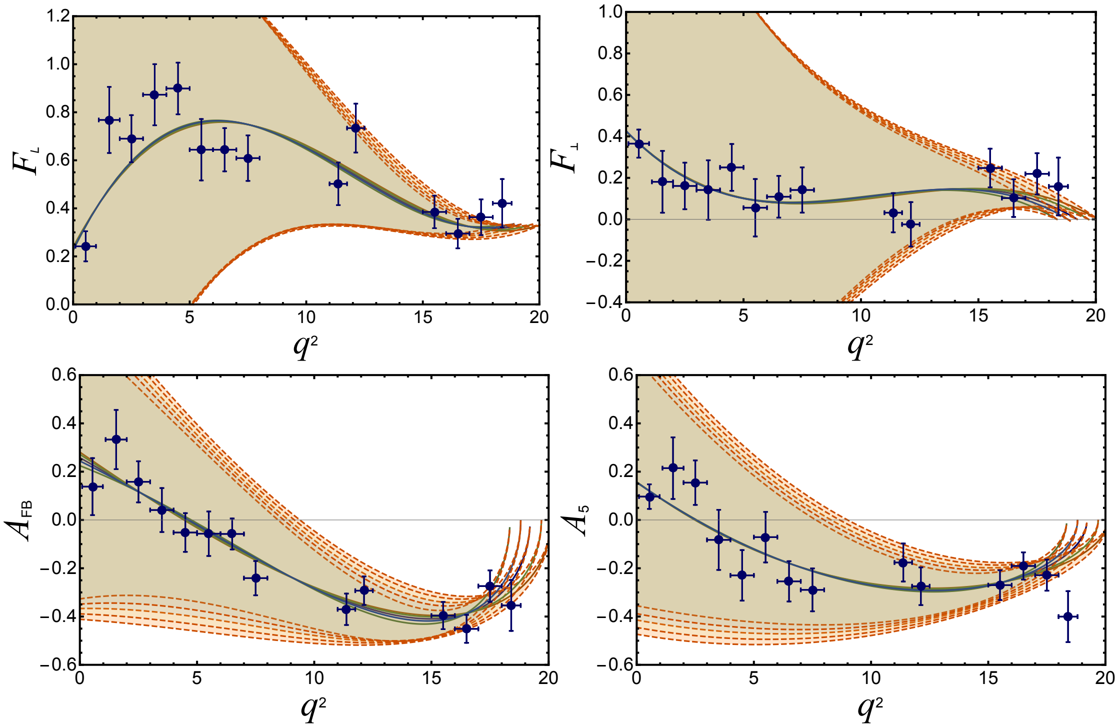

Figure 3.8: The third-order polynomial fits for F_L, $F_\perp$, $A_{\rm FB}$, and A_5 with varying $q^2_{\rm max}$ are shown. The q^2 is in units of GeV^2. The central curves are the best fits while the dashed orange curves along with the light orange shaded region illustrate $\pm 1\sigma$ region surrounding the best fit. The blue crosses illustrate the corresponding experimental data points.

We have taken a weighted average over the Breit-Wigner shape of K^* for $\omega_{1,2}$:

$$\begin{aligned}\omega_1 &= 1.11 \pm 0.30 \; (1.03 \pm 0.35)\\ \omega_2 &= -3.56 \pm 28.34 \; (-3.50 \pm 27.44).\end{aligned} \tag{3.95}$$

These values are consistent with the values quoted in (3.78).

3.4 Summary

To summarize, we have presented a phenomenological framework to uniquely probe for RH currents in $B \to K^* \ell^+ \ell^-$. In this approach we have focused on relations among form factors emerging out of heavy quark symmetry arguments that are extremely reliable at $q^2_{\rm max}$ [44, 52]. This approach differs from others [13] that probe NP at low q^2, as we do not rely on theoretical estimates for the hadronic parameters. Moreover, our parametrization of the amplitudes include non-factorizable loop corrections and power-corrections, in general. We have also used the limiting values of the observables which are kinetically constrained at $q^2_{\rm max}$ which does not change in presence of NP. However, their approach to these values are affected by the nature of NP present in the decay mode. We have parametrized the observables in form of polynomials which are just Taylor expansions around $q^2_{\rm max}$. The latest LHCb measurements are used to fit the polynomials. The data implies a 5σ evidence for RH currents in $B \to K^*\ell^+\ell^-$. However, the significance of RH would be reduced if other kind of NP contributions were present. Varying the lone input parameter r/C_{10}, results in a reduced 3σ evidence for RH currents.

We have also assessed the impact, a variety of non-perturbative and systematic contributions could have on our claims. A comprehensive study on the charm resonance contributions in Sec 3.3.4 reveal that the present data around $q^2_{\rm max}$ can not have significant resonance contributions and even if they did, the evidence for RH currents would have more significance. The systematics of the polynomial fits are discussed in Sec. 3.3.5, where a third order polynomial fit using 14-bin LHCb measurements is chosen as the benchmark. The sanctity of this choice has been illustrated though fits to a 14-bin SM simulated data set. Similarly, the impact of non-zero imaginary contributions and finite K^* width are discussed in Sec. 3.3.6 and Sec. 3.3.7, respectively, where we find that our conclusions remain unaltered. All things considered, we contemplate that if the current feature of data persists even with higher statistics then the presence of RH currents can be established using this approach.

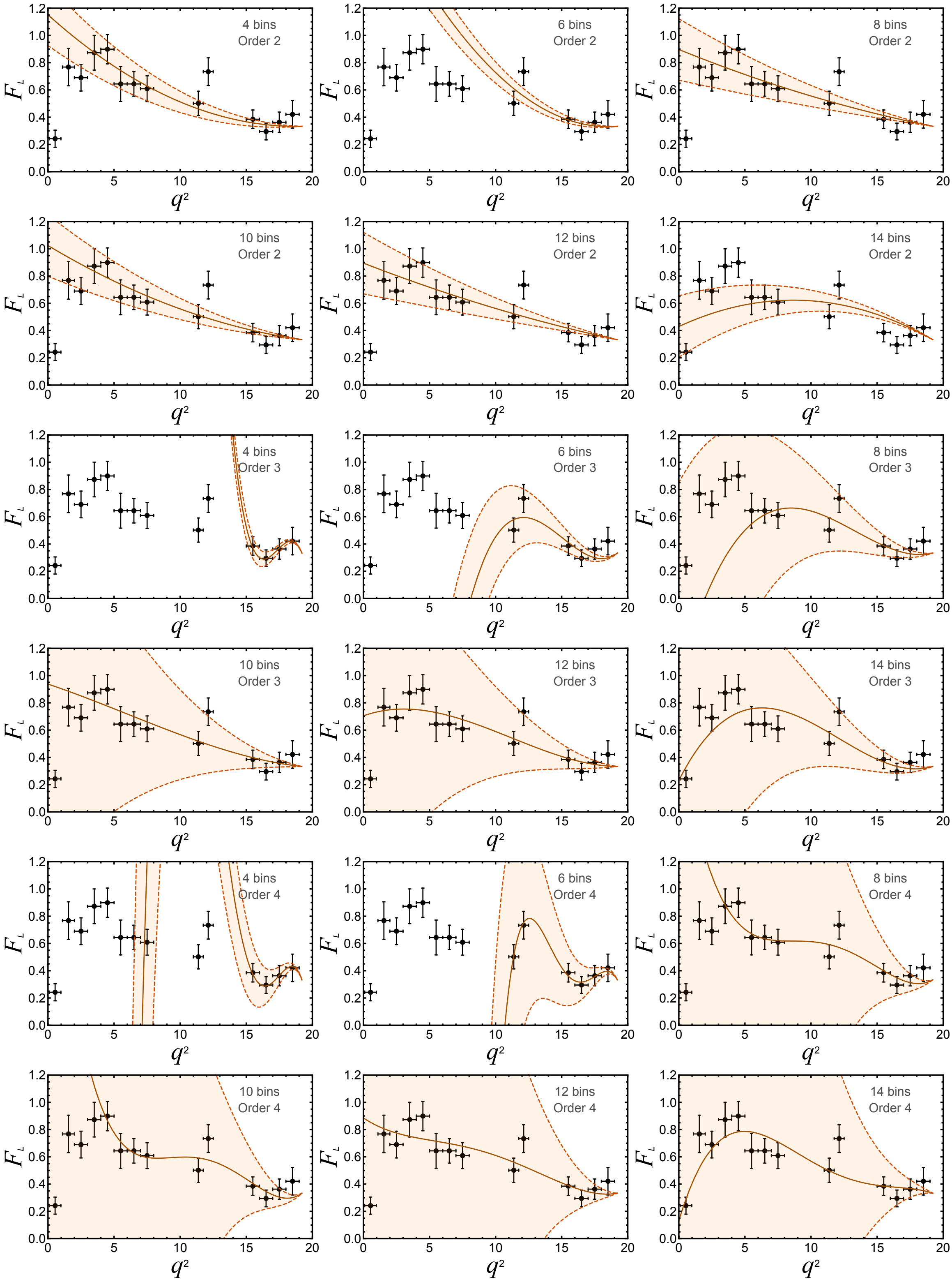

Figure 3.9: Variation of the fits with varying number of bins and varying order of polynomials, in steps of two, for F_L are shown here. The q^2 is in units of GeV^2. The color code and other details are same as that of Fig. 3.2. The values for the fit coefficients are summarized in Fig. 3.7

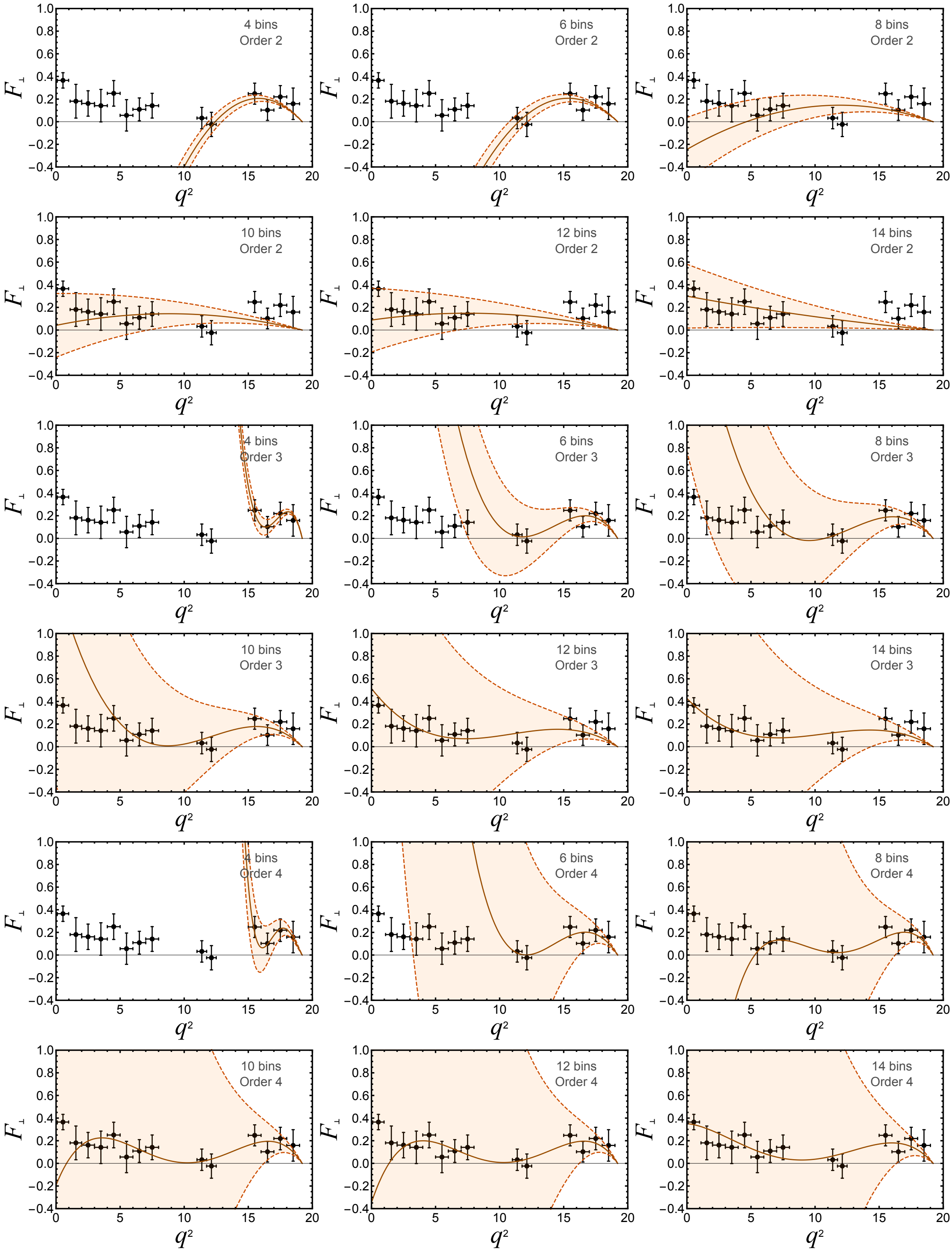

Figure 3.10: Variation of the fits with varying number of bins and varying order of polynomials, in steps of two, for $F_\perp$ are shown here. The q^2 is in units of GeV^2. The color code and other details are same as that of Fig. 3.2. The values for the fit coefficients are summarized in Fig. 3.7

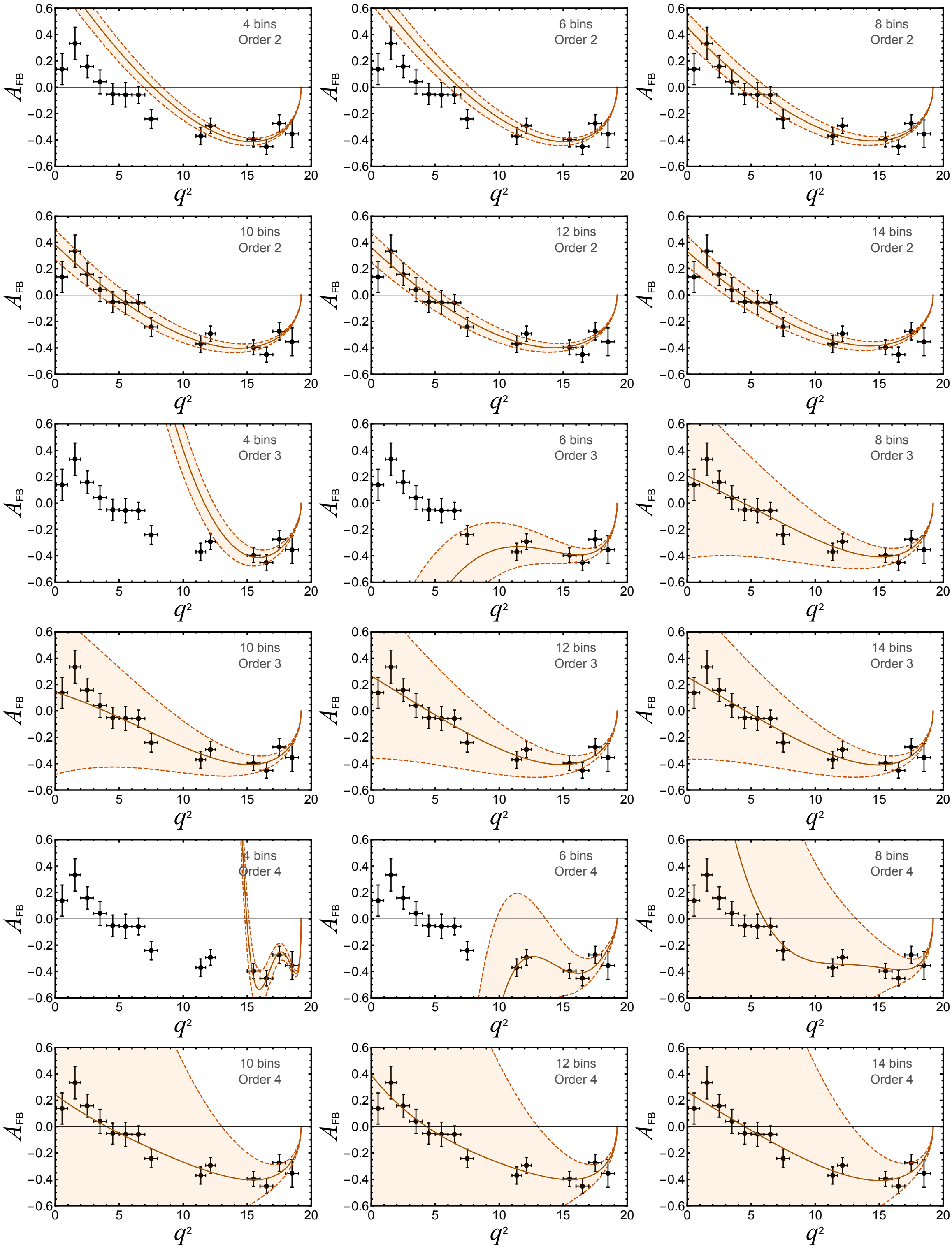

Figure 3.11: Variation of the fits with varying number of bins and varying order of polynomials, in steps of two, for A_{FB} are shown here. The q^2 is in units of GeV^2. The color code and other details are same as that of Fig. 3.2. The values for the fit coefficients are summarized in Fig. 3.7

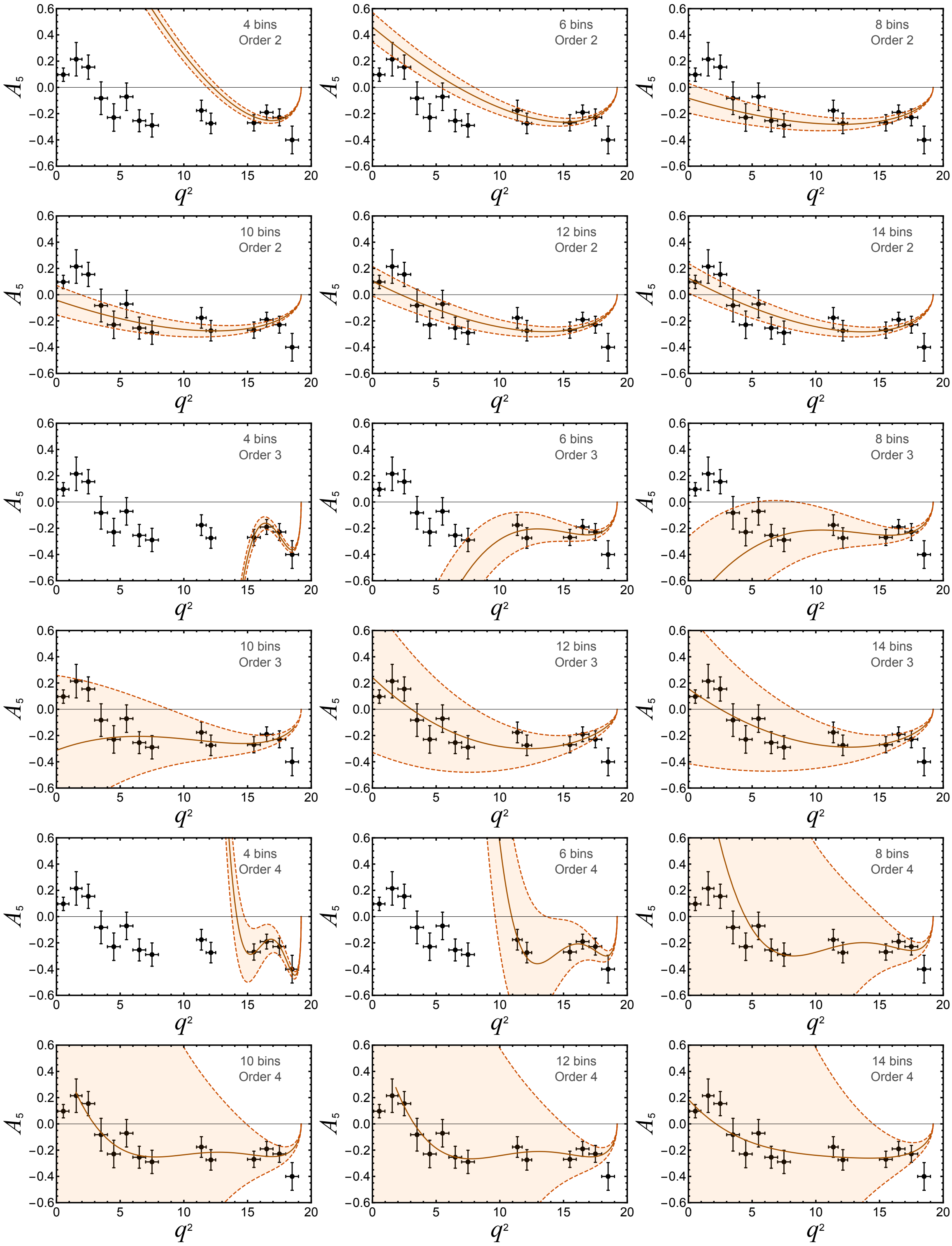

Figure 3.12: Variation of the fits with varying number of bins and varying order of polynomials, in steps of two, for A_5 are shown here. The q^2 is in units of GeV^2. The color code and other details are same as that of Fig. 3.2. The values for the fit coefficients are summarized in Fig. 3.7

Chapter 4

Electroweak penguin pollutions in weak phase α measurement

The contents of this chapter are based on the work done with Rahul Sinha, Anirban Karan, and Benjamin Grinstein in [64].

4.1 Prologue

Symmetries have played a vital role in our understanding of nature. All of our physical theories are based on some form of a symmetric principle, for instance, in the theory of relativity, the speed of light is a symmetry of space-time transformations. The symmetries used in our physical theories can be categorized into space-time symmetries and internal symmetries. The space-time symmetries are transformations that affect the space-time coordinates, in other words, transformations in the 4-vector Minkowski space. These symmetries can be categorized into two distinct forms: *continuous* space-time symmetries and *discrete* space-time symmetries. The *continuous* space-time symmetries are continuous transformations which can be regarded as a series of an infinite number of small steps: Lorentz transformation, translation in space or time, rotations around an axis, etc. On the other hand, *discrete* space-time symmetries are discrete in nature and usually consist of three transformations: parity (P), charge conjugation (C), time reversal (T), etc. The P, C, and T symmetries are of fundamental relevance in physics. On the other hand, the internal symmetries are related to transformations that do not affect the space-time coordinates. These symmetries could be global that are same everywhere in space: baryon number, lepton number, $SU(2)$ isospin, $SU(3)$ isospin, etc., or they could be local that vary over space: $U(1)_Y$ hypercharge, $SU(2)_L$ gauge symmetry, $SU(3)_C$ color symmetry, etc. Out of these intriguing symmetries, we will mostly be talking about P, C, and $SU(2)$ isospin symmetries in this chapter.

The P and C symmetries are defined as invariance under the following transformations:

- parity P – reflecting the space coordinates e.g. $\vec{x} \to -\vec{x}$,
- charge conjugation C – transforming a particle into its antiparticle.

The nature of these transformations had, earlier, lead physicists to propose that P and C should be symmetries of nature at fundamental scales and confirmation of it through experimental observations in electromagnetic and strong interactions had left little doubt about this proposition. However, in 1956, Lee and Yang proposed that P must be violated in order to explain an anomaly observed in Kaon decays. A year later, quite contrary to the popular belief, this was confirmed experimentally by Madam Wu and her collaborators. As a result, it was established that the weak interactions violate parity and that too to the maximum extent. Though shocked, physicists were able to find some peace in the observation that the weak interactions also violate C maximally such that the combination of them, charge-parity or CP, was still conserved by all known interactions. However, in 1964, they were baffled, again, when CP violation was observed for the first time in Kaon decays by Fitch, Cronin *et al.* at BNL. CP violation is more fundamental in the sense that it means nature makes a clear distinction between particle and anti-particle in a convention-independent way, even if CP is violated ever so lightly. It also has important implications for T invariance: as CPT invariance holds naturally in quantum field theories, CP violation could not occur without violating T. Moreover, CP violation represents the most delicately broken symmetry observed so far in nature and acts as a very powerful phenomenological probe. However, inducting CP violation into theories is not an easy task. For instance, P violation could be embedded into gauge theories through chiral coupling even give meaningful definition to maximal P or C violation. For CP and T violation, the situation is completely different. In SM, we use the CKM prescription where it is implemented through complex Yukawa couplings which we will elaborate next.

We start with the SM Lagrangian:

$$\mathcal{L}_{\text{SM}} = \mathcal{L}_{\text{kinetic}} + \mathcal{L}_{\text{Higgs}} + \mathcal{L}_{\text{Yukawa}}. \tag{4.1}$$

The Yukawa part is expressed as,

$$\mathcal{L}_{\text{Yukawa}} = -\tilde{\phi}\bar{Q}_L Y^u u_R - \phi\bar{Q}_L Y^d d_R - \phi\bar{L}_L Y^l l_R + \text{h.c.} \tag{4.2}$$

In the mass basis these terms are diagonalized by linear redefinition of the quark fields,

$$u_L \to V_{u_L} u_L, \quad u_R \to V_{u_R} u_R, \quad d_L \to V_{d_L} d_L, \quad d_R \to V_{d_R} d_R. \tag{4.3}$$

However, these linear transformations must preserve the form of kinetic terms which implies

$$V_{u_L}^{\dagger} V_{u_L} = \mathrm{I}, \tag{4.4}$$

and the off-diagonal terms in gauge interactions give us an unitary matrix

$$V = V_{u_L} V_{d_L}^{\dagger}. \tag{4.5}$$

This is the Cabibbo-Kobayashi-Masakawa (CKM) mixing matrix for quarks or V_{CKM}. As this is not diagonal in the mass basis, $W^{\pm}$ gauge bosons couple to mass eigenstates of quarks belonging to different generations and this is the only source of flavor changing quark interactions as well as CP violation in SM. The parameters of the CKM matrix are fundamental to SM which means their precise measurement carries great significance. It is useful to write the matrix in terms of quarks they connect:

$$\begin{pmatrix} V_{ud} & V_{us} & V_{ub} \\ V_{cd} & V_{cs} & V_{cb} \\ V_{td} & V_{ts} & V_{tb} \end{pmatrix} \tag{4.6}$$

The unitarity of the *CKM* matrix imposes constraints on it's elements:

$$\sum_i V_{ij} V_{ik}^* = \delta_{jk} \quad \text{and} \quad \sum_j V_{ij} V_{kj}^* = \delta_{ik}. \tag{4.7}$$

In other words, the rows and columns of V_{CKM} are orthogonal to each other. These constraints are inherently triangle equations which are aptly referred to as unitarity triangles. Four independent parameters are needed to define the *CKM* matrix. The original parametrization of Kobayashi and Masakawa used three angles $(\theta_1, \theta_2, \theta_3)$ and a *CP*-violating phase δ:

$$\begin{bmatrix} c_1 & -s_1 c_3 & -s_1 s_3 \\ s_1 c_2 & c_1 c_2 c_3 - s_2 s_3 e^{i\delta} & c_1 c_2 s_3 + s_2 c_3 e^{i\delta} \\ s_1 s_2 & c_1 s_2 c_3 + c_2 s_3 e^{i\delta} & c_1 s_2 s_3 - c_2 c_3 e^{i\delta} \end{bmatrix}, \tag{4.8}$$

where, $c_j \equiv \cos\theta_j$ and $s_j \equiv \sin\theta_j$. Various other parametrizations have also been proposed, one of the more commonly used ones is the Wolfenstein parametrization which uses the four parameters λ, A, ρ, and η:

$$\begin{bmatrix} 1 - \frac{1}{2}\lambda^2 & \lambda & A\lambda^3(\rho - i\eta) \\ -\lambda & 1 - \frac{1}{2}\lambda^2 & A\lambda^2 \\ A\lambda^3(1 - \rho - i\eta) & -A\lambda^2 & 1 \end{bmatrix} + \mathcal{O}(\lambda^4). \tag{4.9}$$

In terms of orders of magnitude V_{CKM} may be tentatively expressed as,

$$V_{CKM} \sim \begin{pmatrix} \epsilon^0 & \epsilon^1 & \epsilon^3 \\ \epsilon^1 & \epsilon^0 & \epsilon^2 \\ \epsilon^3 & \epsilon^2 & \epsilon^0 \end{pmatrix} \quad \epsilon \approx 0.1 \tag{4.10}$$

As evident from Eq.(4.7-4.10), not all unitarity triangles are useful as most of them are squashed, with one side being much smaller than the other two e.g. the triangle corresponding to 1st and 2nd column that is $\epsilon^1 + \epsilon^1 + \epsilon^5 = 0$. However, two triangles have sides of comparable sizes e.g. the triangle corresponding to the 1st and 3rd columns, and the 1st and 3rd rows i.e. $\epsilon^3 + \epsilon^3 + \epsilon^3 = 0$. The unitarity conditions corresponding to these triangles are given by

$$V_{ud}V_{ub}^* + V_{cd}V_{cb}^* + V_{td}V_{tb}^* = 0, \tag{4.11}$$

$$V_{ud}V_{td}^* + V_{us}V_{ts}^* + V_{ub}V_{tb}^* = 0. \tag{4.12}$$

The triangle in Eq.(4.11) has been tested extensively experimentally. The triangle is constructed by taking out $V_{cd}V_{cb}^*$ as a common factor. The internal angles of this triangle are defined as

$$\alpha = \arg\left(-\frac{V_{td}V_{tb}^*}{V_{ud}V_{ub}^*}\right), \; \beta = \arg\left(-\frac{V_{cd}V_{cb}^*}{V_{td}V_{tb}^*}\right), \; \gamma = \arg\left(-\frac{V_{ud}V_{ub}^*}{V_{cd}V_{cb}^*}\right), \tag{4.13}$$

and they must add up to π by construction i.e. $\alpha + \beta + \gamma = \pi$, violation of this would undeniably confirm the presence beyond SM physics. Then, the objective is to over-constrain these parameters through various direct or indirect measurements. The direct measurements are mostly accomplished through *CP* violating observables in *B*-meson decays. For instance $B \to \pi\pi, \rho\pi, \rho\rho$ are used for α, while $B \to J/\psi K^0, J/\psi\pi^0, D^{(*)+}D^{(*)-}$ etc are used for β, and $B^\pm \to DK^\pm$ are used for γ measurements [65].

4.2 The *CKM* matrix elements

The *CKM* parameters are fundamental to the Standard Model. In addition, *CP* violation in SM can only be understood through the *CKM* framework, meaning precise measurements of these parameters are important. Consequently, there have been efforts to measure their magnitudes, and phases as accurately as possible.

The magnitudes of the *CKM* elements are obtained through experimental observables in various semi-leptonic, leptonic, or hadronic weak decays. In some cases estimates of form factors are used which are obtained from lattice QCD framework. For instance, $|V_{ud}|$ is extracted from the $0^+ \to 0^+$ nuclear beta decays. These measurements are theoretically clean as it involves pure vector transitions. Similarly, $|V_{cd}|$ is measured using experimental measurements in semileptonic charm decays and theoretical estimates of the corresponding form factors. $|V_{cb}|$ is measured from the inclusive and exclusive decays of B mesons to charm mesons.

In SM, CP violation involves the CKM phases, hence, CP violating observables are used to constrain them. Measuring the CP violation in $K^0 - \bar{K}^0$ mixing renders important information on the CKM matrix. The ϵ and ϵ' are two parameters in terms of which the CP-violating observables in $K^0 - \bar{K}^0$ mixing are expressed. The constraint from ϵ are bounded by approximate hyperbolas in the $\bar{\rho}$, $\bar{\eta}$ plane, see Fig. 4.1. The measurement of $6\ \mathrm{Re}(\epsilon'/\epsilon) = 1 - |\eta_{00}/\eta_{+-}|^2$ is a qualitative test of the CKM mechanism which, in turn, puts strong constraints on several NP models. The observation of its non-zero value, $\mathrm{Re}(\epsilon'/\epsilon) = (1.67 \pm 0.23) \times 10^{-3}$, confirms the presence of direct CP violation [66]. However, due to large hadronic uncertainties, $\mathrm{Re}(\epsilon'/\epsilon) \propto \mathrm{Im}(V_{td}V_{ts}^*)$ is not very useful in extracting the CKM parameters. Most SM estimates are in agreement with this observed value, however, with future improvements, specifically from lattice QCD, we will be able to test these consistencies more accurately.

CP-violating observbles in B-meson decays give direct information on the angles of the unitarity triangle which improve determination of the CKM matrix elements. The time-dependent CP asymmetry of a neutral B decaying to a final state f, common to B^0 and $\bar{B}^0$, is given by [65,67,68]

$$\mathcal{A}_f = \frac{\Gamma(\bar{B}^0(t) \to f) - \Gamma(B^0(t) \to f)}{\Gamma(\bar{B}^0(t) \to f) + \Gamma(B^0(t) \to f)} = S_f \sin(\Delta m_d t) - C_f \cos(\Delta m_d t) \tag{4.14}$$

where,

$$S_f = \frac{2\mathrm{Im}\lambda_f}{1 + |\lambda_f|^2}, \qquad C_f = \frac{1 - |\lambda_f|^2}{1 + |\lambda_f|^2}, \qquad \lambda_f = \frac{q}{p}\frac{\bar{A}_f}{A_f}. \tag{4.15}$$

q/p describes the $B^0 - \bar{B}^0$ mixing and given by, in SM, $q/p = V_{tb}^* V_{td}/V_{tb}V_{td}^* = e^{-2i\beta + \mathcal{O}(\lambda^4)}$.

A_f ($\bar{A}_f$) is the decay amplitude for $B^0 \to f$ ($\bar{B}^0 \to f$). If f is a *CP* eigenstate, and amplitudes with one *CKM* phase dominate the decay process, then $|A_f| = |\bar{A}_f|$, $C_f = 0$, and $S_f = \sin(\arg\lambda_f) = \eta_f \sin 2\phi$, where η_f is the eigenvalue of f and 2ϕ is the phase difference between $B^0 \to f$ and $B^0 \to \bar{B}^0 \to f$ decay paths. A contribution of another amplitude to the decay with a different *CKM* phase makes S_f sensitive to relative strong-interaction phases between the decay amplitudes. For instance, $b \to c\bar{c}s$ decays to *CP* eigenstates ($B^0 \to$ charmonium $K^0_{S,L}$) are used to measure the angle β by measuring $S_f = -\eta_f \sin 2\beta$. Here, the $b \to s$ penguin have dominantly the same weak phase as the $b \to c\bar{c}s$ tree with only λ^2-suppressed penguin amplitudes introducing a different *CP*-violating phase. As a result, amplitudes with a single weak phase dominate the decay, with expectation of $|\bar{A}_{\psi K}/A_{\psi K}| < 0.01$. The e^+e^- asymmetric-energy B-factory experiments, *BABAR* [69] and Belle [70], and LHCb [71] provide precise measurements. The world average, including some other measurements, is [72] $\sin 2\beta = 0.699 \pm 0.017$. The ambiguities in these measurements are resolved by global fits. The $B^0 \to J/\psi\pi^0$ and $B^0 \to D^{(*)+}D^{(*)-}$ can also measure $\sin 2\beta$. Here, the dominant component of the $b \to d$ penguin amplitude has a different *CKM* phase than the tree while having a similar order of magnitude in λ. Consequently, the effects of penguins could be large implying $C_f \neq 0$, $S_f \neq -\eta_f \sin 2\beta$. Measurements by *BABAR*, Belle, and LHCb indicate that the $\sin 2\beta$ is consistent with that from $B^0 \to$ charmonium $K^0_{S,L}$ modes. However, the uncertainties in these measurements are sizable, leaving room for future improvements in understanding the penguin contributions. The $b \to c\bar{u}d$ decays $B^0 \to \bar{D}^{0(*)}h^0$, with $\bar{D}^0 \to CP$ eigenstates and $\bar{D}^0 \to K^0_S\pi^+\pi^-$ with Dalitz plot analysis, have no penguin contributions, and provide theoretically clean $\sin 2\beta$ measurements. The average joint analysis by *BABAR* and Belle data [73–75] give $\sin 2\beta = 0.71 \pm 0.09$ [72]. The $b \to sq\bar{q}$ penguin dominated decays have, up to a very good approximation, the same *CKM* phase as $b \to c\bar{c}s$ tree level decays as $V^*_{tb}V_{ts} = -V^*_{cb}V_{cs}[1 + \mathcal{O}(\lambda^2)]$. Hence, decays such as $B^0 \to \phi K^0$ and $\eta' K^0$ are used in $\sin 2\beta$ measurements in SM. In addition, these modes are used in search of NP as any NP amplitude with a different *CKM* phase would imply $S_f \neq -\eta_f \sin 2\beta$, and possibly $C_f \neq 0$.

The unitary angle γ, by definition, (see Eq.(4.13)) does not depend on *CKM* elements involving the top-quark, hence, can be measured in the tree-level B decays. The absence of heavy loops also mean that the γ extraction is unlikely to be affected by NP. To this end, the interference between $B^- \to D^0K^-$ ($b \to c\bar{u}s$) and $B^- \to \bar{D}^0K^-$ ($b \to u\bar{c}s$) decays are used for extraction of γ. However, the level of uncertainty in these processes is sensitive to the ratio $r_B = |A(B^- \to \bar{D}^0K^-)/A(B^- \to D^0K^-)|$, which is around 0.1 inclusively. There are a few well established methods where various combination of exclusive channels are considered such that the interfering amplitudes become comparable. For instance, the Gronau-London-Wyler(GLW) method [76,77] considers the decays where D decays to CP eigenstates i.e. $B^\pm \to D^{(*)}_{CP}(\to \pi^+\pi^-)K^{(*)\pm}$. Whereas, the Atwood-Dunietz-Soni(ADS) method [78,79] uses the interference among the Cabibbo-allowed $\bar{D}^0$ and doubly-Cabibbo-suppressed D^0 decays to alleviate r_B. The Giri-Grossman-Soffer-Zupan(GGSZ) method [80, 81] involves Dalitz plot analysis of D decaying to CP self-conjugate final states, such as $K^0_S\pi^+\pi^-$. For $B^0_s \to D^\pm_s K^\mp$ the corresponding amplitude ratio is much larger, allowing a model-independent extraction of $\gamma - 2\beta_s$, where a constraint on β_s will have to be used. Combining all the measurements done by Belle, *BABAR*, and LHCb , the γ is constrained as $\gamma = (72.1^{+4.1}_{-4.5})^\circ$.

The information obtained on the *CKM* elements can be used to test for the unitarity of the *CKM* matrix. For instance, $|V_{ud}|^2 + |V_{us}|^2 + |V_{ub}|^2 = 0.9985 \pm 0.0005$, $|V_{cd}|^2 + |V_{cs}|^2 + |V_{cb}|^2 = 1.025 \pm 0.022$, $|V_{ud}|^2 + |V_{cd}|^2 + |V_{td}|^2 = 0.9970 \pm 0.0018$, $|V_{us}|^2 + |V_{cs}|^2 + |V_{ts}|^2 = 1.026 \pm 0.022$, and $\alpha + \beta + \gamma = (179^{+7}_{-6})^\circ$ are obtained, which are consistent with SM. We can also do global fits to all available measurements while imposing all of the unitarity constraints simultaneously. This provides the most precise determination of the *CKM* matrix elements even though the fits require theoretical estimates of hadronic matrix elements. There are several independent groups involved e.g. CKMfitter [18], Ref. [82], and UTfit [83]. The fit results for the triangle in Eq. (4.11) along with constraints on the $\bar{\rho}$, $\bar{\eta}$ plane from various measurements are shown in Fig. 4.1.

4.3 Introduction: Measuring α

The unitarity triangle formed by α, β, and γ (see Eq.(4.13)) has been tested extensively through direct and indirect measurements [18,83] in search for physics beyond the SM. As of now the direct and indirect measurements of the weak phases are in good agreement.

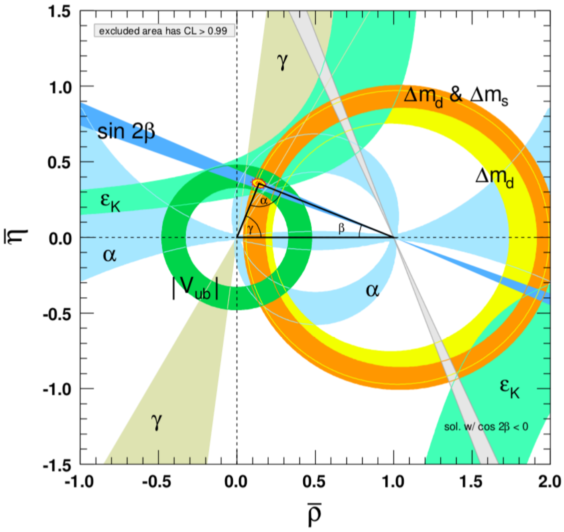

Figure 4.1: The constraints from various measurements are shown here. The shaded areas have a confidence level of 99%.

However, with the increased statistics coming from both the LHCb and Belle II collaborations, more accurate measurements are expected in the future. Hence, it is imperative to formulate methods that are clean and precise in extraction of the weak phases.

The weak phase α is the relative phase between $V_{td}V_{tb}^*$ and $V_{ud}V_{ub}^*$. Consequently, $b \to u\bar{u}d$ decay dominated modes are used for it's extraction. Unlike other modes, where penguin amplitudes are usually suppressed compared to tree amplitudes, the penguins here are of the same order of magnitude in λ but, they do have different *CKM* phases which makes the extraction of α sensitive to the penguin contributions. However, this matter could be settled by using a method of isospin decomposition [14, 85–87] which is used to extract α from $B \to \pi\pi$ and $B \to \rho\rho$ modes. The electroweak penguin can also contribute to these modes and in turn pollute the α measurement, but its contribution is expected to be negligible in SM. However, the electroweak penguins(EWPs) are sensitive to physics beyond the SM hence require careful consideration. There is no exact theoretical estimate available for the EWPs. We propose a method where these contributions can be estimated from experimental data itself. However, in order to achieve this, we need one extra input as isospin framework alone is not enough; we elaborate on what follows.

We begin our theoretical framework by assuming the SM and including electroweak penguin contributions. Our objective is to see how well the theory agrees with the present experimental data. Our sole assumption in this framework is that the indirect measurements of α [18, 83] are in fact the correct value of α and this is our needed extra input. We then estimate the electroweak contributions using available data on $B \to \pi\pi$ and $B \to \rho\rho$ modes. We find that our estimates for these contributions are in fact small and within 1σ from theoretical expectations from SM. Considering current measurements have large errors, there is neither any proof of deviation from SM nor any proof of isospin violation. We also observe that by measuring the time-dependent asymmetry in $B^0 \to \rho^0\rho^0$ we can not only test isospin but also get rid of ambiguities in the solution of α.

The use of $B \to \rho\rho$ in α extraction usually involves some approximations: ρ^0 being a neutral vector meson has substantial mixing with other light neutral vector mesons, e.g. photon, leading to long-distance contributions which can imitate the electroweak penguin contributions; we assume that only $I = 0$ and $I = 2$ isospin amplitudes contribute to the decay mode, however, the $I = 1$ amplitude can also contribute in principle which then would serve as a correction to the isospin prescription; it is assumed in the experimental analysis that transverse polarization contributions are ignorable. We observe that the approximations are indeed valid as $B \to \rho\rho$ works well under these assumptions.

The rest of the chapter is arranged as follows. Sec. 4.4 contains the necessary theoretical framework, followed by Sec. 4.5, where we present our numerical procedure and results. We summarize in Sec. 4.6.

4.4 Thoretical Framework

We begin by describing how to separate the tree and penguin amplitudes in $B \to \pi\pi$. The $B \to \rho\rho$ modes can be treated similarly with some approximations. This is achieved by relating the $B^0 \to \pi^+\pi^-$, $B^0 \to \pi^0\pi^0$ and $B^+ \to \pi^+\pi^0$ decay amplitudes using isospin decomposition. The pions are iso-triplets with each of them having isospin $I = 1$ and third component of isospin equal to their charge $I_z = +1, 0, -1$; as a result, the bose symmetry of identical particles implies that the two pion final states can only be in states with isospin $I = 0$ or $I = 2$. We note further that, the tree diagrams in the decay can lead to both $I = 0$

or $I = 2$ final states [88] whereas the penguin contributions can only lead to $I = 0$ final state [89]. In other words, both the tree and penguin contribute in $\Delta I = 1/2$ (as initial state is in $I = 1/2$ state) transitions while $\Delta I = 3/2$ transitions contains pure tree contributions. Finally, since $\pi^+\pi^0$ can not be in $I = 0$ final state, $B^+ \to \pi^+\pi^0$ happens via $\Delta I = 3/2$ and only gets contribution from the tree diagrams. Now we can expand the $B^0 \to \pi^+\pi^-$, $B^0 \to \pi^0\pi^0$ and $B^+ \to \pi^+\pi^0$ amplitudes (denoted as A^{+-}, A^{00} and A^{+0}, respectively) in terms of the isospin amplitudes corresponding to $I = 0$ and $I = 2$ final states (A_0 and A_2, respectively) [14]:

$$\begin{aligned} \frac{1}{\sqrt{2}}A^{+-} &= A_2 - A_0, \\ A^{00} &= 2A_2 + A_0, \\ A^{+0} &= 3A_2. \end{aligned} \tag{4.16}$$

An immediate consequence of Eq. (4.16) is that the decay amplitudes satisfy a triangle equation in complex plane,

$$\frac{1}{\sqrt{2}}A^{+-} + A^{00} = A^{+0}. \tag{4.17}$$

Similarly, the relation among the charge conjugated counterparts is given by,

$$\frac{1}{\sqrt{2}}\bar{A}^{+-} + \bar{A}^{00} = \bar{A}^{+0}. \tag{4.18}$$

The amplitudes $\bar{A}^{+-}$, $\bar{A}^{00}$, and $\bar{A}^{+0}$ correspond to the charge-conjugated processes (i.e. $\bar{B}^0 \to \pi^+\pi^-$, $\bar{B}^0 \to \pi^0\pi^0$, and $B^- \to \pi^-\pi^0$, respectively) and are obtained from A^{ij} (i, j correspond to $+$, $-$, or 0) by simply changing the sign of the weak phase.

The decay amplitude can also expressed in terms of complex topologies or graph contributions. Taking account of all possible penguin diagrams, the decay amplitudes can in general be written as [15, 16]

$$\begin{aligned} \frac{1}{\sqrt{2}}A^{+-} &= (T + E)e^{i\gamma} + (P + \frac{2}{3}P^C_{EW})e^{-i\beta}, \\ A^{00} &= (C - E)e^{i\gamma} + (P_{EW} + \frac{1}{3}P^C_{EW} - P)e^{-i\beta}, \end{aligned}$$

$$A^{+0} = (T+C)e^{i\gamma} + (P_{EW} + P^C_{EW})e^{-i\beta}. \tag{4.19}$$

The complex topologies T, C, P, P_{EW}, and P^C_{EW} are referred as "tree", "color-suppressed-tree", "penguin", "electroweak-penguin", and "color-suppressed electroweak-penguin" amplitudes correspondingly and they include strong phases. There could also be a tiny penguin annihilation contribution to the B^0 decay modes but it does not affect the isospin relations in Eq. (4.17-4.18). The conjugate amplitudes are obtained by switching the sign of the weak phases:

$$\begin{aligned}
\frac{1}{\sqrt{2}}\bar{A}^{+-} &= (T+E)e^{-i\gamma} + (P + \frac{2}{3}P^C_{EW})e^{i\beta}, \\
\bar{A}^{00} &= (C-E)e^{-i\gamma} + (P_{EW} + \frac{1}{3}P^C_{EW} - P)e^{i\beta}, \\
\bar{A}^{+0} &= (T+C)e^{-i\gamma} + (P_{EW} + P^C_{EW})e^{i\beta}.
\end{aligned} \tag{4.20}$$

Note that these amplitudes still satisfy the isospin triangle relations in Eq. (4.17-4.18). It is convenient to redefine the amplitudes of the decay modes and their conjugated counterparts by rotating them by $e^{-i\gamma}$ and $e^{i\gamma}$, respectively:

$$\begin{aligned}
\tilde{A}^{+-} &= e^{-i\gamma}A^{+-}, \quad \tilde{A}^{00} = e^{-i\gamma}A^{00}, \quad \tilde{A}^{+0} = e^{-i\gamma}A^{+0} \\
\tilde{\bar{A}}^{+-} &= e^{i\gamma}\bar{A}^{+-}, \quad \tilde{\bar{A}}^{00} = e^{i\gamma}\bar{A}^{00}, \quad \tilde{\bar{A}}^{+0} = e^{i\gamma}\bar{A}^{+0}.
\end{aligned} \tag{4.21}$$

It is clear that these redefinitions does not affect the isospin triangle relations in Eq. (4.17-4.18). The observable definitions are also not altered by such redefinitions. Using the unitarity triangle relation $\beta + \gamma = \pi - \alpha$, we can cast the amplitudes in Eq. (4.19) in terms of a single weak phase α:

$$\begin{aligned}
\frac{1}{\sqrt{2}}\tilde{A}^{+-} &= (T+E) + Xe^{i\alpha}, \\
\tilde{A}^{00} &= (C-E) + Ye^{i\alpha}, \\
\tilde{A}^{+0} &= (T+C) + (X+Y)e^{i\alpha},
\end{aligned} \tag{4.22}$$

where, $X = (-P - \frac{2}{3}P^C_{EW})$ and $Y = (P - P_{EW} - \frac{1}{3}P^C_{EW})$. The corresponding conjugate amplitudes are given by,

$$\begin{aligned}
\frac{1}{\sqrt{2}}\tilde{\bar{A}}^{+-} &= (T+E) + Xe^{-i\alpha}, \\
\tilde{\bar{A}}^{00} &= (C-E) + Ye^{-i\alpha}, \\
\tilde{\bar{A}}^{+0} &= (T+C) + (X+Y)e^{-i\alpha}. \qquad (4.23)
\end{aligned}$$

An important observation at this point is that the quantity $X+Y(= -P_{EW} - P^C_{EW})$, only depends on the electroweak penguins and color suppressed electroweak penguins [15]. In other words, $X+Y$ serves as a measure of pure electroweak contributions in $B \to \pi\pi$ modes. The redefined amplitudes follow the same isospin relation i.e.

$$\begin{aligned}
\frac{1}{\sqrt{2}}\tilde{A}^{+-} + \tilde{A}^{00} &= \tilde{A}^{+0}, \\
\frac{1}{\sqrt{2}}\tilde{\bar{A}}^{+-} + \tilde{\bar{A}}^{00} &= \tilde{\bar{A}}^{+0}. \qquad (4.24)
\end{aligned}$$

The relations in Eq.(4.24) are inherent triangle equations in the complex plane. As we know, any two triangles can be fully described, up to a finite ambiguity, by lengths of the sides and a relative angle between any related side of the two triangles. In other words, we require seven pieces of information. Six of these are provided by measurements of the branching fractions B_{ij} and the direct CP asymmetries C_{ij} for each of the $B \to \pi\pi$ modes. The B_{ij} and C_{ij} are defined as

$$B_{ij} = \frac{|\tilde{A}^{ij}|^2 + |\tilde{\bar{A}}^{ij}|^2}{2}, \qquad C_{ij} = \frac{|\tilde{A}^{ij}|^2 - |\tilde{\bar{A}}^{ij}|^2}{|\tilde{A}^{ij}|^2 + |\tilde{\bar{A}}^{ij}|^2}. \qquad (4.25)$$

These two observables together render full information about each individual triangle but say nothing about the relative orientation between them, we require one more piece of information. The measurement of the time-dependent CP asymmetry in $B \to \pi^+\pi^-$ or S_{+-}, which is related to the phase between $\tilde{A}^{ij}$ and $\tilde{\bar{A}}^{ij}$, provides the seventh information. S_{+-} is defined as

$$\begin{aligned}
S_{+-} &= \sqrt{1 - C^2_{+-}}\,\sin(2\alpha^{\text{eff}}), \\
\text{where,} \quad 2\alpha^{\text{eff}} &= 2\alpha + 2\Delta\alpha \quad \text{or} \quad \pi - 2\alpha^{\text{eff}} = 2\alpha + 2\Delta\alpha. \qquad (4.26)
\end{aligned}$$

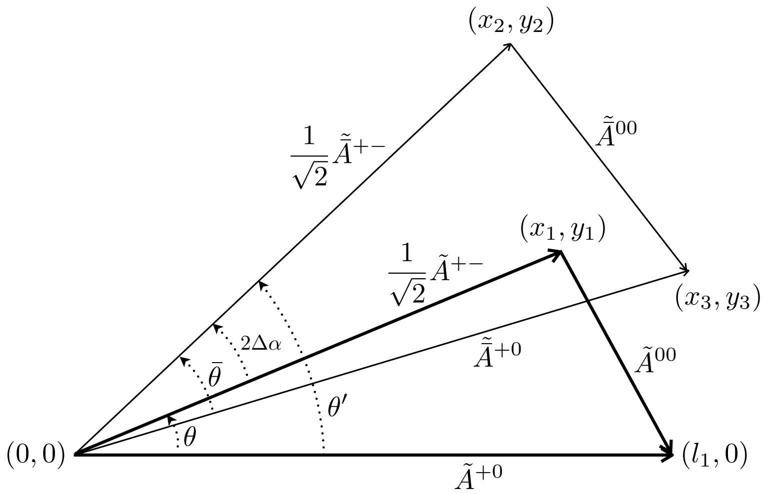

Figure 4.2: An illustration of the isospin triangles depicted in the complex coordinate plane. The figure defines the notation of coordinates and angles used to obtain the solutions of decay amplitudes including ambiguities. There is a sixteen-fold ambiguity in the solutions of coordinates as can be seen from Eq. (4.28), hence, there are sixteen distinct orientations of the triangles drawn in this figure. However, only eight solutions result in the correct value of $2\alpha^{\text{eff}}$.

$2\Delta\alpha$ is the relative phase between $\tilde{\tilde{A}}^{+-}$ and $\tilde{A}^{+-}$. As evident from the above equation, the measurement of $2\alpha^{\text{eff}}$ alone is not enough to determine $2\Delta\alpha$, we need to know α beforehand. Here, we assume that the indirect measurements are a true measure of α and use this value as an input to estimate $2\Delta\alpha$. A diagrammatic presentation of the two resulting isospin triangles, in the complex coordinate frame, is given in Fig. 4.2.

In conventional α measurements, the electroweak penguins are neglected (i.e. $X + Y \to 0$) which leads to $\tilde{\tilde{A}}^{+0} = \tilde{A}^{+0}$ (see Eq. (4.22-4.23)) and $2\Delta\alpha$ can be calculated using just the seven observables. In other words, the relative orientation of the two triangles gets fixed up to a finite ambiguity and α can be measured directly from α^{eff} with ambiguities. In presence of the electroweak penguin, there are four independent combinations of complex topologies i.e. $T + E$, $C - E$, X, and Y, and considering that the overall phase is immaterial, we have seven independent hadronic parameters to solve for. It is clear that we can not solve for these parameters as well as α from seven measurements hence we use the indirectly measured value of α and translate the difference between the "direct" and "indirect" measurements to a bound on $\Delta\alpha$ and, in turn, the electroweak penguins.

From Fig. 4.2, it is easy to express the magnitudes of each side in terms of the coordinates and also the observables:

$$
\begin{aligned}
\tfrac{1}{2}|\tilde{A}^{+-}|^2 &= x_1^2 + y_1^2 = \tfrac{1}{2}\{B_{+-}(1+C_{+-})\} \\
|\tilde{A}^{+0}|^2 &= l_1^2 = B_{+0}(1+C_{+0}) \\
|\tilde{A}^{00}|^2 &= (x_1 - l_1)^2 + y_1^2 = B_{00}(1+C_{00}) \\
\tfrac{1}{2}|\tilde{\bar{A}}^{+-}|^2 &= x_2^2 + y_2^2 = \tfrac{1}{2}\{B_{+-}(1-C_{+-})\} \\
|\tilde{\bar{A}}^{+0}|^2 &= x_3^2 + y_3^2 = B_{+0}(1-C_{+0}) \\
|\tilde{\bar{A}}^{00}|^2 &= (x_3 - x_2)^2 + (y_3 - y_2)^2 = B_{00}(1-C_{00}).
\end{aligned}
\tag{4.27}
$$

The solutions for the coordinates in terms of the observables are given by,

$$
\begin{aligned}
l_1 &= |\tilde{A}^{+0}| \\
x_1 &= \tfrac{1}{\sqrt{2}}|\tilde{A}^{+-}|\cos\theta \\
y_1 &= \tfrac{1}{\sqrt{2}}|\tilde{A}^{+-}|\sin\theta \\
x_2 &= \tfrac{1}{\sqrt{2}}|\tilde{\bar{A}}^{+-}|\cos\theta' \\
y_2 &= \tfrac{1}{\sqrt{2}}|\tilde{\bar{A}}^{+-}|\sin\theta' \\
x_3 &= |\tilde{\bar{A}}^{+0}|\cos(\theta' - \bar{\theta}) \\
y_3 &= |\tilde{\bar{A}}^{+0}|\sin(\theta' - \bar{\theta})
\end{aligned}
\tag{4.28}
$$

where the phases θ, θ', $\bar{\theta}$ and $2\Delta\alpha$ are depicted in Fig. 4.2. There is an overall sixteen fold ambiguity in the above coordinate solutions which means we have sixteen different triangles but only eight of them give the correct value of $2\alpha^{\text{eff}}$: θ and $\bar{\theta}$ are obtained using the cosine law from their respective triangles which means both of them have twofold ambiguities and $2\Delta\alpha$, with correct convention, too has a two-fold ambiguity given by $2\Delta\alpha = 2\alpha^{\text{eff}} - 2\alpha$ or $2\Delta\alpha = \pi - 2\alpha^{\text{eff}} - 2\alpha$. Hence, together we have an eightfold ambiguity in our solutions for the amplitudes. This is according to expectation as the weak phase α is measured with an eightfold ambiguity using conventional methods. The right-hand side of Eq. (4.28) can be expressed completely in terms of observables; for the sake of compactness, we have refrained from doing so.

	$B \to \pi\pi$	$B \to \rho\rho$
$B_{+-} \times 10^{-5}$	0.512 ± 0.019	2.77 ± 0.19
C_{+-}	-0.32 ± 0.04	0.0 ± 0.09
S_{+-}	-0.63 ± 0.04	-0.14 ± 0.13
$\mathrm{corr}(C_{+-}, S_{+-})$	0.21	−0.02
$B_{00} \times 10^{-5}$	0.159 ± 0.026	0.096 ± 0.015
C_{00}	-0.33 ± 0.22	0.2 ± 0.85
S_{00}	-	0.3 ± 0.73
$\mathrm{corr}(C_{00}, S_{00})$	-	0.0
$B_{+0} \times 10^{-5}$	0.55 ± 0.04	2.4 ± 0.19
C_{+0}	-0.03 ± 0.04	0.05 ± 0.05
α	91.8 ± 2.88	

Table 4.1: The table shows the used experimental values of the branching fraction, direct CP asymmetry and time-dependent CP asymmetry of $B \to \pi\pi$ and $B \to \rho\rho$ modes observed in [18,19,65,91], respectively. Note that in order to maintain consistency between the definitions of C_{ij} in [18, 19, 65, 91] and Eq. (4.25), the signs of C_{+0} in Table 4.1 has been reversed as compared to the values reported in [18, 19, 65, 91].

We use the available experimental data to obtain the coordinate which in turn will render the full complex decay amplitudes. The data used for this analysis are shown in Table. 4.1. The observables are simulated as normal distributions around their central values with errors and available correlations. In other words, each time we use the value of an observable in Eq. (4.28) means that we are picking a random value from that observable's simulated profile. We make sure that the simulated data sets are physically allowed by imposing the triangle inequalities (which makes sure that the triangle is closed) and $-1 \leq \{C_{ij}, S_{ij}\} \leq 1$. Each of the physical data set gives us eight equivalent solutions of the amplitudes. We observe that the triangles obtained by the simulated observables close in for around half of the time for $B \to \pi\pi$ modes whereas the odds drop to a few percent for $B \to \rho\rho$ modes. This closure depends on isospin bounds [16,90] on B_{00}. Since the observed values of B_{00} are really small and barely satisfy the isospin bounds, the small odds for triangle getting close is expected for both $B \to \pi\pi$ and $B \to \rho\rho$ modes.

Once we have determined the decay amplitudes, it's straightforward to calculate the hadronic parameters $T + E$, $C - E$, X, and Y. We can also estimate the observable S_{00} which is not yet measured in $B^0 \to \pi^0\pi^0$ but has been measured in $B^0 \to \rho^0\rho^0$. Our primary objective is to estimate the size of electroweak contributions or $X + Y$. For a better grasp on the numbers, we normalize our hadronic parameters by the dominant tree contributions $|T+C|$ and define the desired quantities as $\mathcal{R}_P = \{\tilde{X}, \tilde{Y}, \tilde{X}+\tilde{Y}\}$:

$$\begin{aligned}
\tilde{X} &= \frac{X}{|T+C|}, \\
\tilde{Y} &= \frac{Y}{|T+C|}, \\
\tilde{X}+\tilde{Y} &= \frac{X+Y}{|T+C|} \equiv z e^{i\delta_{TC}},
\end{aligned} \tag{4.29}$$

where z is defined in Eq. (4.32) and δ_{TC} is the strong phase of $T+C$.

As discussed earlier in this section, the $B^{\pm} \to \pi^{\pm}\pi^{0}$ decay only gets contribution from $\Delta I = \frac{3}{2}$ part of the Hamiltonian. In presence of electroweak penguins, $\Delta I = \frac{3}{2}$ operators has both tree and electroweak penguin contributions; and they can be related by assuming that only C_7 and C_8 are neglected [17]:

$$\mathcal{H}^{EW}_{\Delta I=\frac{3}{2}} = -\frac{3}{2}\frac{V_{tb}V_{td}}{V_{ub}V_{ud}}\frac{C_9+C_{10}}{C_1+C_2}\mathcal{H}^{\text{tree}}_{\Delta I=\frac{3}{2}} \tag{4.30}$$

The amplitudes $\tilde{\bar{A}}^{+0}$, $\tilde{A}^{+0}$ can be expressed here as

$$\begin{aligned}
\tilde{A}^{+0} &= (T+C) + z e^{i\alpha}(T+C), \\
\tilde{\bar{A}}^{+0} &= (T+C) + z e^{-i\alpha}(T+C),
\end{aligned} \tag{4.31}$$

where,

$$z = -\frac{3}{2}\left|\frac{V_{tb}V_{td}}{V_{ub}V_{ud}}\right|\frac{C_9+C_{10}}{C_1+C_2} \approx -0.013\left|\frac{V_{tb}V_{td}}{V_{ub}V_{ud}}\right|. \tag{4.32}$$

Eq. (4.32) serves as a theoretical estimate for z in this analysis. The value of ratio of CKM elements $(V_{tb}V_{td})/(V_{ub}V_{ud})$ are taken from Ref. [18].

4.5 Numerical Analysis

4.5.1 Topological Amplitudes:

The decay amplitudes can be cast in a general form:

$$\begin{aligned}\tilde{A}^{ij} &= \mathcal{O}_1 + \mathcal{O}_2 e^{i\alpha},\\ \tilde{\bar{A}}^{ij} &= \mathcal{O}_1 + \mathcal{O}_2 e^{-i\alpha}.\end{aligned} \tag{4.33}$$

The solution to $\mathcal{O}_1$ and $\mathcal{O}_2$ are then given by,

$$\mathcal{O}_1 = \frac{\tilde{\bar{A}}^{ij} e^{i\alpha} - \tilde{A}^{ij} e^{-i\alpha}}{2i \sin\alpha}, \qquad \mathcal{O}_2 = \frac{\tilde{A}^{ij} - \tilde{\bar{A}}^{ij}}{2i \sin\alpha}. \tag{4.34}$$

As a result, given $\tilde{A}^{ij}$ and $\tilde{\bar{A}}^{ij}$ these hadronic parameters can be known. As mentioned in Sec. 4.4, the observables are simulated around their measured central values. As a result, our desired quantities or ratios are also distributions of sample points. We fit these distributions to possible probability distribution functions or PDFs from where required confidence levels are drawn.

We present the 68.27% and 95.45% confidence levels of $\mathcal{R}_P$ and S_{00} for $B \to \pi\pi$ decays in Fig. 4.4. The solution, one of the possible eight, illustrated in Fig. 4.3 shows that the estimate for $\tilde{X} + \tilde{Y}$ agrees with the SM within 68.27% confidence level. The light gray, light blue and light green contours correspond to the topological ratios $\tilde{X} + \tilde{Y}$, $\tilde{X}$ and $\tilde{Y}$, respectively. The gray, blue and green points show the mean value of the PDFs corresponding to $\tilde{X} + \tilde{Y}$, $\tilde{X}$ and $\tilde{Y}$, respectively and similarly the vectors connecting them to the origin. The'•' at the center indicates origin while the '♦' symbol at -0.0327 indicates an SM estimate for z. As seen in the right panel figure of Fig. 4.3, S_{00} has been estimated to have positive values; however if S_{00} is measured to be negative while rest of the experimental data remain unchanged then it is clear that we have to discard this solution. In other words, measurement of the time-dependent asymmetry S_{00} can help reduce or even eliminate the ambiguity.

Recall that there are seven other possible solutions. Five of them together with the one in

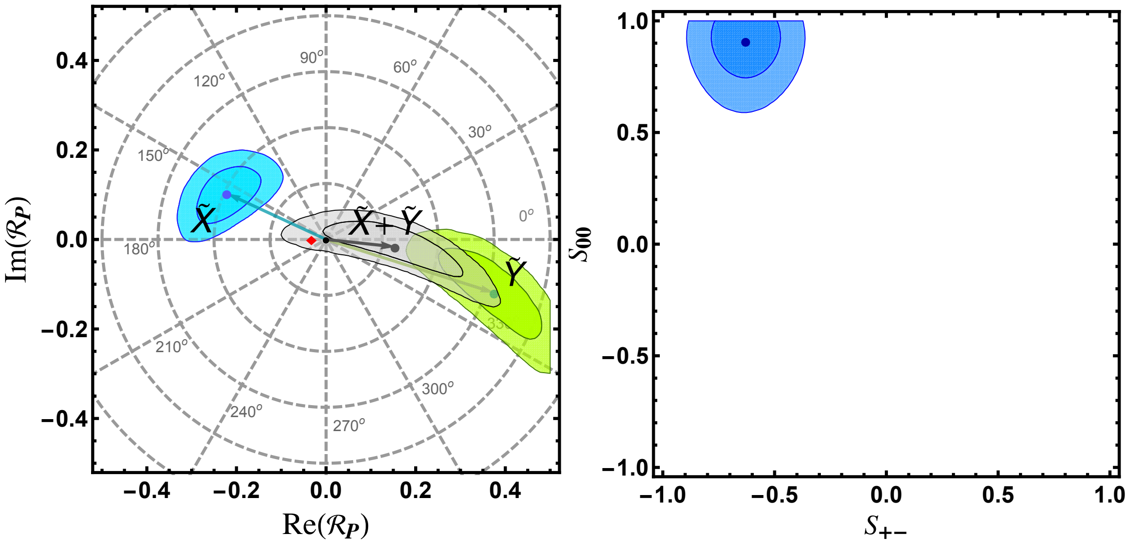

Figure 4.3: The estimated 68.27% and 95.45% confidence levels for the topological ratios (left panel) and S_{00} versus S_{+-} (right panel) for $B \to \pi\pi$ modes are depicted. The light gray, light blue and light green contours correspond to the topological ratios $\tilde{X}+\tilde{Y}$, $\tilde{X}$ and $\tilde{Y}$, respectively. The gray, blue and green points show the mean value of the PDFs corresponding to $\tilde{X}+\tilde{Y}$, $\tilde{X}$ and $\tilde{Y}$, respectively and similarly the vectors connecting them to the origin. The '•' at the center indicates origin while the '♦' symbol at -0.0327 indicates the SM estimate for z.

Fig. 4.3 are shown in Fig. 4.4. The remaining two solutions are ignored as they indicate very large penguin contributions and are, in turn, far from the SM expectations.

Similar estimates of the topological ratios (left panel) and S_{00} versus S_{+-} (right panel) for $B \to \rho\rho$ are depicted in Fig. 4.5. The details of the figures are the same as those of Fig. 4.3. Four of the eight possible solutions are presented here. The estimates for $\tilde{X}+\tilde{Y}$ are in good agreement with SM for all of these four solutions. The remaining four solutions are ignored as they indicate very large penguin contributions and are, in turn, very very far from the SM expectations. The gray band in S_{00} versus S_{+-} (right panel) figures correspond to the 1σ region of measured S_{00} for $B^0 \to \rho^0\rho^0$. It is clear that more accurate measurements of S_{00} can identify the correct ambiguity.

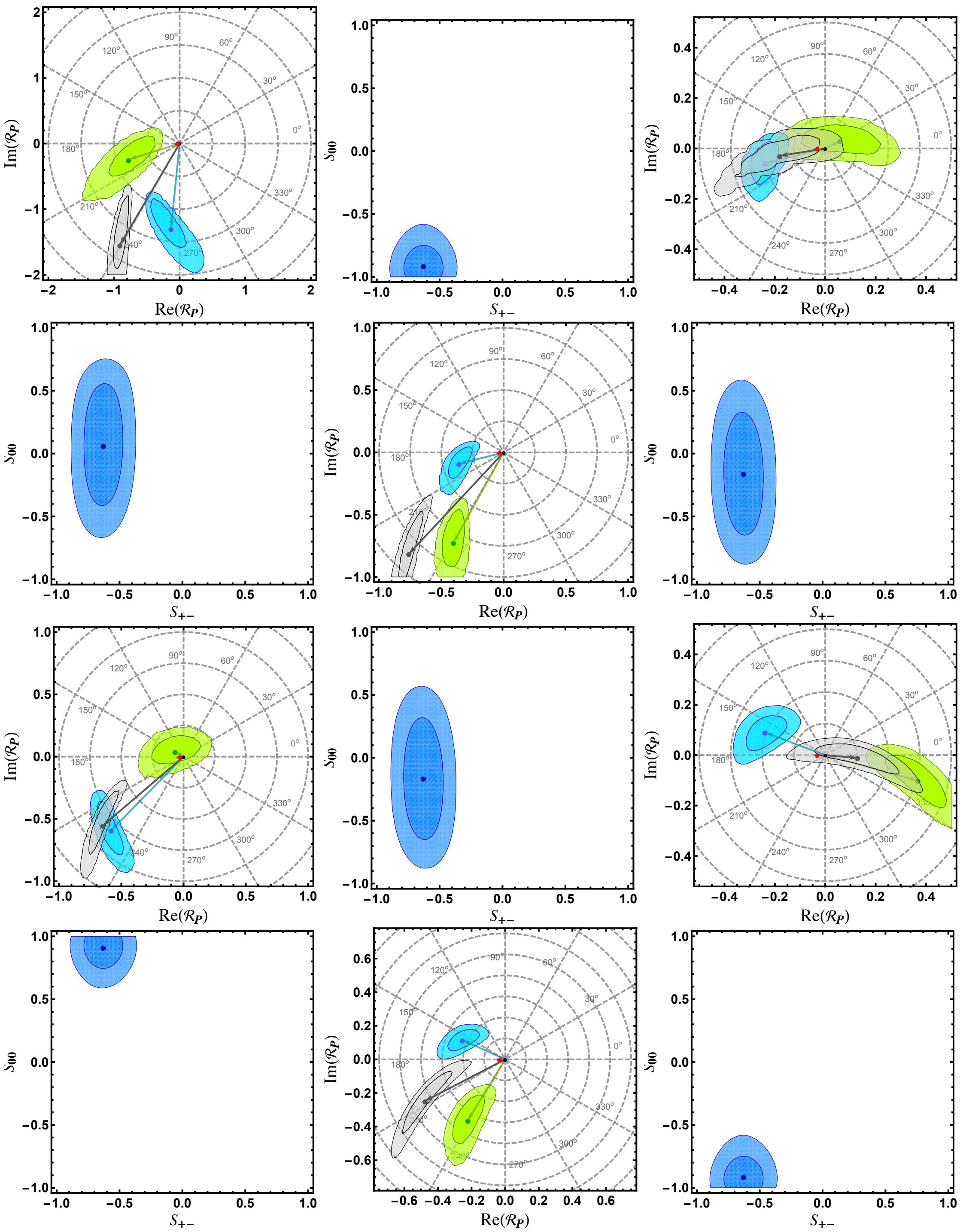

Figure 4.4: Six of the eight possible solutions and their corresponding estimates for S_{00} versus S_{+-} (right next to the solution) are illustrated. The light gray, light blue and light green contours correspond to 68.27% and 95.45% confidence levels of the topological ratios $\tilde{X}+\tilde{Y}$, $\tilde{X}$ and $\tilde{Y}$, respectively. The gray, blue and green points show the mean value of the PDFs corresponding to $\tilde{X}+\tilde{Y}$, $\tilde{X}$ and $\tilde{Y}$, respectively and similarly the vectors connecting them to the origin. The'•' at the center indicates origin while the '♦' symbol at -0.0327 indicates the SM estimate for z.

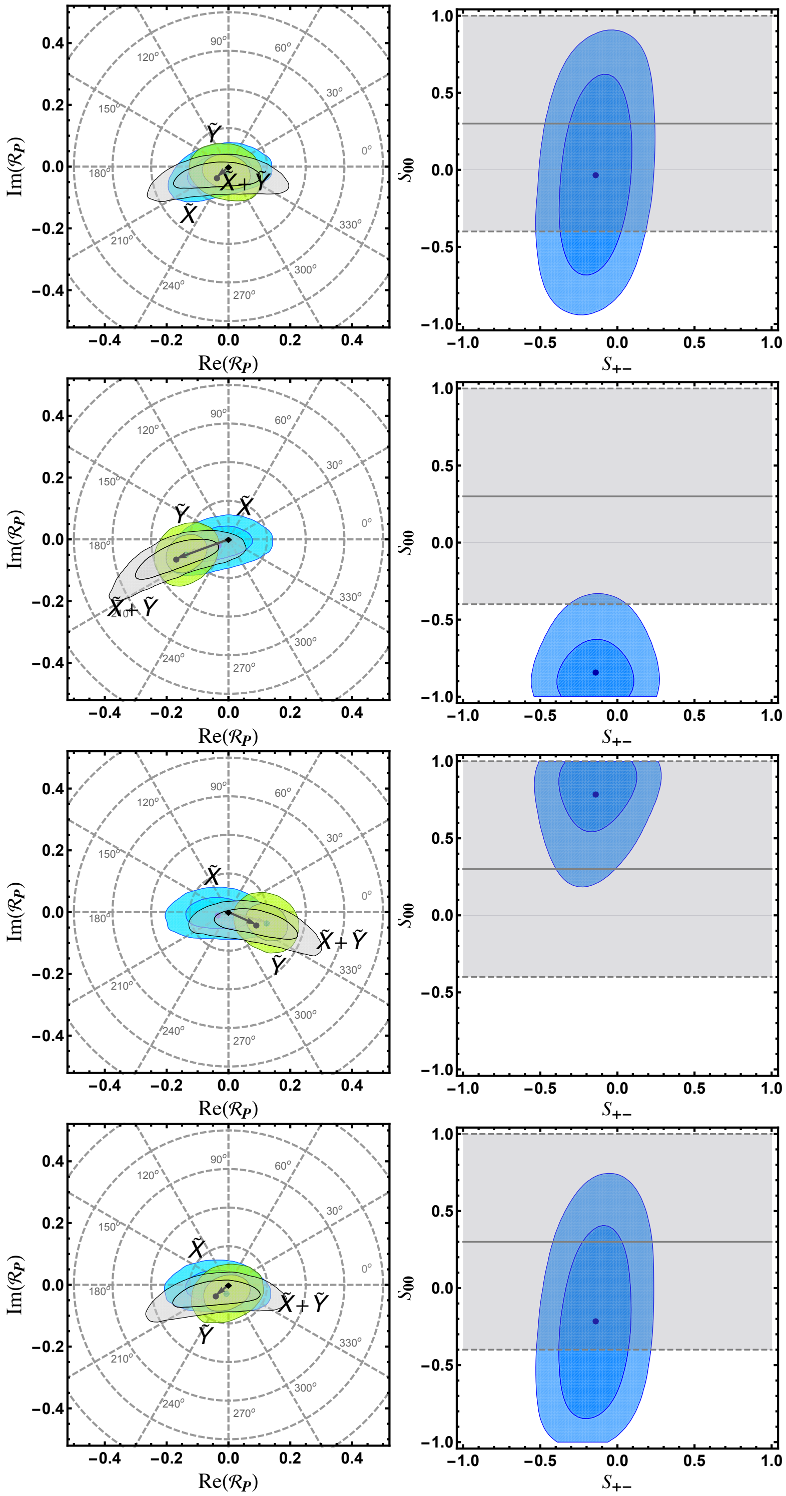

Figure 4.5: The topological amplitudes (left panel) and S_{00} versus S_{+-} (right panel) are depicted for $B \to \rho\rho$ modes. The color codes and other details are the same as in Fig. 4.3. The estimates for $\tilde{X}+\tilde{Y}$ are in good agreement with SM for all of these solutions. The gray band in S_{00} versus S_{+-} (right panel) figures correspond to the 1σ region of measured S_{00} for $B^0 \to \rho^0\rho^0$. It is clear that more accurate measurements of S_{00} can help in identifying the correct ambiguity.

4.5.2 Isospin Amplitudes:

As mentioned in Eq. (4.16), the decay amplitudes can be expanded in terms isospin amplitudes. Under redefinitions (see Eq. (4.21)) Eq. (4.16) transforms as follows

$$\begin{aligned}\frac{1}{\sqrt{2}}\tilde{A}^{+-} &= \tilde{A}_2 - \tilde{A}_0,\\ \tilde{A}^{00} &= 2\tilde{A}_2 + \tilde{A}_0,\\ \tilde{A}^{+0} &= 3\tilde{A}_2.\end{aligned} \tag{4.35}$$

Similarly, the conjugate amplitudes transform as

$$\begin{aligned}\frac{1}{\sqrt{2}}\tilde{\bar{A}}^{+-} &= \tilde{\bar{A}}_2 - \tilde{\bar{A}}_0,\\ \tilde{\bar{A}}^{00} &= 2\tilde{\bar{A}}_2 + \tilde{\bar{A}}_0,\\ \tilde{\bar{A}}^{+0} &= 3\tilde{\bar{A}}_2.\end{aligned} \tag{4.36}$$

The rotated isospin amplitudes are given by

$$\begin{aligned}\tilde{A}_0 &= e^{-i\gamma}A_0, \quad \tilde{A}_2 = e^{-i\gamma}A_2,\\ \tilde{\bar{A}}_0 &= e^{i\gamma}\bar{A}_0, \quad \tilde{\bar{A}}_2 = e^{i\gamma}\bar{A}_2.\end{aligned} \tag{4.37}$$

A graphical presentation of Eq. (4.35-4.36) is depicted in Fig. 4.6. The isospin amplitudes $\tilde{A}_0$, $\tilde{A}_2$, $\tilde{\bar{A}}_0$ and $\tilde{\bar{A}}_2$ can be easily expressed in terms of the decay amplitudes:

$$\begin{aligned}\tilde{A}_0 &= \tilde{A}^{00} - \frac{2}{3}\tilde{A}^{+0}, \quad \tilde{A}_2 = \frac{1}{3}\tilde{A}^{+0},\\ \tilde{\bar{A}}_0 &= \tilde{\bar{A}}^{00} - \frac{2}{3}\tilde{\bar{A}}^{+0}, \quad \tilde{\bar{A}}_2 = \frac{1}{3}\tilde{\bar{A}}^{+0}.\end{aligned} \tag{4.38}$$

They can also be expressed in terms of topological amplitudes:

$$\begin{aligned}\tilde{A}_0 &= \frac{C-2T-3E}{3} + \frac{Y-2X}{3}e^{i\alpha},\\ \tilde{A}_2 &= \frac{C+T}{3} + \frac{X+Y}{3}e^{i\alpha},\end{aligned}$$

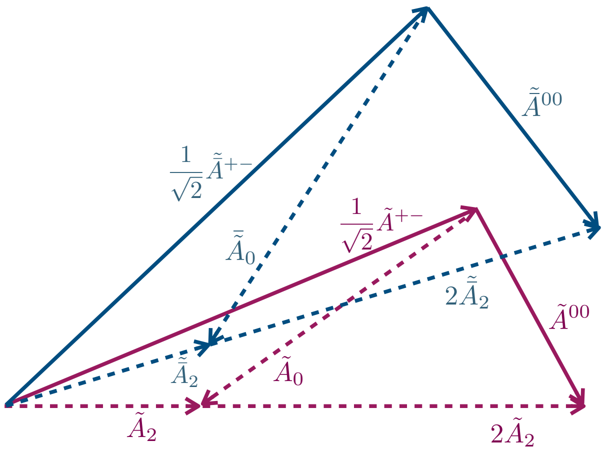

Figure 4.6: An illustration of the isospin triangles depicted in isospin space. the isospin amplitudes $\tilde{A}_0$, $\tilde{A}_2$, $\tilde{\bar{A}}_0$ and $\tilde{\bar{A}}_2$ defined in Eq. (4.35) are illustrated here.

$$
\begin{aligned}
\tilde{\bar{A}}_0 &= \frac{C-2T-3E}{3} + \frac{Y-2X}{3}e^{-i\alpha}, \\
\tilde{\bar{A}}_2 &= \frac{C+T}{3} + \frac{X+Y}{3}e^{-i\alpha}.
\end{aligned} \tag{4.39}
$$

Similar to our earlier approach, here we study the ratios of isospin amplitudes which are denoted by

$$\mathcal{R}_I = \{\tilde{A}_0/\tilde{A}_2, \tilde{\bar{A}}_0/\tilde{\bar{A}}_2, \tilde{A}_0/\tilde{\bar{A}}_0, \tilde{A}_2/\tilde{\bar{A}}_2\}$$

Notice that $\tilde{A}_0/\tilde{A}_2 = A_0/A_2$ and $\tilde{\bar{A}}_0/\tilde{\bar{A}}_2 = \bar{A}_0/\bar{A}_2$ which is evident from Eq. (4.37). The estimates of $\mathcal{R}_I$ for $B \to \pi\pi$ and $B \to \rho\rho$ are presented in Fig. 4.7 and Fig. 4.8, respectively. The light gray, light blue, light green and light orange contours correspond to 68.27% and 95.45% confidence levels of A_0/A_2, $\bar{A}_0/\bar{A}_2$, $A_0/\bar{A}_0$ and $A_2/\bar{A}_2$, respectively. The solutions presented in Fig. 4.7 and Fig. 4.8 correspond to the solutions in Fig. 4.4 and Fig. 4.5, respectively.

We find two sets of hierarchies among $\mathcal{R}_I$ from Fig. 4.7 and 4.8. For $B \to \pi\pi$ we find $|A_2| \approx |\bar{A}_2| \lesssim |A_0| < |\bar{A}_0|$ whereas for $B \to \rho\rho$ we find $|A_2| \approx |\bar{A}_2| < |A_0| \approx |\bar{A}_0|$. It is interesting to observe that in first and the last figure of Fig. 4.8 A_0/A_2 and $\bar{A}_0/\bar{A}_2$ are almost overlapping which leads to a relation among topological amplitudes. The isospin ratios can be written as

$$\frac{A_0}{A_2} = xe^{i\delta_x} + iye^{i\delta_y},$$

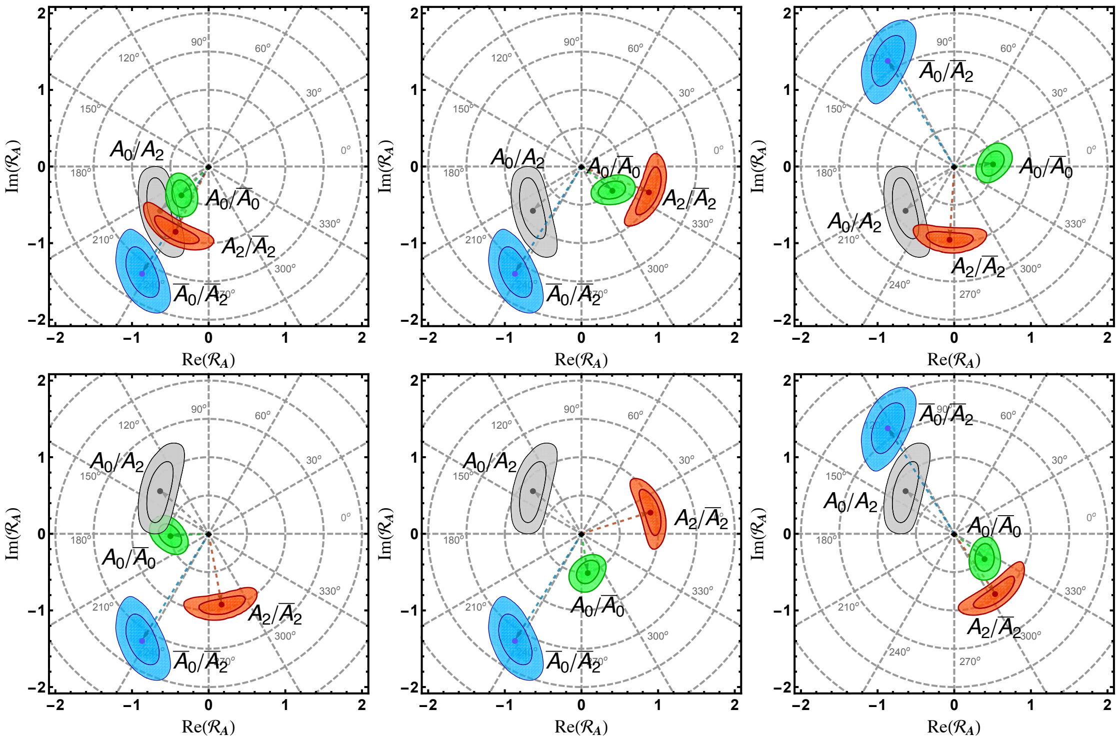

Figure 4.7: The estimated 68.27% and 95.45% confidence levels of $\mathcal{R}_I$ for $B \to \pi\pi$ modes are shown. The gray, blue, green and orange contours correspond to A_0/A_2, $\bar{A}_0/\bar{A}_2$, $A_0/\bar{A}_0$ and $A_2/\bar{A}_2$, respectively. The figures shown corresponds to the solutions presented in Fig. 4.3.

$$\frac{\bar{A}_0}{\bar{A}_2} = xe^{i\delta_x} - iye^{i\delta_y}, \tag{4.40}$$

where x, y, δ_x and δ_y are complicated function of topological amplitudes and α. Then the overlap of these two implies $y = 0$:

$$\frac{A_0}{A_2} \approx \frac{\bar{A}_0}{\bar{A}_2} \implies y = 0 \implies \frac{C-E}{T+E} \approx \frac{Y}{X}. \tag{4.41}$$

4.6 Summary:

In this chapter, we have shown that using seven experimental measurements available for $B \to \pi\pi$ or $B \to \rho\rho$ modes along with assuming the indirectly measured value of α, we can easily solve for seven hadronic parameters as well as all of the isospin amplitudes. The solutions have an eightfold ambiguity and measurement of the associated time-

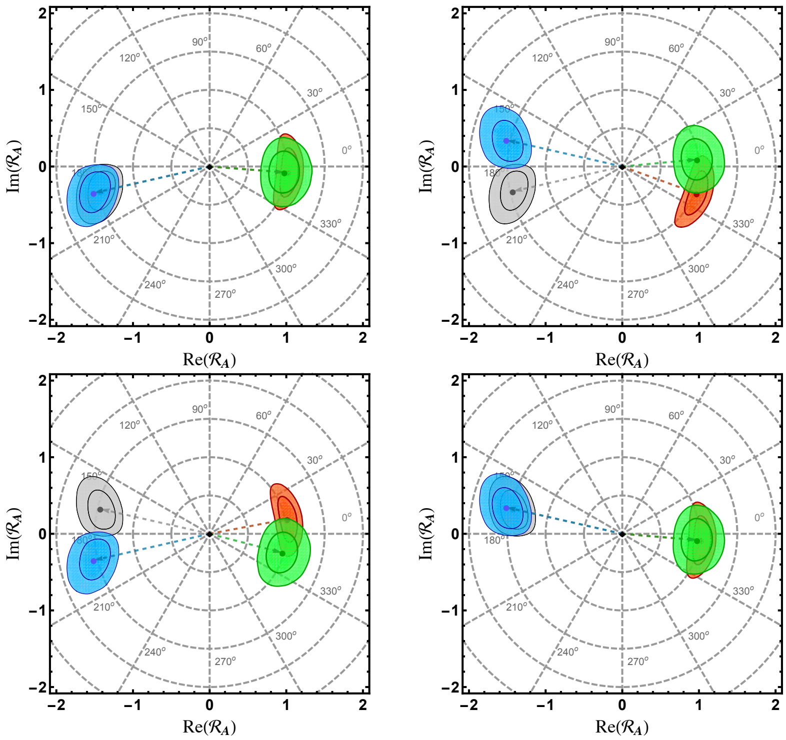

Figure 4.8: The estimated $\mathcal{R}_I$ for $B \to \rho\rho$ are depicted here. The color code and other details are same as of Fig. 4.7.

dependent CP asymmetry S_{00} can reduce or even eliminate this ambiguity. Given the current experimental accuracies, our estimates for the size of the electroweak penguin contributions are consistent with the SM. However, with improved accuracies in measuring the observables as well as the indirect measurements of α we can understand these contributions with improved certainty.

Chapter 5

Conclusion

The standard model of particle physics, though an impeccable theory, falls short of being the complete theory of fundamental interactions. However, the enormous success of SM at predicting numerous experimental observations, up to astronomical precision for some instances, can't be simply ignored. In view of these, a great amount of effort has been put in extending this highly successful yet incomplete theory to accommodate the phenomena left unexplained. With direct evidence for such beyond SM (BSM) scenarios still eluded at colliders, the indirect searches, sensitive to much higher scales than the reach of colliders, could be our gateway to BSM physics. With the advent of a high precision experimental era, this proposition may finally turn into reality. However, the advances in experimental measurements must also be complemented by theoretically clean measures to extract the new physics signals. In other words, we require formalisms that are less dependent on theoretical estimates of the hadronic parameters. In this thesis, we present two such formalisms: the first part is focused on extracting signals of RH currents in $B \to K^* \ell^+ \ell^-$, while the second part is focused on extracting the electroweak penguin contributions using experimental measurements in $B \to \pi\pi$ and $B \to \rho\rho$.

In chapter 3, we have presented a phenomenological approach to extract RH currents in $B \to K^* \ell^+ \ell^-$. We have relied on relations coming from heavy quark symmetries and kinetic constraints on the observables at q^2_{max}. This eliminates our dependence on hadronic estimates. A relation is obtained between form factor ratios R_λ which provides irrefutable evidence of RH currents. The R_λ is expressed completely in terms of the observables. The observables are Taylor expanded around $q^2_{\max}$ which are then fitted with the latest LHCb measurements. The results indicate a 5σ evidence for RH currents in $B \to K^*\ell^+\ell^-$. The significance of this signal can be reduced by introducing other kinds of feasible NP. Varying the lone theoretical input r/C_{10} results in a reduced 3σ evidence for RH currents. The impact of various non-perturbative and systematic contributions is also assessed. A detailed study of charm resonances in $B \to K^*\ell^+\ell^-$ indicates the absence of any significant contribution in data. We learn that if these contributions were somehow removed, the significance of RH currents would rise. We study the impact of variation in polynomial order, and the number of bins on the observable coefficients and chose the third-order polynomial fitted to 14-bin data as a benchmark. The sanctity of the choice has been justified through a fit to SM generated 14-bin dataset. We note that the inclusion of non-zero imaginary contributions and finite K^* width have an insignificant effect on our conclusions. In view of these, we conclude that with higher statistics and finer bins around $q^2_{\max}$, the presence of RH currents can be efficiently probed through this approach.

In chapter 4, we assess the effect of ignoring electroweak penguins on α measurements using $B \to \pi\pi$ and $B \to \rho\rho$ modes. The experimental measurements in these modes along with the indirectly measured value of α allow us to solve for seven hadronic parameters and all of the isospin amplitudes. The solution has an eightfold ambiguity which can be reduced or even eliminated by measuring the associated time-dependent CP asymmetry S_{00}. With current precision, our estimates for the size of the electroweak penguin contributions are consistent with the SM. This has particular relevance for $B \to \rho\rho$ as it indicates that the approximations made in isospin analysis for $B \to \rho\rho$ are reliable. The estimates for the isospin amplitudes are also obtained and a particular hierarchy among them is noted. Finally, we emphasize that with improved accuracy, effects such as the pollution in α measurement due to electroweak penguin contributions will become more and more relevant. This analysis provides a clear way to approach the problem of ignoring electroweak penguins. We note that precise measurements of CP asymmetries, some of which have not yet been measured, will be of great importance.

Chapter 5

Conclusion

The standard model of particle physics, though an impeccable theory, falls short of being the complete theory of fundamental interactions. However, the enormous success of SM at predicting numerous experimental observations, up to astronomical precision for some instances, can't be simply ignored. In view of these, a great amount of effort has been put in extending this highly successful yet incomplete theory to accommodate the phenomena left unexplained. With direct evidence for such beyond SM (BSM) scenarios still eluded at colliders, the indirect searches, sensitive to much higher scales than the reach of colliders, could be our gateway to BSM physics. With the advent of a high precision experimental era, this proposition may finally turn into reality. However, the advances in experimental measurements must also be complemented by theoretically clean measures to extract the new physics signals. In other words, we require formalisms that are less dependent on theoretical estimates of the hadronic parameters. In this thesis, we present two such formalisms: the first part is focused on extracting signals of RH currents in $B \to K^*\ell^+\ell^-$, while the second part is focused on extracting the electroweak penguin contributions using experimental measurements in $B \to \pi\pi$ and $B \to \rho\rho$.

In chapter 3, we have presented a phenomenological approach to extract RH currents in $B \to K^*\ell^+\ell^-$. We have relied on relations coming from heavy quark symmetries and kinetic constraints on the observables at $q^2_{\rm max}$. This eliminates our dependence on hadronic estimates. A relation is obtained between form factor ratios R_λ which provides irrefutable evidence of RH currents. The R_λ is expressed completely in terms of the observables. The observables are Taylor expanded around $q^2_{\rm max}$ which are then fitted with the latest LHCb measurements. The results indicate a 5σ evidence for RH currents in $B \to K^* \ell^+ \ell^-$. The significance of this signal can be reduced by introducing other kinds of feasible NP. Varying the lone theoretical input r/C_{10} results in a reduced 3σ evidence for RH currents. The impact of various non-perturbative and systematic contributions is also assessed. A detailed study of charm resonances in $B \to K^* \ell^+ \ell^-$ indicates the absence of any significant contribution in data. We learn that if these contributions were somehow removed, the significance of RH currents would rise. We study the impact of variation in polynomial order, and the number of bins on the observable coefficients and chose the third-order polynomial fitted to 14-bin data as a benchmark. The sanctity of the choice has been justified through a fit to SM generated 14-bin dataset. We note that the inclusion of non-zero imaginary contributions and finite K^* width have an insignificant effect on our conclusions. In view of these, we conclude that with higher statistics and finer bins around $q^2_{\rm max}$, the presence of RH currents can be efficiently probed through this approach.

In chapter 4, we assess the effect of ignoring electroweak penguins on α measurements using $B \to \pi\pi$ and $B \to \rho\rho$ modes. The experimental measurements in these modes along with the indirectly measured value of α allow us to solve for seven hadronic parameters and all of the isospin amplitudes. The solution has an eightfold ambiguity which can be reduced or even eliminated by measuring the associated time-dependent *CP* asymmetry S_{00}. With current precision, our estimates for the size of the electroweak penguin contributions are consistent with the SM. This has particular relevance for $B \to \rho\rho$ as it indicates that the approximations made in isospin analysis for $B \to \rho\rho$ are reliable. The estimates for the isospin amplitudes are also obtained and a particular hierarchy among them is noted. Finally, we emphasize that with improved accuracy, effects such as the pollution in α measurement due to electroweak penguin contributions will become more and more relevant. This analysis provides a clear way to approach the problem of ignoring electroweak penguins. We note that precise measurements of *CP* asymmetries, some of which have not yet been measured, will be of great importance.

SUMMARY

The thesis mostly focuses on three types of B decays. The rare decay $B \to K^* \ell^+ \ell^-$ has a rich angular distribution and is sensitive to physics beyond the standard model(SM). Our study is focused on the low-recoil limit, or the limit of soft K^* in B rest frame, or the limit of high q^2, where q^2 is the di-lepton invariant mass square. We have used kinematic constraints, and relations from heavy quark symmetries in this limit. Using a parametric fit of the observables to the LHCb data, we obtain clear evidence for right-handed(RH) currents. The impact of resonances and various systematic effects on our results are discussed in great detail. The other B decays considered in the thesis are $B \to \pi\pi$, and $B \to \rho\rho$. The unitarity angle α, from the *CKM* framework, is measured directly from these modes with the help of an isospin decomposition where electroweak penguin(EWP) contributions are ignored. However, EWPs are sensitive to new physics(NP). We present a clear way to approach the problem of ignoring them. We also observe that precise measurements of the *CP* asymmetries will be of great significance in dissolving the ambiguities.

Bibliography

[1] R. Mandal, R. Sinha and D. Das, "*Testing New Physics Effects in $B \to K^* \ell^+ \ell^-$*", *Phys. Rev.* **D 90** (2014) 9, 096006.

[2] R. Mandal and R. Sinha, "*Implications from $B \to K^* \ell^+ \ell^-$ observables using 3fb^{-1} of LHCb data*", *Phys. Rev.* **D 95** (2017) 1, 014026.

[3] A. Karan, R. Mandal, A. K. Nayak, R. Sinha and T. E. Browder, "*Signal of right-handed currents using $B \to K^* \ell^+ \ell^-$ observables at the kinematic endpoint*", *Phys. Rev.* **D 95** (2017) 11, 114006.

[4] The lepton mass corrections can easily be included as shown in Ref. [1]. However the corrections are negligible at large q^2.

[5] M. Beneke, T. Feldmann, D. Seidel, "*Systematic approach to exclusive $B \to V \ell^+ \ell^-$, $V\gamma$ decays*", *Nucl. Phys.* **B 612** (2001) 25-58.

[6] A. Khodjamirian, T. Mannel, A. A. Pivovarov and Y.-M. Wang, "*Charm-loop effect in $B \to K^{(*)} \ell^+ \ell^-$ and $B \to K^* \gamma$*", *JHEP* **09** (2010), 089.

[7] W. Altmannshofer, P. Ball, A. Bharucha, A. J. Buras, D. M. Straub and M. Wick, "*Symmetries and Asymmetries of $B \to K^* \mu^+ \mu^-$ Decays in the Standard Model and Beyond*", *JHEP* **01** (2009), 019.

[8] C. Bobeth, G. Hiller and D. van Dyk, "*The Benefits of $\bar{B} \to \bar{K}^* l^+ l^-$ Decays at Low Recoil*", *JHEP* **07** (2010), 098.

[9] D. Das and R. Sinha, "*New Physics Effects and Hadronic Form Factor Uncertainties in $B \to K^*\ell^+\ell^-$*", *Phys. Rev.* **D 86** (2012) 056006.

[10] G. Hiller, Roman Zwicky, "*(A)symmetries of weak decays at and near kinematic endpoint*", *JHEP* **03** (2014), 042.

[11] R. Aaij *et al.* [**LHCb** Collaboration], "*Angular analysis of the $B^0 \to K^{*0}\mu^+\mu^-$ decay using $3fb^{-1}$ of integrated luminosity*", *JHEP* **02** (2016), 104.

[12] R. Aaij *et al.* [**LHCb** Collaboration], "*Measurements of the S-wave fraction in $B^0 \to K^+\pi^-\mu^+\mu^-$ decays and the $B^0 \to K^*(892)^0\mu^+\mu^-$ differential branching fraction*", *JHEP* **11** (2016), 047, *JHEP* **04** (2017), 142 (erratum).

[13] W. Altmannshofer and D. M. Straub, "*New physics in $b \to s$ transitions after LHC run I*", *Eur. Phys. J.* **C 75** (2015) 8, 382; M. Ciuchini, M. Fedele, E. Franco, S. Mishima, A. Paul, L. Silvestrini and M. Valli, "*$B \to K^*\ell^+\ell^-$ decays at large recoil in the Standard Model: a theoretical reappraisal*", *JHEP* **06** (2016), 116; S. Jäger and J. Martin Camalich, "*Reassessing the discovery potential of the $B \to K^*\ell^+\ell^-$ decays in the large-recoil region: SM challenges and BSM opportunities*", *Phys. Rev.* **D 93** (2016) 1, 014028; S. Descotes-Genon, J. Matias and J. Virto, "*Understanding the $B \to K^*\mu^+\mu^-$ Anomaly*", *Phys. Rev.* **D 88** (2013) 074002; S. Descotes-Genon, L. Hofer, J. Matias and J. Virto, "*Global analysis of $b \to s\ell\ell$ anomalies*", *JHEP* **06** (2016), 092 and references therein.

[14] M. Gronau and D. London, "*Isospin analysis of CP asymmetries in B decays*", *Phys. Rev. Lett.* **65** (1990) 3381.

[15] M. Gronau, O. F. Hernandez, D. London and J. L. Rosner, "*Electroweak penguins and two-body B decays*", *Phys. Rev.* **D 52** (1995) 6374-6382.

[16] M. Gronau, D. London, N. Sinha and R. Sinha, "*Improving bounds on penguin pollution in $B \to \pi\pi$*", *Phys. Lett.* **B 514** (2001) 315-320.

[17] M. Gronau, D. Pirjol and T. M. Yan, "*Model-independent electroweak penguin amplitudes in B decays to two pseudoscalars*", *Phys. Rev.* **D 60** (1999) 034021; Erratum: *Phys. Rev.* **D 69** (2004) 119901.

[18] J. Charles *et al.* [**CKMfitter** Group], "*CP violation and the CKM matrix: Assessing the impact of the asymmetric B factories*", *Eur. Phys. J.* **C 41** (2005) 1, 1-131. http://ckmfitter.in2p3.fr

[19] Y. Amhis *et al.* [**HFLAV**], "*Averages of b-hadron, c-hadron, and τ-lepton properties as of summer 2016*", *Eur. Phys. J.* **C 77** (2017) 12, 895.

[20] J. Lees *et al.* [**BaBar** Collaboration], "*Measurement of an Excess of $\bar{B} \to D^{(*)}\tau^-\bar{\nu}_\tau$ Decays and Implications for Charged Higgs Bosons*", *Phys. Rev.* **D 88**, (2013) 7, 072012.

[21] M. Huschle *et al.* [**Belle** Collaboration], "*Measurement of the branching ratio of $\bar{B} \to D^{(*)}\tau^-\bar{\nu}_\tau$ relative to $\bar{B} \to D^{(*)}\ell^-\bar{\nu}_\ell$ decays with hadronic tagging at Belle*", *Phys. Rev.* **D 92**, (2015) 7, 072014.

[22] A. Abdesselam *et al.* [**Belle** Collaboration], "*Measurement of the branching ratio of $\bar{B}^0 \to D^{*+}\tau^-\bar{\nu}_\tau$ relative to $\bar{B}^0 \to D^{*+}\ell^-\bar{\nu}_\ell$ decays with a semileptonic tagging method* ", *arXiv*:1603.06711 [hep-ex].

[23] R. Aaij *et al.* [**LHCb** Collaboration], "*Measurement of the ratio of branching fractions $\mathcal{B}(\bar{B}^0 \to D^{*+}\tau^-\bar{\nu}_\tau)/\mathcal{B}(\bar{B}^0 \to D^{*+}\mu^-\bar{\nu}_\mu)$*", *Phys. Rev. Lett.* **115** (2015) 11, 111803.

[24] R. Aaij *et al.* [**LHCb** Collaboration], "*Test of lepton universality using $B^+ \to K^+\ell^+\ell^-$ decays*", *Phys. Rev. Lett.* **113** (2014), 151601.

[25] R. Aaij *et al.* [**LHCb** Collaboration], "*Test of lepton universality with $B^0 \to K^{*0}\ell^+\ell^-$ decays*", *JHEP* **08** (2017), 055.

[26] R. Aaij *et al.* [**LHCb**], "*Measurement of Form-Factor-Independent Observables in the Decay $B^0 \to K^{*0}\mu^+\mu^-$*", *Phys. Rev. Lett.* **111** (2013), 191801.

[27] **LHCb** Collaboration, "*Angular analysis of the $B^0 \to K^{*0}\mu^+\mu^-$ decay*", LHCb-CONF-2015-002.

[28] R. Aaij *et al.* [**LHCb** Collaboration], "*Differential branching fractions and isospin asymmetries of $B \to K^{(*)}\mu^+\mu^-$ decays*", *JHEP* **06** (2014), 133.

[29] R. Aaij *et al.* [**LHCb** Collaboration], "*Differential branching fraction and angular analysis of the decay $B_s^0 \to \phi\mu^+\mu^-$*", *JHEP* **07** (2013), 084.

[30] P. Ball and R. Zwicky, "*$B_{d,s} \to \rho, \omega, K^*, \phi$ decay form-factors from light-cone sum rules revisited*", *Phys. Rev.* **D 71** (2005), 014029.

[31] R. R. Horgan, Z. Liu, S. Meinel and M. Wingate, "*Lattice QCD calculation of form factors describing the rare decays $B \to K^*\ell^+\ell^-$ and $B_s \to \phi\ell^+\ell^-$*", *Phys. Rev.* **D 89** (2014) 9, 094501.

[32] A. Bharucha, D. M. Straub and R. Zwicky, "*$B \to V\ell^+\ell^-$ in the Standard Model from light-cone sum rules*", *JHEP* **08** (2016), 098.

[33] R. R. Horgan, Z. Liu, S. Meinel and M. Wingate, "*Calculation of $B^0 \to K^{*0}\mu^+\mu^-$ and $B_s^0 \to \phi\mu^+\mu^-$ observables using form factors from lattice QCD*", *Phys. Rev. Lett.* **112** (2014) 212003; R. R. Horgan, Z. Liu, S. Meinel and M. Wingate, "*Rare B decays using lattice QCD form factors*", *PoS* LATTICE2014 (2015) 372.

[34] S. Descotes-Genon, L. Hofer, J. Matias and J. Virto, "*On the impact of power corrections in the prediction of $B \to K^*\mu^+\mu^-$ observables*", *JHEP* **12** (2014), 125.

[35] S. Jäger and J. Martin Camalich, "*Reassessing the discovery potential of the $B \to K^*\ell^+\ell^-$ decays in the large-recoil region: SM challenges and BSM opportunities*", *Phys. Rev.* **D 93** (2016) 1, 014028.

[36] M. Beylich, G. Buchalla and T. Feldmann, "*Theory of $B \to K^{(*)}\ell^+\ell^-$ decays at high q^2: OPE and quark-hadron duality*", *Eur. Phys. J.* **C 71** (2011), 1635.

[37] A. Khodjamirian, T. Mannel and Y. M. Wang, "*$B \to K\ell^+\ell^-$ decay at large hadronic recoil*", *JHEP* **02** (2013), 010.

[38] S. Jäger and J. Martin Camalich, "*On $B \to V\ell\ell$ at small dilepton invariant mass, power corrections, and new physics*", *JHEP* **05** (2013), 043.

[39] C. Bobeth, G. Hiller and D. van Dyk, "*More Benefits of Semileptonic Rare B Decays at Low Recoil: CP Violation*", *JHEP* **07** (2011), 067.

[40] D. Becirevic and E. Schneider, "*On transverse asymmetries in $B \to K^*\ell^+\ell^-$*", *Nucl. Phys.* **B 854** (2012), 321-339.

[41] J. Matias, F. Mescia, M. Ramon and J. Virto, "*Complete Anatomy of $\bar{B}_d \to \bar{K}^{*0}(\to K\pi)\ell^+\ell^-$ and its angular distribution*", *JHEP* **04** (2012), 104.

[42] S. Descotes-Genon, J. Matias, M. Ramon and J. Virto, "*Implications from clean observables for the binned analysis of $B \to K^*\mu^+\mu^-$ at large recoil*", *JHEP* **01** (2013), 048.

[43] S. Descotes-Genon, T. Hurth, J. Matias and J. Virto, "*Optimizing the basis of $B \to K^*\ell\ell$ observables in the full kinematic range*", *JHEP* **05** (2013), 137.

[44] C. Bobeth, G. Hiller and D. van Dyk, "*General analysis of $\bar{B} \to \bar{K}^{(*)}\ell^+\ell^-$ decays at low recoil*", *Phys. Rev.* **D 87** (2013) 3, 034016.

[45] J. Lyon and R. Zwicky, "*Resonances gone topsy turvy - the charm of QCD or new physics in $b \to s\ell^+\ell^-$?*", *arXiv*:1406.0566 [hep-ph].

[46] W. Altmannshofer, P. Paradisi and D. M. Straub, "*Model-Independent Constraints on New Physics in $b \to s$ Transitions*", *JHEP* **04** (2012), 008.

[47] W. Altmannshofer and D. M. Straub, "*Cornering New Physics in $b \to s$ Transitions*", *JHEP* **08** (2012), 121.

[48] S. Descotes-Genon, J. Matias and J. Virto, "*Understanding the $B \to K^*\mu^+\mu^-$ Anomaly*", *Phys. Rev.* **D 88** (2013), 074002.

[49] F. Beaujean, C. Bobeth and D. van Dyk, "*Comprehensive Bayesian analysis of rare (semi)leptonic and radiative B decays*", *Eur. Phys. J.* **C 74** (2014), 2897, Erratum: *Eur. Phys. J.* **C 74** (2014), 3179.

[50] T. Hurth and F. Mahmoudi, "*On the LHCb anomaly in $B \to K^*\ell^+\ell^-$*", *JHEP* **04** (2014), 097.

[51] F. Kruger, L. M. Sehgal, N. Sinha, R. Sinha, "*Angular distribution and CP asymmetries in the decays anti-$B \to K^-\pi^+\ell^-\ell^+$ and anti-$B \to \pi^-\pi^+\ell^-\ell^+$*", *Phys. Rev.* **D 61**, 114028 (2000).

[52] B. Grinstein and D. Pirjol, "*Exclusive rare $B \to K^* \ell^+ \ell^-$ decays at low recoil: Controlling the long-distance effects*", *Phys. Rev.* **D 70** (2004), 114005.

[53] T. Hurth and M. Nakao, "*Radiative and Electroweak Penguin Decays of B Mesons*", *Ann. Rev. Nucl. Part. Sci.* **60** (2010), 645-677.

[54] A. J. Buras, "*Climbing NLO and NNLO Summits of Weak Decays*", *arXiv*:1102.5650 [hep-ph].

[55] B. Grinstein, M. J. Savage and M. B. Wise, "*$B \to X(s) e^+ e^-$ in the Six Quark Model*", *Nucl. Phys.* **B 319** (1989), 271-290.

[56] M. Beneke and T. Feldmann, "*Symmetry breaking corrections to heavy to light B meson form-factors at large recoil*", *Nucl. Phys.* **B 592** (2001), 3-34.

[57] F. Beaujean, M. Chrzäszcz, N. Serra and D. van Dyk, "*Extracting Angular Observables without a Likelihood and Applications to Rare Decays*", *Phys. Rev.* **D 91**, (2015) 11, 114012.

[58] F. Kruger and L. M. Sehgal, "*Lepton polarization in the decays $b \to X(s) \mu^+ \mu^-$ and $B \to X(s) \tau^+ \tau^-$*", *Phys. Lett.* **B 380** (1996) 199-204.

[59] K. A. Olive *et al.* [**P**article **D**ata **G**roup Collaboration], "*Review of Particle Physics*", *Chin. Phys.* **C 38** (2014) 090001.

[60] R. Aaij *et al.* [**LHCb** Collaboration], "*Measurement of the $B_s^0 \to J/\psi \bar{K}^{*0}$ branching fraction and angular amplitudes*", *Phys. Rev.* **D 86** (2012) 071102.

[61] K. Abe *et al.* [**Belle** Collaboration], "*Measurements of branching fractions and decay amplitudes in $B \to J/\psi K^*$ decays*", *Phys. Lett.* **B 538** (2002) 11-20.

[62] *http://www.imsc.res.in/~abinashkn/arXiv*.

[63] K. De Bruyn, R. Fleischer, R. Knegjens, P. Koppenburg, M. Merk, A. Pellegrino and N. Tuning, "*Probing New Physics via the $B_s^0 \to \mu^+ \mu^-$ Effective Lifetime*", *Phys. Rev. Lett.* **109** (2012) 041801.

[64] A. K. Nayak, R. Sinha, A. Karan and B. Grinstein, "*Constraining electroweak penguin graph contributions in measurements of the CKM phase alpha using* $B \to \pi\pi$ *and* $B \to \rho\rho$ *decays*", *Phys. Rev.* **D 101** (2020) 7, 073001.

[65] M. Tanabashi *et al.* [**P**article **D**ata **G**roup], "*Review of Particle Physics*", *Phys. Rev.* **D 98** (2018) 3, 030001.

[66] M. Tanabashi *et al.* [**P**article **D**ata **G**roup], "*Review of Particle Physics*", *"K^0_L meson" particle listing*.

[67] A. B. Carter and A. I. Sanda, "*CP Violation in Cascade Decays of B Mesons*", *Phys. Rev. Lett.* **45** (1980), 952.

[68] A. B. Carter and A. I. Sanda, "*CP Violation in B Meson Decays*", *Phys. Rev.* **D 23** (1981), 1567.

[69] B. Aubert *et al.* [**BaBar** Collaboration], "*Measurement of Time-Dependent CP Asymmetry in* $B^0 \to c\bar{c}K^{(*)0}$ *Decays*", *Phys. Rev.* **D 79** (2009), 072009.

[70] I. Adachi *et al.* [**Belle** Collaboration], "*Precise measurement of the CP violation parameter* $\sin 2\phi_1$ *in* $B^0 \to (c\bar{c})K^0$ *decays*", *Phys. Rev. Lett.* **108** (2012), 171802.

[71] R. Aaij *et al.* [**LHCb** Collaboration], "*Measurement of CP violation in* $B^0 \to J/\psi K^0_S$ *decays*", *Phys. Rev. Lett.* **115** (2015) 3, 031601.

[72] Y. S. Amhis *et al.* [**HFLAV** Collaboration], "*Averages of b-hadron, c-hadron, and* τ*-lepton properties as of 2018*", *arXiv*:1909.12524 [hep-ex].

[73] I. Adachi *et al.* [**BaBar, Belle**], "*First Evidence for* $\cos 2\beta > 0$ *and Resolution of the Cabibbo-Kobayashi-Maskawa Quark-Mixing Unitarity Triangle Ambiguity*", *Phys. Rev. Lett.* **121** (2018) 26, 261801.

[74] I. Adachi *et al.* [**BaBar, Belle**], "*Measurement of* $\cos 2\beta$ *in* $B^0 \to D^{(*)}h^0$ *with* $D \to K^0_S\pi^+\pi^-$ *decays by a combined time-dependent Dalitz plot analysis of BaBar and Belle data*", *Phys. Rev.* **D 98** (2018) 11, 112012.

[75] A. Abdesselam *et al.* [**BaBar, Belle**], "*First Observation of CP Violation in $\overline{B}^0 \to D^{(*)}_{\rm CP} h^0$ Decays by a Combined Time-Dependent Analysis of BABAR and Belle Data*", Phys. Rev. Lett. **115** (2015) 12, 121604.

[76] M. Gronau and D. London, "*How to determine all the angles of the unitarity triangle from $B^0_d \to DK_s$ and $B^0_s \to D\phi$*", Phys. Lett. **B 253** (1991), 483-488.

[77] M. Gronau and D. Wyler, "*On determining a weak phase from CP asymmetries in charged B decays*", Phys. Lett. **B 265** (1991), 172-176.

[78] D. Atwood, I. Dunietz and A. Soni, "*Enhanced CP violation with $B \to KD^0(\bar{D}^0)$ modes and extraction of the CKM angle γ*", Phys. Rev. Lett. **78** (1997), 3257-3260.

[79] D. Atwood, I. Dunietz and A. Soni, "*Improved methods for observing CP violation in $B^\pm \to KD$ and measuring the CKM phase γ*", Phys. Rev. **D 63** (2001), 036005.

[80] A. Poluektov *et al.* [**Belle** Collaboration], "*Measurement of ϕ_3 with Dalitz plot analysis of $B^\pm \to D^{(*)}K^\pm$ decay*", Phys. Rev. **D 70** (2004), 072003.

[81] A. Giri, Y. Grossman, A. Soffer and J. Zupan, "*Determining γ using $B^\pm \to DK^\pm$ with multibody D decays*", Phys. Rev. **D 68** (2003), 054018.

[82] G. P. Dubois-Felsmann, D. G. Hitlin, F. C. Porter and G. Eigen, "*Sensitivity of CKM fits to theoretical uncertainties and their representation*", *arXiv*:hep-ph/0308262 [hep-ph]; G. Eigen, G. Dubois-Felsmann, D. G. Hitlin and F. C. Porter, "*Global CKM Fits with the Scan Method*", Phys. Rev. **D 89** (2014) 3, 033004; S. Plaszczynski and M. H. Schune, "*Overall determination of the CKM matrix*", *PoS* **hf8** (1999), 019; D. Boutigny *et al.* (BaBar), in "*Workshop on Physics at Asymmetric B Factory (BaBar Collaboration Meeting) Pasadena, California, September 22-24, 1997*", *https://www-public.slac.stanford.edu/sciDoc/docMeta.aspx?slacPubNumber=SLAC-R-504*.

[83] M. Bona *et al.* [**UTfit** Collaboration], "*The Unitarity Triangle Fit in the Standard Model and Hadronic Parameters from Lattice QCD: A Reappraisal after the Measurements of Δm_s and $BR(B \to \tau\nu_\tau)$*", *JHEP* **10** (2006) 081. `http://utfit.org/UTfit/ResultsSummer2018SM`

[84] M. Gronau, O. F. Hernandez, D. London and J. L. Rosner, "*Decays of B mesons to two light pseudoscalars*", *Phys. Rev.* **D 50** (1994) 4529.

[85] D. London and R. D. Peccei, "*Penguin Effects in Hadronic B Asymmetries*", *Phys. Lett.* **B 223** (1989) 257-261.

[86] B. Grinstein, "*Critical Reanalysis of CP Asymmetries in B0 Decays to CP Eigenstates*", *Phys. Lett.* **B 229** (1989) 280-284.

[87] M. Gronau, "*CP Violation in Neutral B Decays to CP Eigenstates*", *Phys. Rev. Lett.* **63** (1989) 1451.

[88] M. K. Gaillard and B. W. Lee, "$\Delta I = 1/2$ *Rule for Nonleptonic Decays in Asymptotically Free Field Theories*", *Phys. Rev. Lett.* **33** (1974) 108.

[89] G. Altarelli and L. Maiani, "*Octet Enhancement of Nonleptonic Weak Interactions in Asymptotically Free Gauge Theories*", *Phys. Lett.* **B 52** (1974) 351-354.

[90] A. F. Falk, Z. Ligeti, Y. Nir and H. Quinn, "*Comment on extracting alpha from* $B \to \rho\rho$", *Phys. Rev.* **D 69** (2004) 011502.

[91] Y. Amhis *et al.* [**HFLAV** Collaboration], "*HFLAV input to the update of the European Strategy for Particle Physics*", *arXiv*:1812.07461 [hep-ex].

Thesis Highlights

Name of the Student: Abinash Kumar Nayak

Name of the CI/OCC: The Institute of Mathematical Sciences **Enrollment No.:** PHYS10201205009

Thesis Title: Right-Handed currents and Electroweak penguins in B decays

Discipline: Physical Sciences **Sub-Area of Discipline:** Particle Phenomenology

Date of viva voice: 19th Jan, 2021

Our universe is governed by four fundamental forces. The interactions of three of these forces(Strong, Weak, and Electromagnetic) can be explained through the standard model(SM) which has been the most successful theory in particle physics. However, the SM is incomplete. The first and obvious drawback is that It does not incorporate Gravity, the fourth fundamental force. Then, there are other observations such as the dark matter, the observed Baryon asymmetry, the neutrino oscillations, etc, which the SM fails to explain. Hence, we need better alternative theories(which are often called beyond SM(BSM) theories, or new physics(NP) theories) which can fill in the gaps left by SM. Such theories need to be established from an experimental viewpoint as well. There are two ways of going about this, direct and indirect. Where, direct experimental confirmation means that we genuinely produce new degrees of freedom corresponding to a theory that is not SM; we haven't had any luck with this so far. So, we turn to indirect signals of what lies beyond SM. However, in order to distinguish potential NP signals, we need very clean and precise SM estimates which are often a challenge.

Here, we are interested in weak decays of B mesons. The presence of a heavy spectator b-quark inside, gives us a much greater theoretical handle in studying its properties and decays. We are particularly interested in two types of quark transitions: $b \to s\, l^+ l^-$ and $b \to u\,\bar{u}\,d$. In the first type, we study the electroweak penguin dominated rare decay $B \to K^* l^+ l^-$. It possesses a very rich angular distribution which leads to a large number of observables. We propose a very unique and general framework to probe for the presence of right-handed(RH) currents in this mode. Our formalism does not rely on form factor estimates and draws inspiration from the heavy quark asymmetries and kinematic constraints at q^2_{max}, where q^2 is the di-lepton invariant mass squared. Using the LHCb measurements we obtain very clear evidence of RH currents in this mode. We study the impact of resonances and systematic effects on our results in great detail. We do not find any of them to be upsetting the significance of our claims. In the second type of quark transitions, we study the decays $B \to \pi\pi$, and $B \to \rho\rho$ in isospin space. These modes are used to measure the CKM angle α, which has great significance to SM. However, the isospin framework used in this process generally ignores the contributions from the Electroweak penguins(EWPs) which are sensitive to NP. We present a formalism where the EWPs can be estimated from experimental data. At the current experimental precision the EWPs are found to be consistent with the SM predictions. However, as measurements become more and more precise, effects such as pollution in α measurement due to non-zero EWPs will become more and more relevant. This analysis provides a clear way to approach the problem of ignoring EWPs.

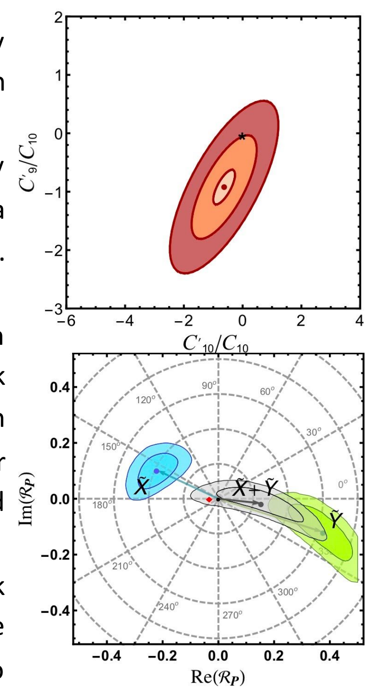

The top figure shows a clear evidence of RH currents. The bottom figure demonstrates a solution that is consistent with SM predictions.